Geochemical drivers of Mn removal in drinking water reservoirs under hypolimnetic oxygenation

Cissy Li Ming

Thesis submitted to the faculty of the Virginia Polytechnic Institute and State University
in partial fulfillment of the requirements for the degree of

Master of Science
In
Geosciences

Madeline E. Schreiber, Chair
Cayelan C. Carey
Benjamin C. Gill
Frederick M. Michel

May 9, 2023
Blacksburg, VA

Keywords: manganese, reservoir, pH, alkalinity, metals, Carvins Cove Reservoir, Falling Creek Reservoir, hypolimnetic oxygenation, autocatalysis

Geochemical drivers of Mn removal in drinking water reservoirs under hypolimnetic oxygenation

Cissy Li Ming

ABSTRACT

Manganese (Mn) is a drinking water contaminant associated with aesthetic and possible public health issues. Hypolimnetic oxygenation (HOx) systems are a novel treatment deployed in part to control Mn in lakes and reservoirs, introducing oxygen to the water column to promote oxidation and subsequent precipitation of redox-sensitive metals. Previous work in two southwestern Virginia drinking water reservoirs has documented differences in Mn removal by HOx systems. The different water chemistry of the reservoirs suggests the influence of geochemical drivers – notably pH and alkalinity – on Mn removal rates in lakes and reservoirs with HOx systems.

This study addressed the geochemical drivers of Mn removal, including pH, alkalinity and the presence of mineral particles. We conducted laboratory experiments and field monitoring at two drinking water reservoirs in southwestern Virginia – Falling Creek Reservoir (FCR) and Carvins Cove Reservoir (CCR). In laboratory experiments in pH and alkalinity-adjusted nanopure water solutions, we observed substantial Mn removal within 14 days only under high pH conditions (pH≥10). In experiments with high pH and moderate to high alkalinity (> 80 mg/L $CaCO_3$), near-total Mn removal occurred within 2 hours, at a rate of 0.25 mg/L^{-1} hr^{-1}. Mn removal occurred alongside precipitation of microscopic (<5 μm diameter) and macroscopic (>100 μm diameter) particles. Elemental analysis of particles with energy-dispersive X-ray spectroscopy (EDS) supports their identification as Mn(IV) oxides (MnOx), which suggests Mn

removal driven by oxidation. Elevated alkalinity in high pH solutions promotes Mn oxidation by maintaining high pH through buffering, which sustains conditions favorable for Mn oxidation. Our results also suggest sorption of Mn and mineral-catalyzed Mn oxidation by Mn oxides formed through oxidation by dissolved oxygen. In experiments using filtered and unfiltered water from the two reservoirs, we observed significant Mn removal in experiments with unfiltered water, suggesting that particles may remove Mn by catalyzing oxidation or nucleating Mn oxide precipitation. Mn removal occurred at 0.05 d^{-1} in unfiltered FCR water and 0.002 d^{-1} in unfiltered CCR water. We observed no Mn removal in filtered water from either reservoir. Scanning electron microscope (SEM) and EDS of visible particles from reservoir water experiments suggests that quartz and clay minerals present in the water column may nucleate or catalyze Mn oxide formation. Overall, this research shows that Mn removal under HOx operation is influenced by a variety of factors, including pH, alkalinity and suspended particles.

Geochemical drivers of Mn removal in drinking water reservoirs under hypolimnetic oxygenation

Cissy Li Ming

GENERAL AUDIENCE ABSTRACT

Elevated concentrations of manganese (Mn), a naturally occurring contaminant, can impair drinking water quality in several ways – by introducing poor taste and smell, staining pipes and appliances, and potentially harming the health of young children. Hypolimnetic oxygenation (HOx) is a novel water treatment method deployed in lakes and reservoirs to control water column contamination of metals and nutrients, including Mn. By pumping oxygen into lakes and reservoirs, HOx systems create conditions favorable for Mn removal from the water column. Previous work in two southwestern Virginia drinking water reservoirs documented differences between sites in how effectively HOx systems are able to remove Mn. These reservoirs have significant differences in their chemical profiles – most notably in pH and alkalinity, which suggests a role for background water chemistry in influencing removal rates in lakes and reservoirs with HOx systems.

We used laboratory experiments to simulate the effects of pH and alkalinity on Mn removal rates in oxygenated lakes and reservoirs. We observed substantial Mn removal within 14 days under high pH conditions (pH 10-11) and negligible removal in solutions at or under pH 8. In experiments with pH 10-11 and alkalinity over 80 mg/L, near-total Mn removal occurred within 24 hours. During the 24 hour removal window, we observed yellow-brown discoloration of our experimental solutions within 12 hours, followed by formation of loosely aggregated brown to black particles. Microscopy and

elemental analyses indicate that initial discoloration occurs due to formation of 1-2 μm wide manganese oxides with needle-like crystals. The visible aggregates are also manganese oxides. Based on mineral characterization and the time series of Mn removal observed in our experiments, we believe that initial formation of Mn oxides creates a positive feedback loop in solutions of pH 10-11 and alkalinity over 80 mg/L. Mn oxides promote further Mn oxide formation by facilitating conversion of Mn in solution into forms that easily settle from water. Observations of particulate formation and solution chemistry in filtered vs. filtered reservoir water from Falling Creek Reservoir and Carvins Cove Reservoir supports a pivotal role for particles in facilitating Mn removal. Our research addresses the impacts of water chemistry Mn removal in drinking water, and improves understanding of Mn cycling in natural freshwaters.

Acknowledgments

I want to extend my appreciation to everyone who contributed funding, labor, and resources to this study, in addition to those who provided support in less tangible ways.

Funding for this project was provided by the Virginia Tech Multicultural Academic Opportunities Program Graduate Fellowship, the Geological Society of America Graduate Research Grant Program, the Virginia Water Resources Research Center (VWRRC), the Roy J. Shlemon Scholarship from the Geological Society of America Environmental & Engineering Geology Division, the Virginia Tech Graduate and Professional Student Senate Graduate Research Development Program, the American Geosciences Institute Wallace Scholarship, NanoEarth at Virginia Tech, and the National Science Foundation (DEB-1753639, CNS-1737424, DBI-1933016).

Thank you to the Western Virginia Water Authority for allowing access to Falling Creek Reservoir and Carvins Cove Reservoir for sampling and monitoring. Jeff Parks performed ICP-MS analysis and Ethan Frederick performed ICP-AES analysis on reservoir and experimental samples. Kelly Peeler performed ion chromatography for reservoir samples. Lowell Moore assisted with EPMA analyses and SEM imaging, while Sheri Singerling operated the TEM on my behalf. The Virginia Tech Reservoir Group made invaluable contributions to fieldwork at the reservoirs and provided key feedback on my presentations, grant proposals and data. Undergraduate student Gavin Moore assisted with laboratory sampling and experimental setup for the 14-day experiments – thank you for your patience, hard work, willingness to learn and great attitude!

I owe my gratitude to my committee members – Dr. Cayelan Carey, Dr. Benjamin Gill and Dr. F. Marc Michel for lending a fresh set of eyes on my data and suggesting

new directions for my work. Thank you to Madeline Schreiber for chairing my committee, supporting me through every obstacle and dead end, and maintaining such relentless positivity when I felt discouraged or stressed. This thesis and research project would not have taken shape without your support and insights.

Thank you to my parents for supporting my decision to attend Virginia Tech, helping with living expenses, giving me a place to rest and recuperate on breaks, and taking me on Costco and Trader Joe's runs when I returned home. Last but not least, thank you to Brandon for being an amazing roommate and partner.

Table of Contents

Preface/Attribution

Authors:
Cissy L. Ming[1], Madeline E. Schreiber[1]
[1]Virginia Tech Department of Geosciences

- CLM and MES developed original project idea.
- CLM and MES planned batch experiments
- CLM conducted the batch experiments
- CLM wrote the thesis in consultation with MES.

1.0 Introduction

Elevated manganese (Mn) concentrations degrade surface and groundwater quality worldwide (Gantzer et al. 2009, Munger et al. 2016, World Health Organization 2021). At 0.05 mg/L, humans begin to experience poor taste from Mn in drinking water, though problems with discolored water and associated staining begin at concentrations as low as 0.02 mg/L (Tobiason et al. 2016, World Health Organization 2021). The U.S. Environmental Protection Agency (U.S. EPA) sets the secondary maximum contaminant level for Mn at 0.05 mg/L, a non-legally enforceable recommendation to water authorities meant to address aesthetic issues associated with elevated Mn concentrations (EPA 2021). Despite emerging public health research suggesting adverse health effects from Mn exposure, the U.S. EPA does not currently regulate Mn concentrations in drinking water for public health protection. However, in 2021, the World Health Organization (WHO) released a provisional health guideline of 0.08 mg/L for Mn in drinking water due to concerns about elevated mortality and childhood neurological deficits linked to Mn exposure during infancy (World Health Organization, 2021).

Mn is a common freshwater contaminant due to enrichment of Mn in sedimentary, igneous and metamorphic rocks of diverse geologic origin (De Vitre and Davison 1993). Mn can enter lakes and reservoirs through weathering of Mn-rich bedrock, flow of anoxic groundwater and leaching from low-oxygen soils (De Vitre and Davison 1993). Across the United States, median surface water Mn concentrations are 0.016 mg/L, with Mn detected at 97% of sites sampled by the United States Geological Survey (World Health Organization, 2021).

Oxidation and reduction reactions drive Mn cycling throughout the water column and between water and sediments in freshwater systems. Oxidation state dictates Mn solubility as is typical for transition metals. Three oxidation states of Mn – Mn(II), Mn(III) and Mn(IV) – are stable under conditions found in natural freshwaters (Davison 1993). Mn(II) is the soluble form of Mn, while Mn at higher oxidation states is insoluble. Although oxygen-rich waters favor the oxidation of Mn(II) to Mn(III) and Mn(IV), the slow rate of Mn oxidation in many freshwaters limits the amount of Mn removal that occurs in the water column on scales relevant to addressing contamination (Munger et al. 2016).

In temperate lakes and reservoirs, seasonal processes influence the oxidation-reduction reactions that release soluble Mn and remove it from the water column. During warm months, sunlight warms the top several meters of water while leaving deeper water cold. Non-uniform warming creates a density contrast between a warm surface layer – the epilimnion – and a cold, dense bottom layer – the hypolimnion (Wetzel 2001). The division of lakes and reservoirs into non-mixing layers with distinct properties is referred to as stratification. With the hypolimnion isolated from the atmosphere, microorganisms consume all oxygen in sediment porewater and the lower water column, occasionally depleting oxygen in the entire hypolimnion (Wetzel 2001).

Oxygen depletion in sediment pore waters of lakes and reservoirs creates conditions favorable for Mn reduction, resulting in upward diffusion and accumulation of soluble Mn in the hypolimnion (Krueger et al. 2020). In the absence of oxygen, solid oxidized forms of Mn (MnOx) become an energetically favored electron acceptor for bacterial respiration (Bryant et al. 2011, Davison 1993). Facultative anaerobic bacteria in

sediment reduce Mn(IV) to Mn(II), which then diffuses from sediments into the water column. Under conditions of seasonal stratification, Mn concentrations in the hypolimnion peak in summer and early fall (Schreiber et al. 2023).

As temperatures cool in fall, the decreasing density and temperature contrast between epilimnion and hypolimnion causes stratification to break down (Wetzel 2001). With the breakdown of stratification, known as fall turnover, the lake or reservoir mixes and oxygen returns to the entire water column. Once turnover restores dissolved oxygen (DO) to the water column, Mn oxidizes, forming Mn oxide minerals that settle to the sediments (Davison 1993).

The fluxes and macroscale processes behind Mn cycles at the lake and reservoir scale are generally well-understood (Chapnick et al. 1982, Davison 1993, Wetzel 2001). However, the impacts of reservoir geochemistry on mechanisms and rates of Mn removal require further examination. In the water columns of lakes and reservoirs, Mn removal occurs by abiotic oxidation, biotic oxidation, complexation, non-redox precipitation of Mn minerals, sorption and mineral-catalyzed oxidation. These chemical reactions are influenced by a complex interplay of biological and geochemical drivers (Davison 1993, Hsiung and Tisue 1994).

Oxidation is the primary process responsible for Mn(II) removal from the water column (Davison 1993, Equation 1). With each unit increase from pH 7, Mn(II) half life decreases by two orders of magnitude (Davison 1993). Because H+ forms as a product of Mn oxidation, basic pH (low H+) conditions drive the oxidation reaction forward (Equation 1, Tebo et al. 2004).

$$Mn^{+2}\,(aq) + 0.5\,O_2\,(aq) + H_2O\,(l) \leftrightarrow MnO_2\,(s) + 2H^+\,(aq) \qquad (1)$$

Bacterial oxidation of Mn has been documented as an integral component of the Mn cycle in lakes and reservoirs around the world. In the presence of Mn-oxidizing bacteria, Mn oxidation proceeds an order of a magnitude faster than under abiotic high pH conditions (Diem and Stumm 1984, Chapnick et al. 1982, Friedl et al. 1997, Table 8). Previous lake studies have observed slowing rates of Mn oxidation with extreme Mn concentrations, which would be expected for a biotically-driven reaction (Chapnick et al. 1982). Microbes may drive the initial formation of catalyzing Mn oxide or Mn oxy-hydroxide minerals, which then catalyze Mn oxidation (Hsiung and Tisue 1994, Learman et al. 2011). The amount of oxidizing activity by microbes may vary with light availability and other environmental factors. Godwin et al. (2020) only found significant Mn oxidation by microbes under light conditions, and calculated higher rates of mineral-catalyzed Mn oxidation in dark conditions.

Aqueous carbonate concentrations – which are closely linked to alkalinity of freshwaters – may influence Mn solubility through complexation reactions, precipitation of Mn carbonates and impacts on oxidation rate. Diem and Stumm (1984) reported Mn(II) oxidation half-lives of several years in solutions with high pH but low alkalinity, suggesting that alkalinity can control Mn removal and release rates in freshwater. High alkalinity may limit the release of Mn(II) from sediments by promoting sequestration of Mn as rhodochrosite ($MnCO_3$) in the upper centimeters of sediment (Davison 1993, Herndon et al. 2018). High alkalinity and high pH waters with abundant Mn, initial rhodochrosite precipitation may facilitate soluble Mn removal, as more rhodochrosite precipitates around the "seed" crystal (Herndon et al. 2018, Wittkop et al. 2020). Calcite crystals – also favored to form under high alkalinity and high pH conditions – may also

become sites for rhodochrosite precipitation (Herndon et al. 2018). In addition, high alkalinity can maintain high pH for prolonged periods, keeping water in conditions favorable to rapid oxidation (Hem 1963). However, high concentrations of carbonates may hinder Mn removal from water by decreasing abiotic Mn oxidation rates and complexing with Mn (Wetzel 2001).

Surfaces of particulate minerals suspended in the water column can accelerate Mn removal from water by catalyzing Mn oxidation and sorbing free Mn ions. Low-oxidation state transition metals – including Mn(II) – favorably sorb onto MnO2 particles and settle with the particles, a process that becomes more favorable at pH>7.5 (Tipping et al. 1984). Diem and Stumm (1984) proposed mineral catalysis of Mn(II) oxidation by rhodochrosite crystals, caused by the coordination arrangement of Mn in rhodochrosite. Ferrihydrite, magnetite and goethite – iron oxides and oxy(hydr)oxides abundant in soil and water – also catalyze Mn(II) oxidation (Lan et al. 2017). The size of mineral particles suspended in water impacts rates of mineral-catalyzed oxidation, with "dramatically" faster rates reported for hematite nanoparticles under 10 nm in size compared to larger particles (Madden and Hochella 2005). Mn oxide and hydroxide minerals formed by oxidation drive further Mn removal through mineral catalysis of oxidation. This reaction is theorized to occur in three steps: Mn oxidation by oxygen followed by precipitation of Mn oxide or hydroxide, adsorption of Mn(II) onto Mn oxide and oxidation of sorbed Mn(II) by the Mn oxide (Equation 2). The Mn oxide surface facilitates electron transfer to oxygen or Mn within the oxide (Hsiung and Tisue 1994).

$$\text{Step 1: } Mn^{+2}\,(s) + O_2\,(aq) \rightarrow MnO_2\,(s) \qquad (2)$$

$$\text{Step 2: } Mn^{+2}\,(aq) + MnO_2\,(s) \rightarrow Mn^{+2} \cdot MnO_2\,(s)$$

Step 3: $Mn^{+2} \cdot MnO_2$ (s) + O_2 (aq) → 2 MnO_2 (s)

These complex biogeochemical processes controlling Mn cycling in freshwaters present an ongoing challenge to water authorities interested in controlling Mn concentrations in drinking water supplies (Tobiason et al. 2016). Water treatment plants use expensive resins, chemical oxidizers, catalysts or biological treatments to remove Mn, which persists in soluble form across a broad range of chemical conditions (Kohl and Medlar 2006, Tobiason et al. 2016). In the past several decades, hypolimnetic oxygenation (HOx) has been deployed within drinking water reservoirs for water quality improvement, in part to remove Mn prior to the water treatment plant stage (Preece et al. 2019). This reduces the need for costly chemical agents later in the treatment process.

Since the 1990s, HOx has been deployed in over 30 lakes and reservoirs across the United States and Europe to improve fisheries, increase water clarity, and control metal and nutrient concentrations (reviewed by Preece et al. 2019). HOx systems introduce DO in the hypolimnion to restore oxygen concentrations to levels greater than 2 mg/L amid periods of seasonal anoxia. HOx aims to preserve stratification by circulating only the hypolimnion or infusing oxygen without circulating water, minimizing ecological disruption especially of valuable coldwater fish habitat (Moore et al. 2014). Infusing oxygen to the hypolimnion creates conditions favorable for the oxidation and subsequent removal of redox-sensitive metals like Mn (Preece et al. 2019). HOx systems also control the release of metals from sediments by promoting DO diffusion into sediment porewaters (Preece et al. 2019).

Short-term case studies of HOx systems in lakes and reservoirs across the United States and Europe have found mixed results on soluble Mn removal. Dent et al. (2014)

demonstrated substantial declines in soluble Mn concentration after eight hours of oxygenation in North Twin Lake in Washington. However, the observed decline of soluble Mn was offset by the re-mobilization of 94% of removed Mn within one week. At Lake Bard in California, Debroux et al. (2012) reported insignificant Mn removal over a two-week monitoring period following HOx system activation two months into stratification. However, Debroux et al. (2012) hypothesized that HOx in Lake Bard would decrease Mn concentrations on months-long timescales, based on results from laboratory experiments using sediment cores and water samples. In Lake Pleasant in Minnesota, the activation of a HOx system improved Mn removal outcomes relative to hypolimnetic aeration, a metals removal method that bubbles air into the water column (Austin et al. 2019). However, after HOx activation, Mn concentrations in the hypolimnion of Lake Pleasant had a median of 0.45 mg/L, which still exceeds the U.S. EPA secondary maximum contaminant level of 0.05 mg/L.

At two southwestern Virginia drinking water reservoirs, almost a decade of monitoring has found differing Mn removal outcomes from HOx (Gantzer et al. 2009, Munger et al. 2016). The Western Virginia Water Authority (WVWA) installed HOx systems at two reservoirs: Falling Creek Reservoir (FCR) in 2012 and Carvins Cove Reservoir (CCR) in 2005 (Gantzer et al. 2009, Gerling et al. 2014). With year-round operation, HOx has eliminated soluble Mn in the upper hypolimnion of CCR. As documented by Gantzer et al. (2009) and confirmed by monitoring in summer 2022, elevated Mn concentrations of up to 8 mg/L in CCR are limited to the bottom waters (below 17 m depth) (Schreiber et al. 2023, see Figures 15, 16). In FCR, HOx operation is limited to the stratified period – typically April-October. Throughout the hypolimnion of

FCR, Mn concentrations during intervals of HOx operation remain below 2 mg/L, but can reach 4 mg/L when the HOx is deactivated. Water quality monitoring has demonstrated differences in water chemistry between FCR and CCR, with possible implications for Mn cycling. Historical alkalinity data from the WVWA demonstrates lower alkalinity in FCR (median: 18 mg/L $CaCO_3$) compared to CCR (median: 62 mg/L $CaCO_3$) (Figure 17). During the stratified period, the median pH within the hypolimnion of CCR is ~7.5 and sediment porewater pH ranges from 8-9 (Bryant et al. 2011). In contrast, hypolimnetic pH in FCR ranges from 6.5-7.5, up to 1 unit lower than in CCR.

Our literature review yielded few studies addressing multiple Mn removal processes in drinking water reservoirs with different water chemistry. In this study, we conducted FCR and CCR field monitoring and laboratory experiments to examine geochemical drivers of Mn removal rates from lakes and reservoirs. Our laboratory experiments in both synthetic solutions and FCR and CCR water quantified Mn removal rates under controlled conditions. We used laboratory experiments to isolate the effects of individual drivers on Mn removal rate. Our field monitoring tracked water chemistry and ongoing Mn removal outcomes, to contextualize laboratory results. The central hypothesis of our study is that the combination of high pH and high alkalinity contributes to faster Mn removal. Based on previous studies, we propose the following potential mechanisms for faster Mn removal under high pH and high alkalinity: pH buffering, enhanced Mn carbonate precipitation, enhanced sorption of Mn onto Mn oxides, and mineral catalysis of Mn oxidation.

2.0 Methods

2.1 Site Description

2.1.1 Falling Creek Reservoir

Falling Creek Reservoir (FCR) in Vinton, VA, USA serves as a reserve water supply for Roanoke, VA. FCR is a eutrophic reservoir with a maximum depth of 9.3 m and surface area of 0.119 km^2. Land cover within the watershed of FCR is over 90% deciduous and mixed forest (Stroud Water Research Center 2017). FCR is located in the Blue Ridge Province of Virginia, with a watershed almost entirely underlain by varieties of granulite and granitic gneisses (Figure 1, Woodward 1932). Water inflows to FCR primarily through an inflow stream connected to nearby Beaverdam Reservoir (Gerling et al. 2016). A secondary inflow is located within a wooded wetland at the reservoir's northern shore (Carey et al. 2022). An outlet stream maintains stable water levels by draining excess inflow (Krueger et al. 2020). During stratification, the upper boundary of FCR's hypolimnion typically exhibits a median depth of 3.8 m (Krueger et al. 2020).

The WVWA installed a side stream super-saturation HOx system in fall 2012. Optimized for small, shallow lakes and reservoirs, the side stream super-saturation HOx system withdraws hypolimnetic water, supersaturates it with DO, then returns the supersaturated water to mix with the hypolimnion (Gerling et al. 2014) (Table 1). Since 2013, the HOx system in FCR has been periodically activated and deactivated for whole-reservoir ecological experiments (Carey et al. 2022). When we conducted our field monitoring during the summer 2022 stratified period, the HOx operated at reduced oxygenation capacity or was non-operational due to maintenance.

2.1.2 Carvins Cove Reservoir

Carvins Cove Reservoir (CCR) in Roanoke, VA, USA is a main water source for the city of Roanoke, VA. CCR is a eutrophic reservoir with five primary inflows: Sawmill Branch, Tinker Creek, Catawba Creek, Horsepen Branch and Carvin Creek (Gantzer et al. 2009, Roland 1970). The 2.5 km^2 reservoir has a maximum depth of 23 m (Gantzer et al. 2009b, Man et al. 2020). The watershed of CCR is 92% forested, but also includes less than 1% residential and agricultural land cover (Stroud Water Research Center 2017). The watersheds of three out of five major inflows to CCR are underlain by shale and sandstone, while Tinker Creek drains a watershed containing multiple carbonate formations (Roland 1970). Discharge from Tinker Creek raises water column alkalinity and pH within the hypolimnion, relative to FCR (Roland 1970). During stratification, the upper boundary of the hypolimnion typically falls at 5-6 meters depth (Gantzer et al. 2009).

The WVWA installed and activated a line diffuser HOx system in August 2005 (Table 1). Unlike in FCR, HOx operation typically continues year-round in CCR, though the volume of oxygen introduced by the system is decreased after turnover (Gantzer et al. 2009).

2.2 Water Column Sampling of FCR and CCR

At FCR, sampling of the reservoir water column occurred weekly from March to November 2022. For the remainder of the year, we sampled monthly. At the deepest point of FCR (site 50), samples for metals and anion analysis were collected at the surface (0.1 m), 1.6 m, 3.8 m, 5.0 m, 6.2 m, 8.0 m and 9.0 m using a 4 L Van Dorn sampler (Wildlife Supply Company; Yulee, FL) (see Table 2, Figure 3). The sampled depths correspond to outtake depths for reservoir water treatment. Metals samples were also collected close to the weir on FCR's intake (site 100) and at the wetland inflow (site 200) (see Table 2, Figure 3). At 0.1 m and 9.0 m at site 50, alkalinity samples were collected in duplicate by immersing a 250 mL Nalgene sample bottle

in reservoir water and capping the bottle while underwater, to minimize trapped atmospheric gasses. These samples were kept chilled until titration within 48 hours of collection. At each sampled depth, ~14 mL of unfiltered water was poured from the Van Dorn into a 15 mL centrifuge tube for total metals analysis. For soluble metals, ~14 mL of water was syringe filtered (0.45 μm nylon filter) into a 15 mL centrifuge tube. For anion analysis, ~50 mL of water was syringe filtered (0.45 μm nylon filter) into a triple-rinsed Nalgene sample bottle.

At CCR, sampling occurred fortnightly from June to mid-August 2022. From August to November 2022, sampling frequency declined to monthly. At the deepest point of CCR (site 50), metals and ion samples were collected at the surface (0.1 m), 1.5 m, 6.0 m, 9.0 m, 15.0 m and 20.0 m. Alkalinity samples were collected at 0.1 m and 20.0 m. Sample collection procedures were identical to FCR procedures. On dates when flow was observed in CCR's tributaries, anion and metal samples were also collected at Sawmill Branch (site 301), Catawba Creek Tunnel (site 501), Tinker Creek Tunnel (site 400) and Carvins Creek Stream (site 201) (see Table 2, Figure 2). Discharge data were collected at each inflow using a FlowMate hand-held flow meter to measure velocity and a meterstick to measure water depth across a representative transect.

In July 2022, surface sediments were collected from CCR site 50 using an Ekman bottom grab sampler. Powder X-ray diffraction (XRD) was conducted on the dried sediments in the Virginia Tech Department of Geosciences using a Rigaku Miniflex II with a copper X-ray tube (Rigaku Corporation, Tokyo, Japan). The XRD spectrum was analyzed for mineral content using Match! Software, which matched peaks detected in the sediment sample to peaks found in reference minerals (Putz and Brandenburg, n.d.).

At site 50 of both reservoirs, we measured temperature, DO, turbidity and pH profiles at 0.1 m increments using a Seabird Electronics SBE 19plus high-resolution conductivity,

temperature and depth meter (CTD). The CTD continuously recorded these parameters from the water surface to the base of the water column. In 2022, CTD profiles were collected at every FCR sampling day and on 2/28, 7/7, 7/14 and 8/19 in CCR.

2.3 Water Quality Analysis Methods

2.3.1 Metals analysis

Within 12 hours of collection, both filtered and unfiltered metals samples were acidified with 10 drops of 1:1 trace metals-grade nitric acid (HNO_3) delivered by transfer pipette. Samples were analyzed for metals by Inductively Coupled Plasma-Mass Spectrometry (ICP-MS; Thermo Electron iCAP RQ) in the Virginia Tech Department of Civil and Environmental Engineering. The method's detection limit for Mn is 0.001 mg/L. The instrument has a relative standard deviation under 2% for measuring the concentrations of most elements.

2.3.2 Anion analysis

Anion samples were kept chilled for transport to the lab, then frozen until analysis by anion chromatography (Metrohm 930 Compact IC Flex) in the Virginia Tech Department of Biological Systems Engineering Water Quality Lab. Analysis was conducted for NO_3^-, Cl^- and SO_4^{-2}. The ion analysis method's lower detection limit is 0.1 mg/L for all anions of interest. The instrument's accuracy and precision is 0.1% (Adamo, 2020).

2.3.3 Alkalinity titrations

We adapted our alkalinity titration method from the Massachusetts Water Watch Partnership Standard Operating Procedure for pH and alkalinity of low to medium alkalinity lakes (UMass Amherst 2016). After alkalinity samples warmed to room temperature, 100 mL of sample was transferred to a 150 mL Erlenmeyer flask. The sample was continually mixed at slow speed with a magnetic stir bar while drops of H_2SO_4 were added from a Hach digital titrator. We

used 0.16 N cartridges for natural waters and experimental solutions without alkalinity adjustment, and 1.6 N cartridges for experimental solutions with alkalinity adjustment. We monitored pH changes throughout titration with an OHaus benchtop pH meter. Alkalinity in mg/L $CaCO_3$ was calculated according to Equation 3. These endpoints represent the depletion of CO_3^{-2} and HCO_3^-, respectively.

$$\text{Alkalinity} = (2A-B)*0.1$$

$$\text{Where A=total number of } H_2SO_4 \text{ drops added to reach pH 4.5,} \quad (3)$$

$$\text{B=total number of } H_2SO_4 \text{ drops added to reach pH 4.2.}$$

2.4 Laboratory pH and Alkalinity Experiments

We conducted two sets of laboratory experiments in synthetic solutions to measure the effects of pH and alkalinity on Mn removal rate. The first experiment tested Mn removal under eight conditions of varying pH and alkalinity over a 14-day period (see Table 3 for full description). Samples were collected at 0, 1, 4, 7, 10 and 14 days. The second experiment included select conditions from the 14-day experiment, run over 24 hours (see Table 4 for full description). During the experiment, we collected samples at 0, 1, 2, 6, 12 and 24 hours (Ming and Schreiber 2023, EDI data product).

The experiments were conducted in 500 mL acid-washed Erlenmeyer flasks containing 250 mL of 1 mg/L $MnCl_2$ solution adjusted to varying alkalinity and pH (see Tables 3 and 4). We adjusted alkalinity of 1 mg/L $MnCl_2$ solutions by adding $NaHCO_3$ crystalline solid and raised pH by iteratively adding 0.1 N NaOH (Ming and Schreiber 2023, EDI data product). Alkalinity and pH were measured in initial solutions for each condition. Aluminum foil-covered flasks were incubated at room temperature on orbital shakers (150 rotations per minute, rpm).

At each sampling interval, ~1.5 mL of solution was withdrawn from each flask for pH measurement using an OHaus benchtop pH meter. We collected and syringe 10 mL of solution from each flask (0.22 μm nylon syringe filter) for analysis of Mn (Ming and Schreiber 2023, EDI data product). Samples collected for Mn analyses were acidified with ~0.5 mL of 1:1 trace metals-grade HNO_3. Analyses were conducted by ICP-AES in the Soils Testing Laboratory at Virginia Tech using APHA Standard Method 3125-B for the 14-day experiments (American Public Health Association et al., 1998). Mn analyses for the 24-hour experiments were conducted by ICP-MS in the Virginia Tech Department of Civil and Environmental Engineering. At the end of both experiments, 100 mL of solution from each pH and alkalinity condition described in Table 3 and 4 was titrated for alkalinity (Ming and Schreiber 2023, EDI data product).

2.5 Reservoir Water Laboratory Experiments

We conducted an experiment using hypolimnetic water from FCR and CCR to compare Mn removal rates between reservoirs. Our 10-day experiment tested Mn removal rates in unfiltered and filtered water (0.45 μm) from both reservoirs (Ming and Schreiber 2023, EDI data product). In mid-March 2023 (prior to stratification), water for experiments was collected at 9 m in FCR and 18 m in CCR using a 4 L Van Dorn sampler (Wildlife Supply Company; Yulee, FL). We immediately transferred water from the Van Dorn into opaque brown plastic Nalgene bottles then stored under chilled conditions (1-3 °C) until experimental setup ~36 hours later. We spiked all reservoir water experiments with 100 mg/L $MnCl_2$ solution to achieve a Mn concentration of 1 mg/L and included a control with unaltered 1 mg/L $MnCl_2$ in DI water (see Tipping et al. 1984, Godwin et al. 2020) (Ming and Schreiber 2023, EDI data product).

Experiments of 250 mL each were conducted in triplicate, in acid-washed 500 mL Erlenmeyer flasks. Flasks covered in aluminum foil were incubated at room temperature on

orbital shakers (150 rpm). Sampling occurred at 0, 1, 4, 7 and 10 days. The procedure for sampling, sample preservation and collecting pH measurements remained consistent from the methods described for 14-day and 24-hour experiments (Ming and Schreiber 2023, EDI data product).

2.6 Particle Analysis

2.6.1 Electron Probe Micro-Analyzer (EPMA)

We analyzed selected particles from 24-hour laboratory experiments and reservoir water experiments using the JEOL JXA-iHP200F Field Emission EPMA (JEOL, Ltd., Tokyo, Japan) housed at the Virginia Tech Nanoscale Characterization and Fabrication Laboratory (NCFL). Identifying and determining the relative abundances of elements on the particle surface allowed us to identify the class of mineral formed, which informed our interpretation on the mechanisms of Mn removal in high pH and moderate to high alkalinity solutions. At the conclusion of the 24-hour experiment and the reservoir water experiments, visible particles were collected from experimental solutions and rinsed in nanopure (18.1 mΩ) water to remove salts. Particles were mounted on copper tape electrical tape by pipetting 10 µL of solution onto the tape, then allowing water to evaporate. Once desiccated, mounted samples were evaporation-coated with carbon (Heu et al. 2019). We collected quantitative data on the EPMA for the elemental compositions of each analyzed particle and element maps showing the relative abundances of elements on the particle surface. We also collected high-magnification scanning electron microscope (SEM) images of the particles' morphology and texture as done by Adams et al. (2009) and Sánchez-España and Yusta (2019).

2.6.2 Transmission Electron Microscopy (TEM)

We used the JEOL JEM 2100 TEM (JEOL, Ltd., Tokyo, Japan) housed at the Virginia Tech NCFL to characterize microscopic (<5 μm diameter) particles in discolored 24-hour experiment solutions and FCR unfiltered reservoir water. The combination of imaging, energy-dispersive X-ray spectroscopy (EDS) and selected area electron diffraction (SAED) shed light on the specific mineral phases present in discolored solutions. We collected 2 mL aliquots from the high pH and moderate or high alkalinity experiments at 12 hours, and preserved them at -18 °C before ultracentrifugation at 109000 RCF for 1 hour to concentrate particles (Learman et al. 2011). Prior to drop casting on a 300 mesh lacey carbon TEM grid, particles were resuspended in deionized water by sonication (Williams and Carter 1996). For each pH and alkalinity condition, 2-3 grids were prepared with 10-20 μL of suspension transferred onto each grid by micropipette. SAED was used to identify the crystalline structure. We applied EDS to determine the elemental composition of particles.

Diffraction patterns obtained from SAED were analyzed for d-spacing using the Gatan Digital Micrograph software package (Gatan Digital Micrograph, v. 3.5). Rings were manually identified and annotated on diffraction patterns. Based on d-spacings with a +/- 0.05 Å tolerance, diffraction pattern matches were identified in the American Mineralogist Crystal Structure Database among Mn oxide and hydroxide phases (Downs and Wallace, 2003).

2.7 Geochemical Modeling in Geochemist's Workbench (GWB)

Using the Sp8 module of GWB, we ran simulations of speciation and mineral precipitation within pH and alkalinity experimental solutions to support our identification of minerals formed in solution (Bethke 2007). We based our models on compositions of our experimental solutions obtained by ICP-MS. We additionally used metals and anion

concentrations obtained from the summer 2022 field campaign at FCR and CCR to model speciation and mineral precipitation in the reservoir water column.

2.8 Calculation of Mn Removal Rate

For the 24-hour high pH and moderate alkalinity solution, we calculated the second-order Mn(II) removal rate (K, $mg/L^{-1}\ hr^{-1}$) by fitting a linear equation to the inverse of Mn concentration data averaged across triplicates from our experiments (Rimstidt, 2013). We also attempted to fit a linear equation to a first- and zero-order transformation of the concentration data, and found the greatest fit with a second-order transformation. For the FCR and CCR unfiltered experiments, we calculated the first-order Mn(II) removal rate (K, d^{-1}) by fitting a linear equation to the natural log of Mn concentration data averaged across triplicates (Rimstidt, 2013).

3.0 Results

3.1 Solution Chemistry of Laboratory Experiments

3.1.1 14-day pH and alkalinity laboratory experiments

Over the 14-day experiment, we only observed decreases in soluble Mn concentration within solutions of high pH (pH≥10) (Figure 4). In high pH experiments with moderate (≥80 mg/L $CaCO_3$) or high (≥200 mg/L $CaCO_3$) alkalinity, the soluble Mn concentration declined to less than 20% of initial values within 24 hours. Slower declines of soluble Mn concentration were observed in high pH solutions with no alkalinity adjustment (Figure 4).

During the experiment, we observed solution color changes and particle formation in experiments of high pH and moderate or high alkalinity. We observed a yellowish-brown color at the 24-hour sampling in experiments of high pH/moderate alkalinity, which persisted throughout. In the high pH/high alkalinity experiments, rusty brown to black aggregates formed within 24 hours (Figure 7, Table 5). In experiments of pH≤8, we observed no solution color changes or particle formation over the 14 days.

Alkalinity adjustment helped maintain consistent pH within high pH and moderate or high alkalinity solutions (Figure 4). Between 1-4 days, the pH in high pH solutions without alkalinity adjustment began to decline relative to pH of high pH and moderate or high alkalinity solutions. By day 14, pH within the non-buffered high pH solution had dropped over one unit from the pH recorded at the experiment's onset.

3.1.2 24-hour pH and alkalinity laboratory experiments

We observed significant decreases in soluble Mn concentrations within one hour in high pH solutions with moderate or high alkalinity (see Figure 5). In contrast, we observed negligible changes in soluble Mn concentration in control solutions. In high pH/moderate alkalinity

solutions, the vast majority of Mn removal occurred between 0-2 hours, with a minor drop in soluble Mn concentration at hour 6 (Figure 5).

With sampling every few hours, we observed discoloration and particle formation in high pH and moderate or high alkalinity solutions within 12 hours. Upon initial experimental setup, the high pH/high alkalinity and high pH/moderate alkalinity solutions displayed translucent yellow-brown discoloration, which remained consistent in high pH/moderate alkalinity solutions (Table 6). Rusty-brown particles formed in high pH/high alkalinity and high pH/moderate alkalinity solutions between 6-12 hours. Between 6-12 hours, the high pH/high alkalinity solution became more opaque and a darker shade of brown (Table 6). Between 12-24 hours, the high pH/high alkalinity solution became clear, similar to visual observations at 1 day in the 14-day experiments.

3.1.3 Reservoir water laboratory experiments

We only observed significant Mn removal over 10 days in unfiltered reservoir water experiments (Figure 6). Significant Mn removal began between day 0 and day 1 in unfiltered FCR reservoir water, with near total Mn removal between 1-4 days (Figure 6). Decline of soluble Mn concentration continued into day 7, but Mn concentrations increased to approximately 50% of initial concentrations in solution between days 7-10 (Figure 6). In unfiltered CCR reservoir water experiments, significant Mn removal began between day 4-7, then Mn concentrations declined at a linear rate until day 10 (Figure 6).

Initial visual observations of reservoir water from FCR and CCR were similar. Water collected from the lower water column of both reservoirs was clear with tan and black silt- to fine sand-sized particles observed at the bottom of the flask (see Table 7). In unfiltered FCR reservoir water, translucent orange-pink discoloration and formation of rusty brown to black

aggregates occurred between day 1-4 (Figure 11, Table 7). In unfiltered CCR reservoir water, both yellow-brown solution discoloration and particle formation occurred between day 4-7 (Figure 12, Table 7).

The filtered reservoir water and control solutions remained clear for the entire experiment. However, we observed black silt-sized particles in FCR filtered experiments at 10 days, but they were present in lower abundance than those observed in unfiltered experiments (Figure 13). No visible particles formed in the CCR filtered experiments.

3.1.4 Calculation of Mn removal rates in experiments

In the high pH/moderate alkalinity 24-hour experiments, the second-order Mn removal rate constant was 0.25 $mg/L^{-1}\ hr^{-1}$ (sd: 0.1 $mg/L^{-1}\ hr^{-1}$) as calculated from averaged concentration time series data. The first-order Mn removal rate constant for CCR unfiltered water from day 0-10 was 0.002 d^{-1} and the corresponding rate constant was 0.050 d^{-1} for FCR unfiltered water from day 0-7 (Table 8).

3.2 Particle analysis

3.2.1 24-hour pH and alkalinity laboratory experiment

All macroscopic (>100 μm diameter) particles sampled from experiments at 24 hours contained abundant Mn and oxygen on their surfaces, as indicated by EDS element maps and quantitative analyses (Figure 7). We observed trace amounts of carbon on the particles likely introduced by carbon coating (Figure 7). Across the particles collected and analyzed, size and morphology did not differ substantially between particles from high pH/high alkalinity and high pH/moderate alkalinity experiments. When imaged by SEM at 200x magnification, representative particles had pitted surface textures (Figure 7). Diameters of imaged particles ranged from 100-500 μm.

TEM-imaged microscopic particles from high pH and moderate or high alkalinity solutions had similar morphologies, elemental compositions and crystal properties. For both high pH/moderate alkalinity and high pH/high alkalinity solutions, particles were interlocking needle-like crystals aggregated in a dense mass (Figure 8, S6, S7). The aggregate particles were ~2 μm in diameter, and individual needles were ~10-20 nm in diameter. In the particle collected from the high pH/high alkalinity solution, we observed thin sheets on the particle's periphery alongside the needles. EDS element maps indicate they are composed of oxygen and manganese (Figure 8).

We used d-spacings of the two particles from SAED analysis and modeling results from GWB to identify Mn minerals forming in experiments (Figure 9, 10). For the particle analyzed from the high pH/moderate alkalinity solution, d-spacings of the two major ring patterns ranged from 2.24-2.49 Å and 1.51-1.52 Å (Figure 9). For the particle analyzed from the high pH/high alkalinity solution, d-spacings of the two major ring patterns ranged from 2.28-2.46 Å and 1.39-1.44 Å (Figure 9). The combination of measured d-spacings and GWB calculations suggest birnessite and pyrolusite – both Mn(IV) minerals – as probable candidates for particles precipitated in the high pH/moderate alkalinity and high pH/high alkalinity solutions.

3.2.2 Reservoir water laboratory experiment

Morphologies and elemental compositions of visible particles collected from both FCR and CCR unfiltered water experiments were similar. In both unfiltered experiments, we observed platy and blocky particles aggregated with globular textures (Figure 11, 12). The aggregates were ~100 μm in diameter; platy and blocky particles within the aggregates were less than 10 μm in diameter. Element mapping with EPMA indicates that blocky and platy particles contain abundant SiO_2 (Figure 11). The globular textured material was abundant in Mn and oxygen, with

concentrated areas of Fe and oxygen (Figure 11). The aggregation of varying compositions and textures in particles from unfiltered experiments contrasted with the composition and texture of particles from filtered FCR reservoir water, which were uniformly globular and composed of Fe oxides and Mn oxides (Figure 13). We observed concretion-like spheres composed of Mn and oxygen within samples collected from filtered FCR reservoir water (Figure 13).

The TEM-imaged microscopic particles from FCR unfiltered water were similar to one another in morphology, elemental composition and crystal properties. All imaged particles had crumpled sheet-like morphologies, with individual particles ~3-5 μm in diameter. EDS element maps indicate they are composed of oxygen and manganese (Figure 14). Across the analyzed particles, d-spacings of the two major ring patterns ranged from 2.21-2.58 Å and 1.38-1.53 Å (Table S9). Based on the elemental composition, d-spacings and crumpled sheet morphology of particles, we identified the particles as likely consisting of aggregated birnessite.

3.2.3 Geochemist's Workbench solid phase calculations for pH and alkalinity experiments

According to solubility calculations using the Spec8 module, Mn oxide precipitation was favored to occur over rhodochrosite precipitation in all high pH and pH 8 experiments. Based on saturation index, a measure of a mineral's probability of precipitating, birnessite (δ-MnO_2) was most favored to precipitate by several orders of magnitude, with hausmannite also favored to precipitate. Rhodochrosite was predicted to be undersaturated in high pH experiments, but was at or slightly over saturation in pH 8/high alkalinity experiments. At the same pH conditions, the calculated solubility of Mn minerals did not vary substantially with alkalinity (see Appendix I).

3.3 Reservoir Monitoring

3.3.1 pH, alkalinity, turbidity and Mn concentrations in FCR and CCR

Our 2022 observations of total and soluble Mn concentration in FCR and CCR were consistent with historical data from both reservoirs (Figure 15, 16). In CCR, high Mn concentrations were restricted to the bottom meters of the water column, as reported by Gantzer et al. (2009) (Figure 15). In the 2022 stratified period, accumulation of Mn in the hypolimnion of FCR continued during periods of HOx operation and deactivation (Figure 16).

In both FCR and CCR, the alkalinity of the lower hypolimnion remained consistently higher than the alkalinity of surface water (Figure 17, 18). The range of alkalinities observed in CCR from June-October 2022 (25-45 mg/L $CaCO_3$) was higher than the typical range observed in FCR over the same interval (12-26 mg/L $CaCO_3$) (Figure 17, 18). An outlier alkalinity of over 50 mg/L $CaCO_3$ was recorded in the hypolimnion of FCR for 8/29/2022 (Figure 17).

From May 1 to November 1, 2022, the median pH in the hypolimnion of FCR was significantly lower than the median pH in the hypolimnion of CCR. The median hypolimnetic pH in FCR was 6.85 compared to 7.37 in CCR (Figure 18).

At depths sampled for reservoir water experiments, we compared 2013-2022 turbidity data collected at site 50 in FCR (9-10 m) and CCR (18-19 m). For every year with data for both reservoirs, median turbidity for FCR (9-10 m) and CCR (18-19 m) falls below 20 NTUs. However, the spread of turbidity in FCR is larger than the CCR spread, with annual peak turbidity in FCR sometimes exceeding 60 NTUs during intervals of phytoplankton blooms or high iron oxidation rates (Wetzel 2001). When aggregated by years, the turbidity medians in FCR are higher than medians in CCR across every year of monitoring with data available from both reservoirs, except 2013. When aggregated by months from May-October, the median turbidity in FCR is higher than in CCR across every month except September and June. The

difference between median FCR and CCR turbidity in corresponding years or months ranged from less than 1 NTUs to 8 NTUs.

3.3.2 XRD of CCR sediments

XRD analyses of sediments collected from the sediment-water interface at CCR site 50 indicates presence of quartz and montmorillonite, a clay mineral. The XRD analyses did not detect Fe or Mn phases in the sediment (see Appendix A).

3.3.3 Geochemist's Workbench solid phase calculations from field data

According to solubility calculations using the Spec8 module, Mn oxide precipitation is favored at all sampled depths under oxygenated conditions in FCR and CCR. Birnessite precipitation is favored by several orders of magnitude over precipitation of hausmannite minerals. In contrast, conditions are unfavorable for precipitation of rhodochrosite (see Appendix I).

4.0 Discussion

In the following sections, we discuss drivers of Mn removal under HOx operation in lakes and reservoirs of different geochemical conditions. We hypothesize mechanisms of rapid Mn removal in high pH and moderate or high alkalinity solutions. We also address how the presence of particulate matter (>0.45 μm) impacts Mn removal rates in the water columns of FCR and CCR, and potential mechanisms of Mn removal by particulate matter. Finally, we describe implications of our study for drinking water treatment, discuss our study limitations and list outstanding questions.

4.1 Elevated pH and alkalinity can enhance rapid Mn removal in freshwaters

Our pH and alkalinity laboratory experiments shed light on the independent impacts of pH and alkalinity on Mn removal rate, and how these drivers act together. Our observations support our initial hypothesis that the combination of elevated pH and alkalinity in freshwater accelerate Mn removal. Considering the composition of our experimental solutions, the potential mechanisms of Mn removal are limited to: oxidation of Mn(II) by oxygen to form Mn oxides (see Equation 1); soluble Mn(II) precipitation as rhodochrosite upon reaction with carbonates; and sorption or mineral-catalyzed oxidation of Mn(II) by Mn oxides formed through oxidation by oxygen (see Equation 2).

We propose that Mn removal in our experiments occurs by Mn oxidation in high pH and moderate or high alkalinity solutions based on elemental analysis, geochemical modeling and qualitative observations of particles (Figures 7-10). Both macroscopic and microscopic particles contained an abundance of Mn and oxygen but a lack of carbon, which is consistent with formation of Mn oxides in solution (Figure 7, 8). The lack of carbon detected on particle surfaces indicates that rhodochrosite precipitation did not occur in detectable quantities (Figure 7). Our

identification of Mn oxidation as the primary removal mechanism is supported by geochemical favorability of mineral precipitation reported in previous studies and visual observation of particles in our experiments (Hem 1963, Hem and Lind 1983). Increasing alkalinity under high pH conditions promotes Mn removal by accelerating oxidation and subsequent Mn oxide precipitation, rather than increasing favorability of Mn oxide precipitation (see section 3.2.3).

The morphology and color of macroscopic particles observed in our high pH and moderate or high alkalinity solutions matches those of Mn oxides formed in previously reported synthetic solution and lake or reservoir water laboratory experiments, including Hem (1963), Tipping et al. (1984) and Learman et al. (2011). Discoloration followed by macroscopic particle aggregation in high pH and moderate or high alkalinity solutions resembles the evolution documented by Learman et al. (2011) (Figure 7, 8). In experiments examining Mn oxide catalysis of Mn oxidation, Learman et al. (2011) identified Mn oxides or hydroxides in the microscopic particles discoloring the solution and in the macroscopic particles that subsequently formed. Hem and Lind (1983) and Hem (1963) reported on the greater favorability of Mn oxidation over rhodochrosite precipitation under basic (pH>7.5) and oxic conditions. Considering the oxygenation maintained in laboratory experiments via agitation, rhodochrosite precipitation should not have been expected in our laboratory experiments (Hem 1963, Hem and Lind 1983). We conclude high pH and moderate to high alkalinity did not contribute to Mn removal via rhodochrosite precipitation or mineral catalysis of Mn oxidation by rhodochrosite, as proposed by Diem and Stumm (1984).

In high pH solutions, moderate to high alkalinity maintained initial high pH conditions for the duration of our laboratory experiments, in contrast to the pH drop in un-buffered high pH experiments (Figure 4). Even 0.5-1 unit drop in pH can substantially slow Mn oxidation (Hem

1963). Therefore, our results suggest that alkalinity accelerates Mn removal in solution by maintaining pH conditions that are favorable to faster Mn oxidation.

Our solution chemistry results are consistent with initial Mn oxide formation in solution driving rapid removal by sorption or mineral catalysis of Mn oxidation. The near-total removal of soluble Mn within 2 hours in solutions of high pH and moderate to high alkalinity suggests sorption and/or mineral catalysis of Mn oxidation by initially formed Mn oxides (Figure 5, Equation 2). The catalysis of Mn oxidation by Mn oxides and hydroxides has a half life of several hours, faster than the uncatalyzed oxidation of Mn under pH 10 conditions (Learman et al. 2011). Our Mn concentration time series for the 24-hour high pH and moderate alkalinity solutions shows the fastest Mn removal rates initially, before removal rates slow as soluble Mn concentrations decrease (Figure 5). This removal trend is consistent with expectations for mineral catalysis of oxidation by Mn oxides, as removal is fastest when soluble Mn(II) is abundant but slows once less Mn(II) remains (Bethke 2007).

Our data cannot elucidate whether Mn oxide particles drove further Mn removal via mineral catalysis, sorption or both. Quantifying Mn removal by each mechanism is difficult without titration of particles for their average oxidation state or analysis by X-ray photoelectron spectroscopy (Hem 1963). Mn(II) sorption is not accompanied by a change in oxidation state, but Mn oxidation transforms Mn(II) into Mn(III) or Mn(IV). Therefore, a low average oxidation state of particles would reflect dominance of sorption over oxidation (Hem 1963). Sorption and Mn oxidation by oxygen both grow more favorable under the high pH conditions in which we observed rapid Mn removal, with the point of zero charge for MnO_2 reported at values ranging from pH 2.4-6 (reviewed by Adams et al. 2009). In addition, Mn sorption precedes Mn catalysis by Mn oxides, making the separate study of these removal mechanisms difficult (see Equation

2). Distinguishing between removal mechanisms has implications for freshwater Mn cycles – sorbed Mn remobilizes more readily than oxidized Mn (Hsiung and Tisue 1994).

4.2 Differences in pH and alkalinity between FCR and CCR exert insignificant influence on Mn removal

We conducted pH-alkalinity laboratory experiments in synthetic solutions and reservoir water to evaluate geochemical drivers of Mn removal in drinking water reservoirs. Based on the results of these experiments, we hypothesized that the combination of higher pH and alkalinity in CCR enhances Mn removal in CCR relative to FCR. However, our field monitoring results do not support this hypothesis. Our pH measurements and alkalinity titrations confirm previous observations of higher pH and alkalinity in CCR compared to FCR, though historical monitoring recorded greater differences in pH and alkalinity between reservoirs (Figures 17, 18). The median hypolimnetic pH of FCR was 6.85 and 7.38 in CCR during our 2022 monitoring period. During the 2022 monitoring period, the median hypolimnetic alkalinity was 22.6 mg/L $CaCO_3$ and 44.1 mg/L $CaCO_3$ in FCR and CCR, respectively. At pH and alkalinity approaching reservoir conditions reported in 2022 or prior, we observed no significant difference in Mn removal rate over 14 days. Our pH-alkalinity experiments show no significant difference in Mn removal rate between 0 and 200 mg/L $CaCO_3$ alkalinity at pH 8, or in any solutions of pH 6-8 (Figure 4). Therefore, our data do not support our initial hypothesis that pH and alkalinity differences in FCR and CCR contribute substantially to differences in Mn removal rate.

4.3 Differences in HOx operation and other environmental factors may drive Mn removal outcomes

Several confounding factors present in the environments of FCR and CCR make cross-reservoir comparisons difficult, including differences in HOx operation, presence of particles in

the water column and potential differences in microbial communities. During 2022, the HOx system in FCR experienced intermittent outages and operated under limited capacity for much of the stratified period, when we monitored water column Mn concentrations for comparison to CCR. Starting oxygenation before the onset of anoxia and continuing oxygenation without disruption throughout stratification is critical for effective Mn control under HOx operation (Bard et al. 2012, Preece et al. 2019). Thus, maintenance and intermittent operation of the HOx system in 2022 at FCR likely impaired the system's ability to control Mn release and removal. By contrast, the HOx system in CCR operated at full capacity throughout the stratification period and continued oxygenating the hypolimnion at reduced capacity in winter.

The influences of biotic drivers on Mn removal have not been compared in FCR and CCR, despite evidence in the literature that microbes accelerate Mn oxidation by several orders of magnitude (Chapnick et al. 1982, Tebo et al. 2004). Prior work in FCR by Munger et al. (2016) detected the presence of Mn oxidizing microbes within the reservoir, and their accelerating effect on Mn oxidation. Greater density of Mn-oxidizing microbes in the water column of one reservoir would contribute to faster Mn removal, independent of geochemistry or HOx operation.

4.3.1 Particulate matter in reservoir water may influence Mn removal

Mn removal was only observed in unfiltered FCR and CCR reservoir water experiments, with insignificant Mn removal observed in filtered solutions over 10 days (Figure 6). Therefore, we propose that particles over 0.45 μm in diameter may be an important driver of Mn removal in FCR and CCR (Figure 6). The particles present in our experiments included minerals, organic matter and other suspended solids, all of which may drive Mn removal through separate pathways. Suspended particles in FCR may catalyze Mn oxidation and subsequent precipitation

as Mn oxides such as birnessite, a common Mn sheet mineral found at the oxic-anoxic boundary in lakes and reservoirs (Figure 14, Elzinga 2016). Within our unfiltered experiments, imaging and elemental analysis of macroscopic particles suggest that Mn oxides likely coat or nucleate on suspended particles (Figure 11, 12). We interpret the aluminum and/or silicate-rich plates and blocks in our particles as primarily quartz and clay minerals based on XRD analysis of CCR sediment (Figure 11, 12, S1). Clay minerals – detected in surficial CCR sediments by this study – can catalyze Mn oxidation (Hsiung and Tisue 1994). The occurrence of Mn in close association with Al and Si in our element maps is consistent with observations of preferential Mn oxide coating on quartzite and shale particles by Adams et al. (2009) (Figure 11). At high magnification of Mn oxide regions on the particles, the globular textures we observed are similar to Mn oxide textures reported in Adams et al. (2009) (probable birnessite) and Sánchez-España and Yusta (2019) (asbolane).

Our results suggesting enhanced Mn removal by suspended particles in our unfiltered reservoir experiments are consistent with previous work on Mn in freshwaters that documented Mn oxidation's high sensitivity to particle catalysis (Hsiung and Tisue 1994, Godwin et al. 2020). Godwin et al. (2020) proposed greater density of suspended particles as one explanation for much greater Mn oxidation in the Western Basin of Lake Erie compared to the Eastern Basin. However, the results of this study do not address how the compositions of suspended particles in each reservoir may drive different Mn removal outcomes. Madden and Hochella (2005) demonstrated that smaller particles have greater capacity to catalyze Mn oxidation, while other studies reported that some catalyzing minerals accelerate Mn oxidation faster than others (Lan et al. 2017, Learman et al. 2011).

We observed higher rates of Mn removal in unfiltered experiments with FCR water relative to CCR water experiments, a difference possibly due to suspended particle densities in the water we collected for our experiments. However, using higher turbidity as a rough proxy for greater suspended particle density in the reservoir water column, our comparisons of 2013-2022 turbidity data from FCR and CCR shows marginally higher turbidity in FCR at the depths sampled for our experiments (Figure 19, Carey et al. 2023). Thus, it is currently unclear if the enhanced Mn removal in FCR vs. CCR is influenced by particle density.

4.4 Implications for HOx operation and Mn removal

Our results support the importance of considering lake or reservoir biogeochemical conditions for optimal Mn removal under HOx operation. We observed in our experiments that Mn removal rates proceed slowly at circumneutral pH (6.5-8) and alkalinity conditions typical of FCR and CCR (0-100 mg/L $CaCO_3$) (Figure 4). However, the presence of particles and microbes in the water column can promote Mn removal within days, timescales most relevant for water quality control (Figure 6). The difficulty of removing soluble Mn from water at pH and alkalinity conditions in most lakes and reservoirs reinforces the necessity of beginning HOx operation before anoxia leads to Mn release from sediments (Preece et al. 2019).

4.5 Study limitations

We propose several key limitations of our work to contextualize interpretation of our results, and for improvement in future research. In this study, declines in soluble Mn were considered equivalent to Mn(II) removal, as done in previous studies (Munger et al. 2016, Godwin et al. 2020). All Mn which passed through the 0.22 μm filter was assumed to be Mn(II), with all oxidized Mn precipitated and removed. The filtration pore size of 0.22 μm that we used to separate soluble from particle Mn does not remove nano-scale Mn particles. Our TEM

imaging of particles from experimental solutions confirms the presence of nano-scale Mn crystals during incubation (Figure 8). Thus, defining Mn removal as the decline in Mn passing a 0.22 μm filter underestimates Mn removal. In a water treatment context, Tobiason et al. (2016) also describe the formation of colloidal and nanoparticle Mn oxides smaller than 0.22 um. Additionally, the process of altering the pH and alkalinity in our synthetic solution experiments introduces concentrations of sodium (Na) and potassium (K) much higher than those found in natural waters, which may impact the reactions occurring in solution. The high concentrations of Na and K raise the ionic strength of our experimental solutions, increasing the probability of aggregation (reviewed by Hotze et al. 2010). The presence of Mn(II) and Na together in solution promote aggregation by neutralizing negative charges on MnOx surfaces and compressing the electric double-layer between particles (Cheng et al. 2020). The concentration of Na in the high pH/moderate alkalinity and high pH/high alkalinity solutions exceeds the minimum needed to destabilize MnOx enough to promote MnOx aggregation (Cheng et al. 2020). Therefore, high Na concentrations may have partially contributed to the formation of microscopic and macroscopic aggregates in high pH/moderate alkalinity and high pH/high alkalinity solutions. In addition, Na often substitutes for Mn in Mn oxide minerals, including birnessite (Adams et al. 2009). We observed abundant sodium on the surface of macroscale particles from high pH and moderate or high alkalinity experiments. However, our elemental analysis does not allow us to conclude whether the sodium is a salt precipitated on pre-existing particles or a part of the Mn oxide.

5.0 Conclusions

Our primary study objective was to test the impacts of pH and alkalinity on Mn removal rate in freshwater to evaluate potential differences in Mn removal in two drinking water reservoirs (FCR and CCR) with HOx systems. Our experimental data demonstrate that high pH results in rapid abiotic Mn removal. Conditions of elevated alkalinity in addition to high pH promote faster Mn removal because alkalinity buffers pH. In high pH and moderate to high alkalinity experiments, rapid Mn removal coincided with formation of microscopic and macroscopic particles, suggesting Mn was removed by oxidation and precipitation as Mn(IV) oxides rather than Mn carbonate precipitation. Analyses using SEM, EPMA and TEM are consistent with our interpretations. Our results also suggest Mn oxides formed by initial Mn oxidation likely contributed to further Mn removal through mineral catalysis of additional Mn oxidation and sorption of Mn(II) in solution. Experiments using reservoir water demonstrate the importance of particulate matter for promoting Mn removal. Analyses of particles formed in reservoir water experiments show regions of Mn oxide alongside aluminosilicate or silicate minerals, likely quartz or clays. The close association of Mn oxide with quartz and clays is consistent with mineral catalysis of Mn oxidation or nucleation of Mn oxide precipitation. Overall, our experimental results support the importance of reservoir geochemistry, including pH, alkalinity and the presence of mineral particles, in facilitating Mn removal.

6.0 Figures

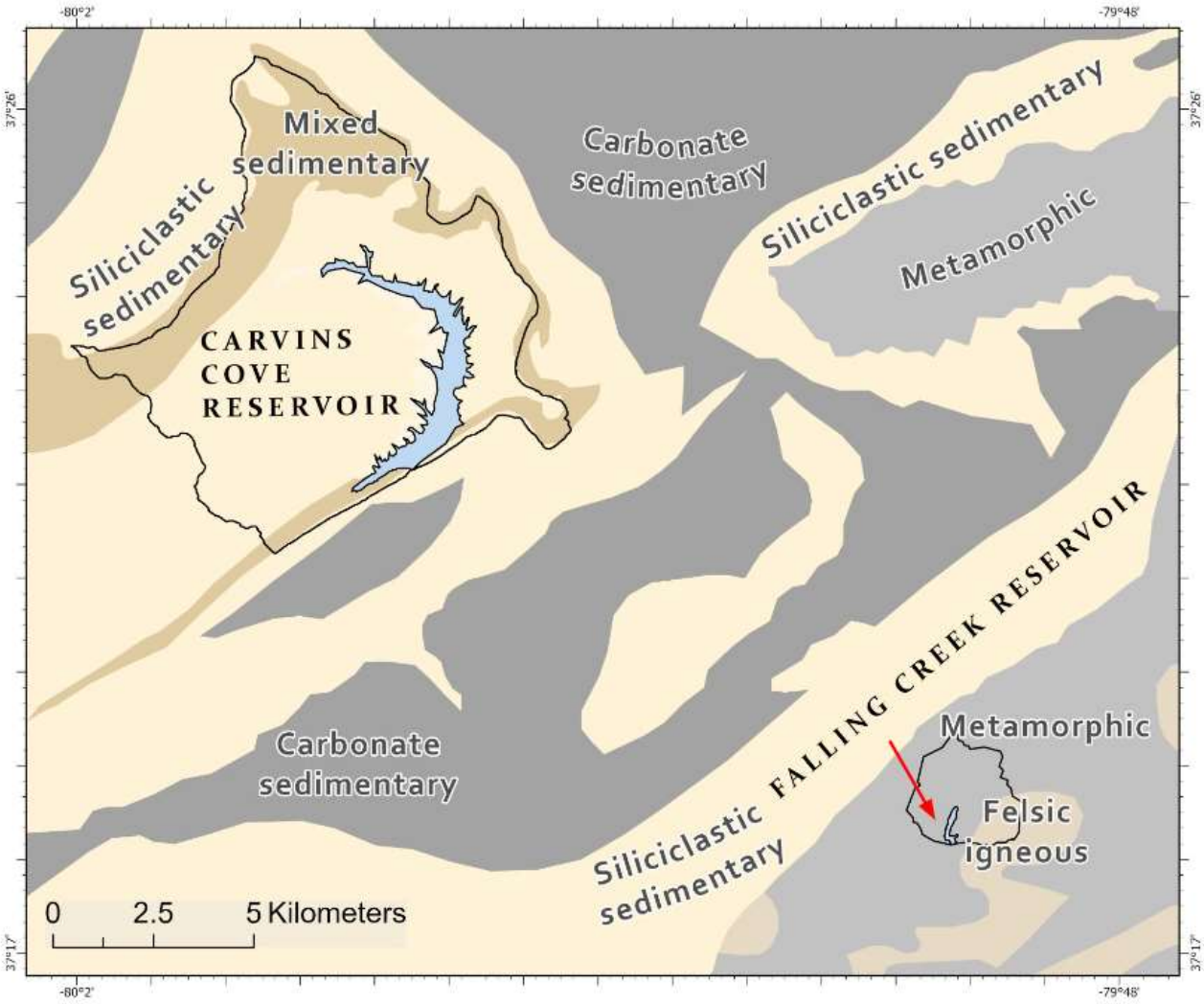

Figure 1: Bedrock lithology underlying the drainage basins of Falling Creek Reservoir (FCR) and Carvins Cove Reservoir (CCR). Tributary watersheds are outlined in black. Watershed boundaries were obtained from Carey et al. (2022b). Lithology data from Moosdorf et al. (2010).

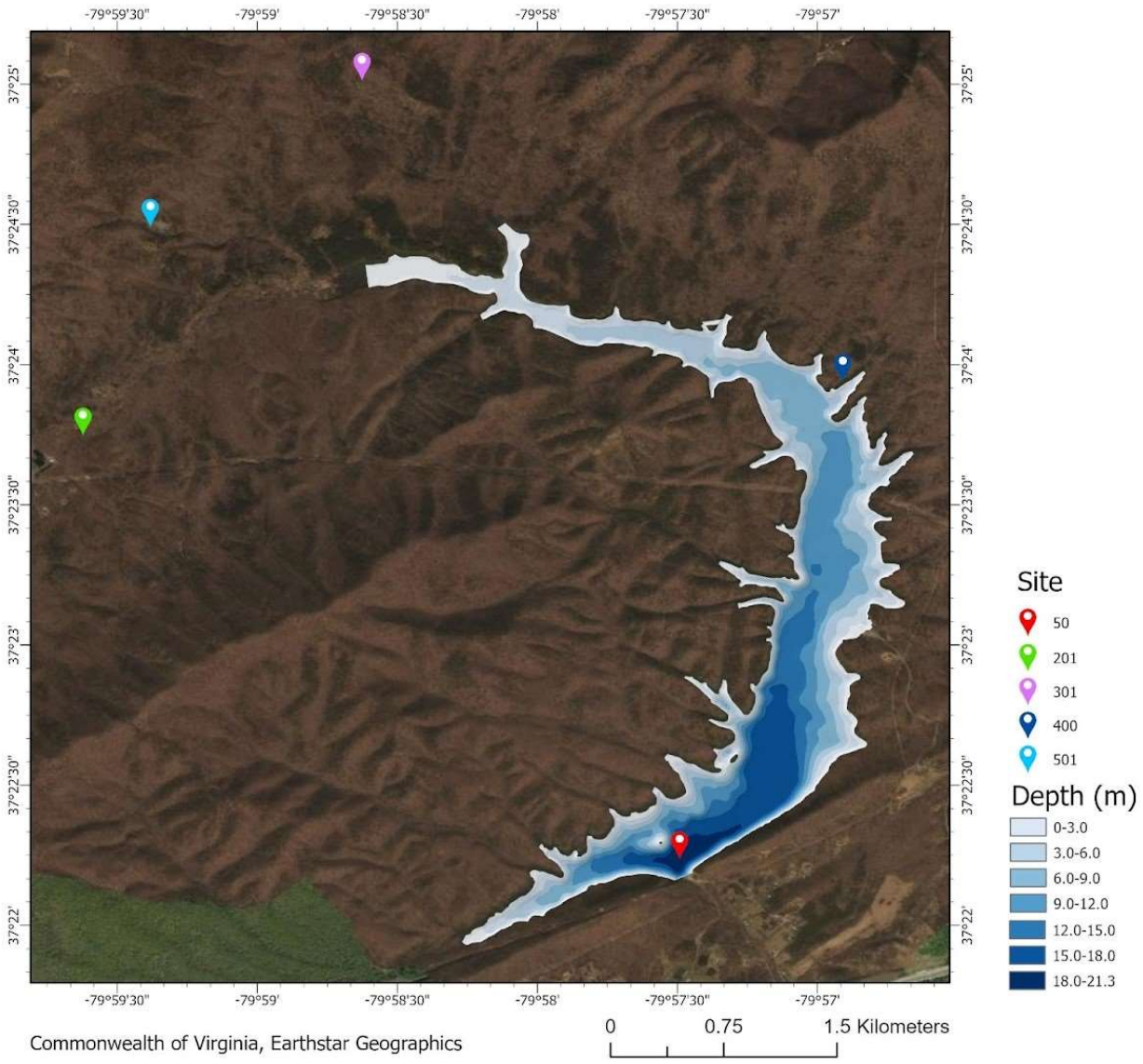

Figure 2: Map of sampling sites at Carvins Cove Reservoir (CCR) and tributaries overlaid on a reservoir bathymetric map. Water column sampling within CCR occurred at the deepest site (site 50). Basemap imagery from Commonwealth of Virginia and Earthstar Geographics.

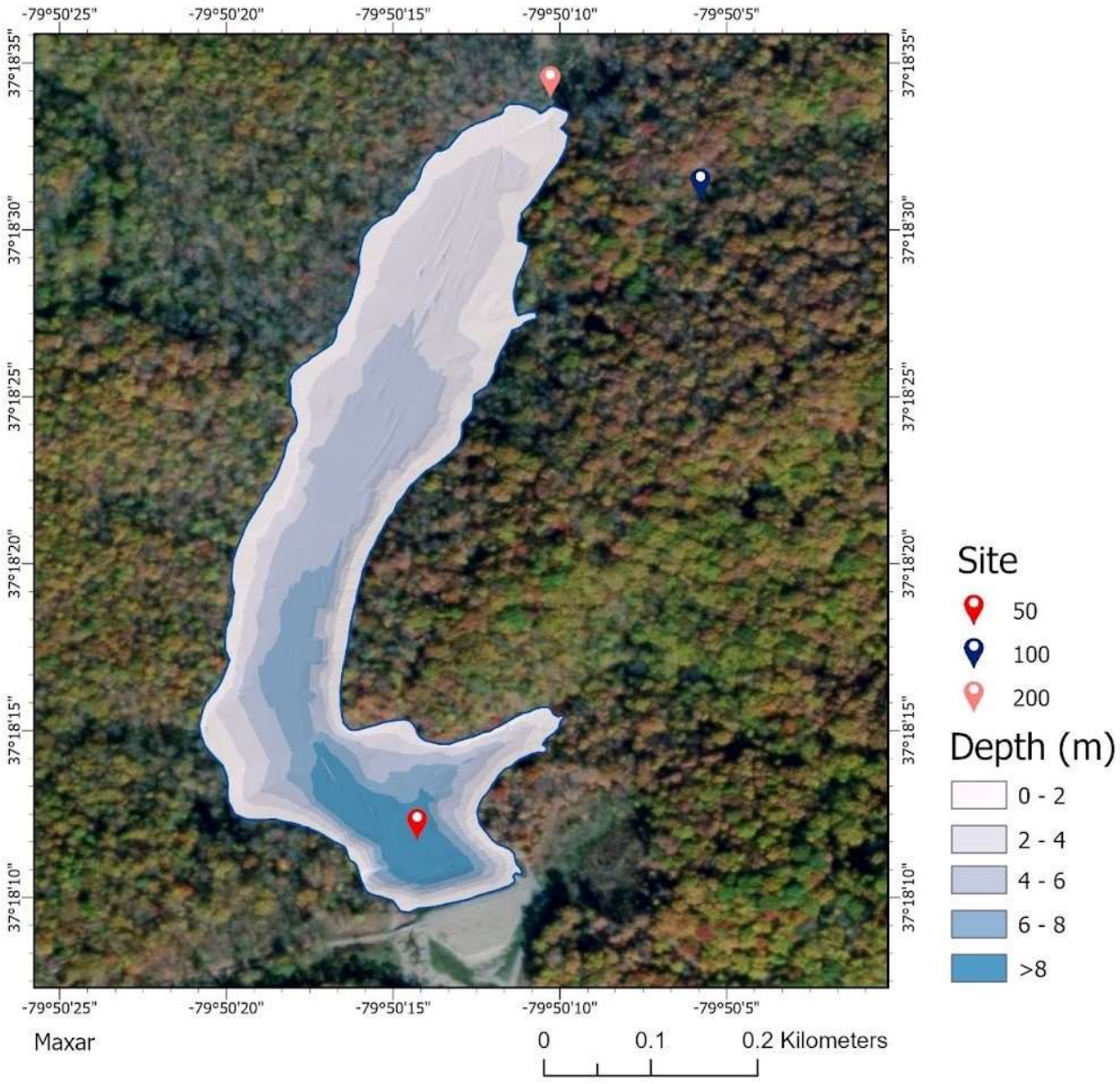

Figure 3: Map of sampling sites at Falling Creek Reservoir (FCR) overlaid on a reservoir bathymetric map. Water column sampling within FCR occurred at the deepest site (site 50). Basemap imagery from Maxar.

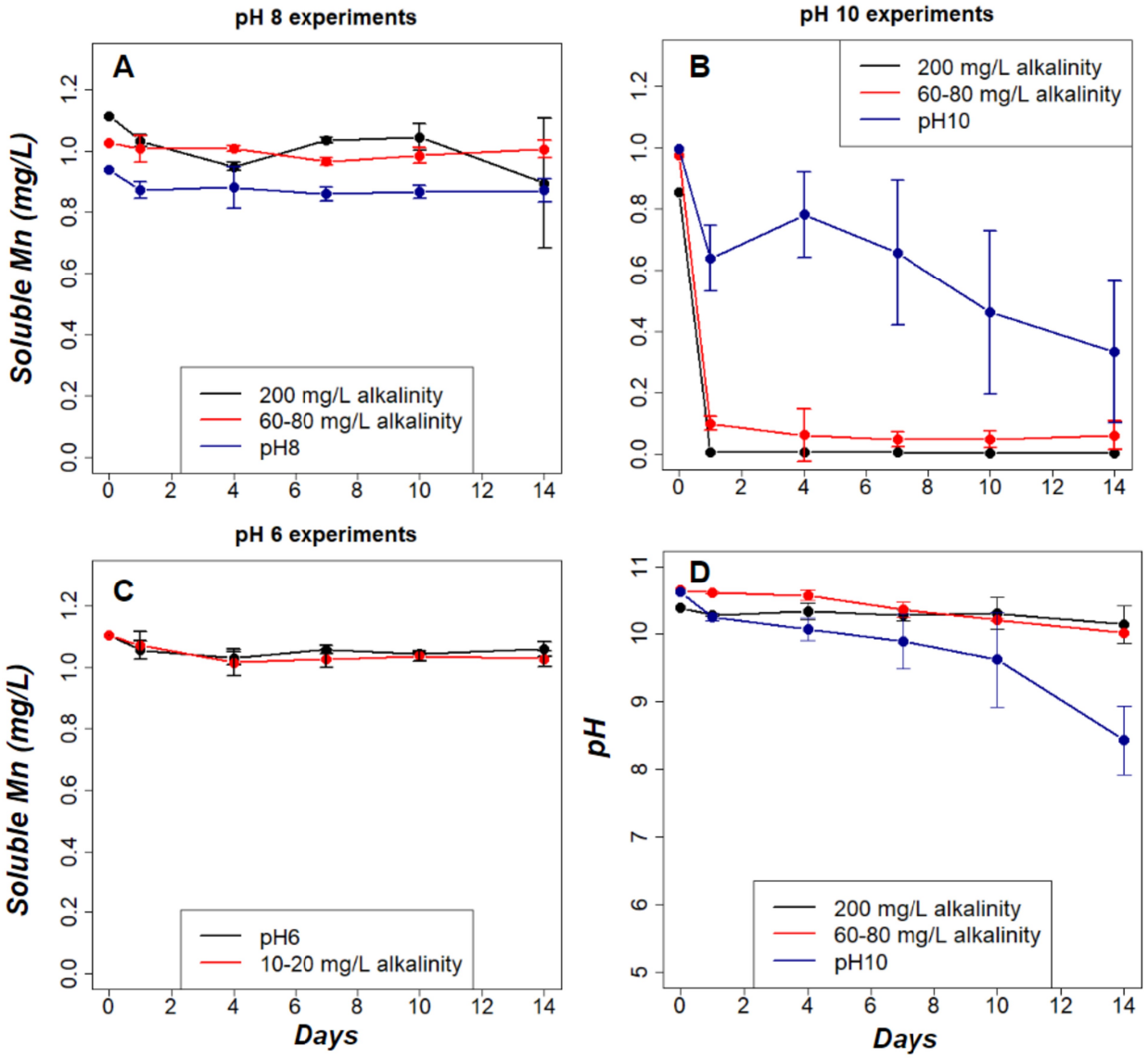

Figure 4: Soluble manganese (Mn) concentrations measured in all experiments and pH measured in high pH experiments for 14-day experiments. Error bars reflect standard deviation from triplicate experiments. A) Soluble Mn time series for pH 8 14-day experiments. All pH 8 solutions remained clear from day 0-14. B) Soluble Mn time series for high pH 14-day experiments. We observed translucent yellow-brown discoloration in the high pH/moderate alkalinity solution at 24 hours. Rusty brown to black aggregates formed in the high pH/high alkalinity solution by 24 hours. C) Soluble Mn time series for low pH 14-day experiments. Both

low alkalinity and control solutions remained clear from day 0-14. D) pH time series for pH 10 14-day experiments. Over 14 days, pH remains stable in high pH and moderate or high alkalinity solutions, but declines by over 1 unit in high pH solutions without alkalinity adjustment.

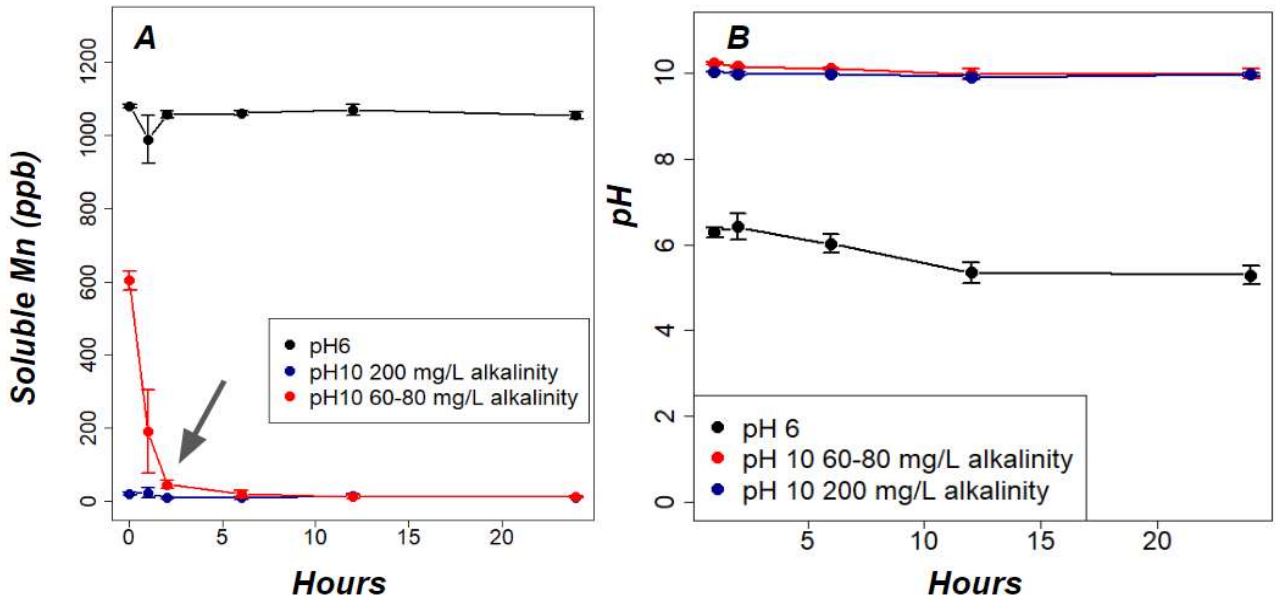

Figure 5: Soluble manganese (Mn) concentrations and pH measured in 24-hour experiments. Error bars reflect standard deviation from triplicate experiments. A) Averaged soluble Mn time series for 24-hour experiments. Mn removal rate is initially high, but decreases at 1 hour and 2 hours (indicated by black arrow). The high pH and moderate or high alkalinity solutions showed translucent yellow-brown discoloration at zero hours. Discoloration remained consistent in high pH/moderate alkalinity solutions, but intensified before decreasing upon macroscopic particle formation in high pH/high alkalinity solutions. Reddish-brown to black aggregates formed in both solutions by 12 hours. B) Averaged pH time series for 24-hour experiments.

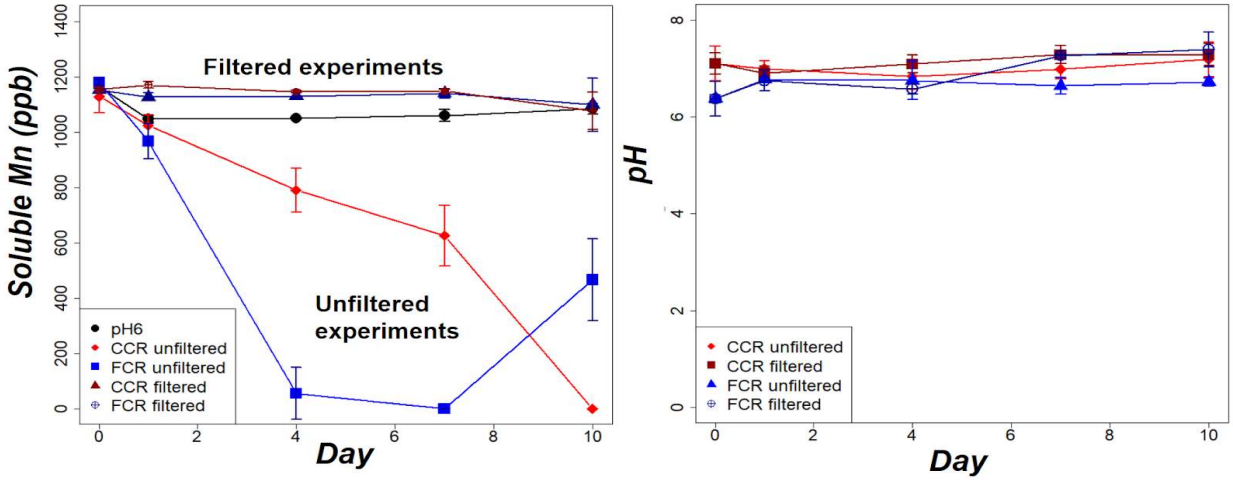

Figure 6: Soluble manganese (Mn) concentrations and pH measured in reservoir experiments. Error bars reflect standard deviation from triplicate experiments. A) Averaged soluble Mn concentration time series for reservoir water experiments. Filtered reservoir water and control solutions were initially clear without any visible particles. In unfiltered reservoir water, tan and black silt to fine sand-sized particles were observed at hour 0. Falling Creek Reservoir unfiltered water developed pink-orange translucent discoloration between day 1-4, while yellow-brown discoloration appeared in Carvins Cove Reservoir unfiltered water between day 4-7. Aggregated or silt-sized particles appeared in unfiltered reservoir water alongside discoloration. B) Averaged pH time series for reservoir water experiments.

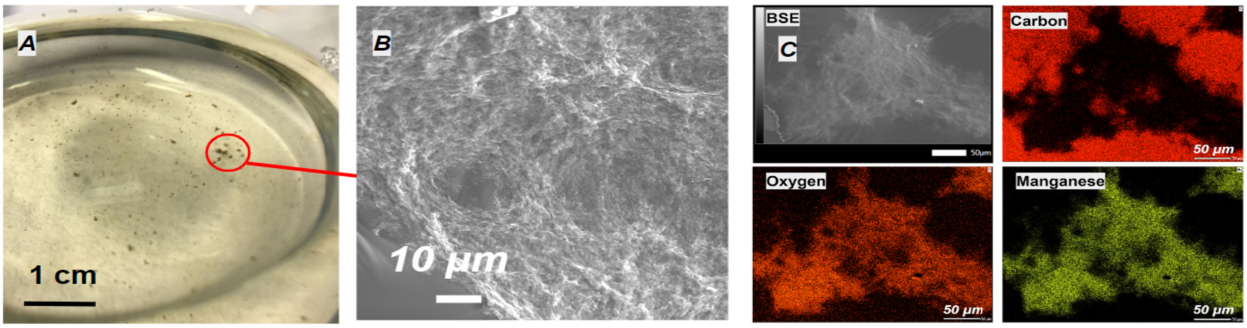

Figure 7: Scanning electron microscope (SEM) images and electron probe microanalyzer (EPMA) maps of particles collected from high pH/moderate alkalinity solution. A) High pH/moderate alkalinity solution photographed at 24 hours. B) Surface texture of macroscopic particles collected at conclusion of high pH/moderate alkalinity 24-hour laboratory experiments. Backscattered electron image (BSE) collected by SEM. C) Carbon (C), oxygen and manganese element maps of a representative macroscopic particle from high pH/moderate alkalinity solution. Maps collected by EPMA, BSE image collected by SEM. C surrounding the particle on the C map is from C coating and adhesive on the copper electrical tape used to mount particles.

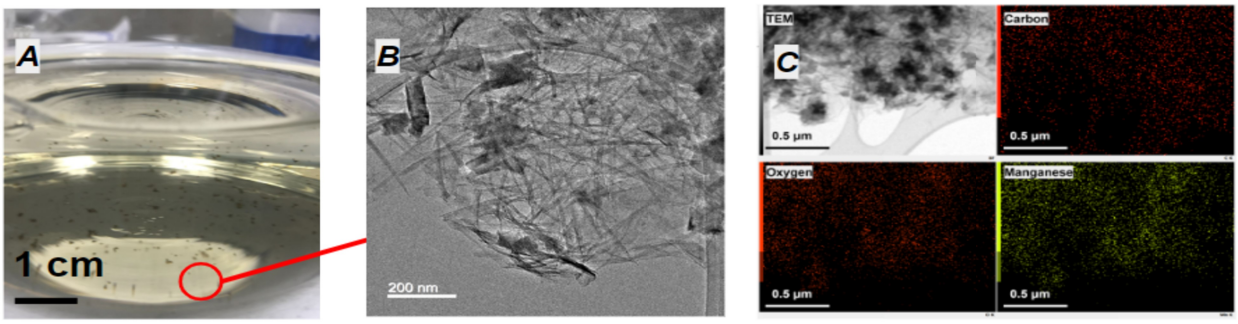

Figure 8: Transmission electron microscopy (TEM) images and energy dispersive spectroscopy (EDS) maps of microscopic particles suspended in discolored high pH/moderate alkalinity solutions. A) High pH/moderate alkalinity solution photographed at 12 hours. B) Brightfield TEM image showing aggregated needle-like crystals within micrometer-scale particles. C) Carbon, oxygen and manganese element maps of the particle shown in B. Maps collected by EDS. Carbon signal in element map likely introduced by lacy carbon grid.

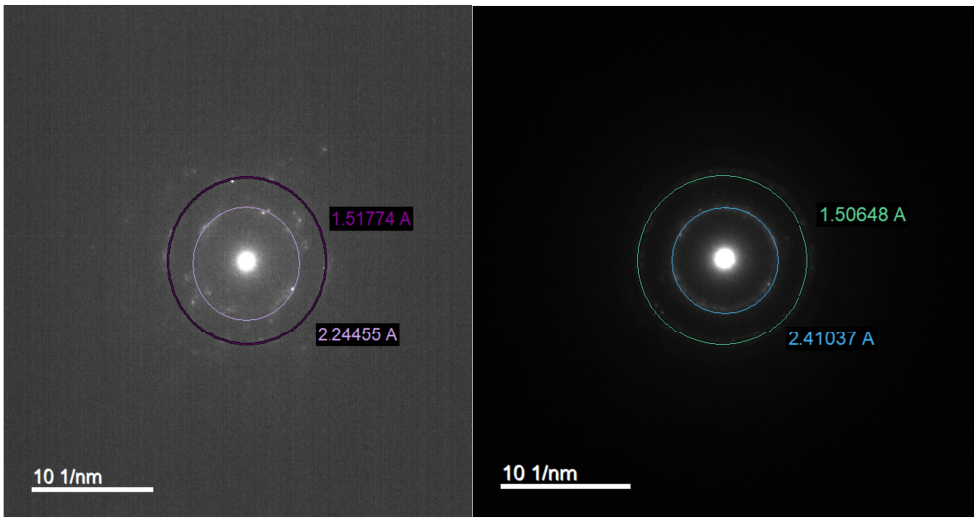

Figure 9: Diffraction rings obtained from selected area electron diffraction (SAED) of a particle collected from high pH/moderate alkalinity solution (see Figure 8).

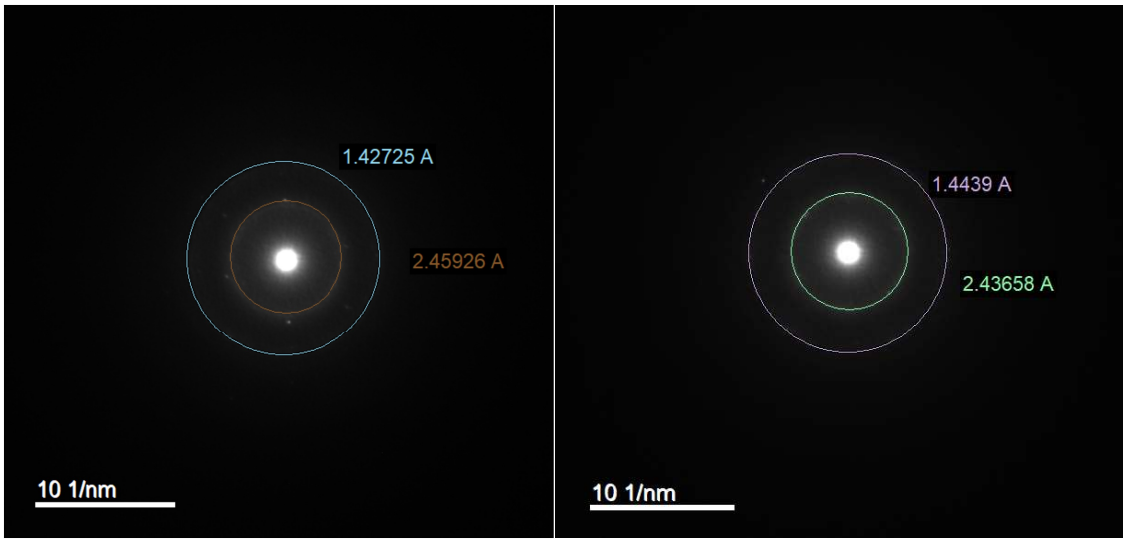

Figure 10: Diffraction rings obtained from selected area electron diffraction (SAED) of the particle collected from high pH/high alkalinity solution (see Figure S7).

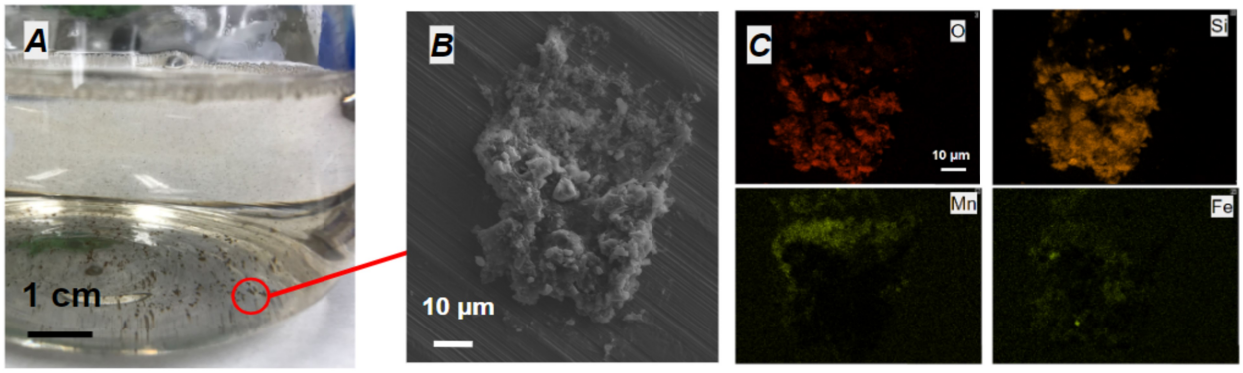

Figure 11: Falling Creek Reservoir (FCR) unfiltered reservoir water experiment. A) Reservoir water photographed at 4 days. B) Scanning electron microscopy of macroscopic particles formed in FCR unfiltered laboratory experiments and collected at 10 days. C) Silicon, iron, oxygen and manganese element maps of the particle shown in B. Maps collected by electron probe microanalyzer.

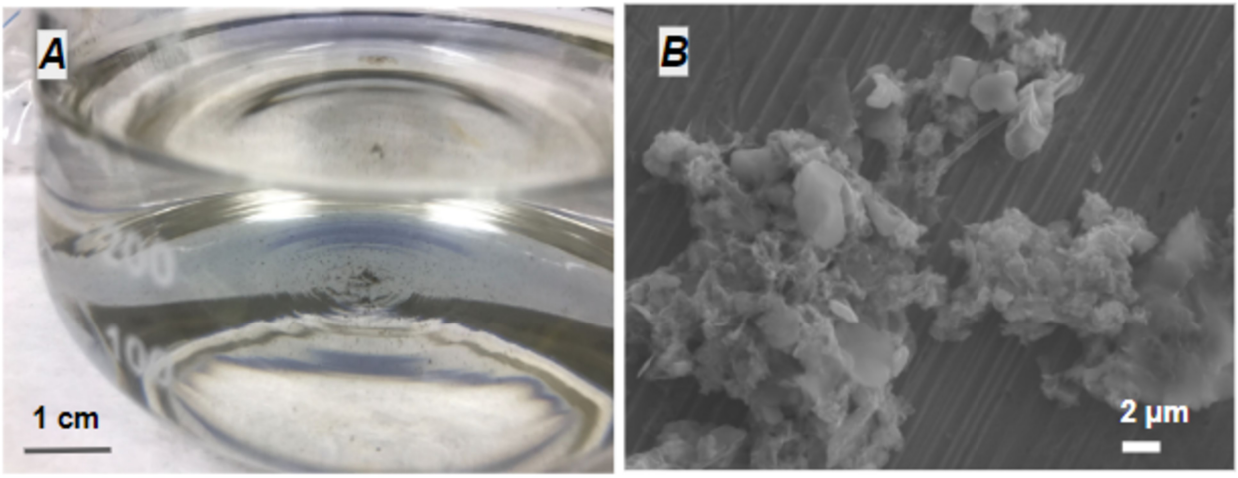

Figure 12: Carvins Cove Reservoir (CCR) unfiltered reservoir water experiment. A) Reservoir water photographed at 10 days. B) High magnification scanning electron microscopy image of visible particles formed in CCR unfiltered laboratory experiments and collected at 10 days.

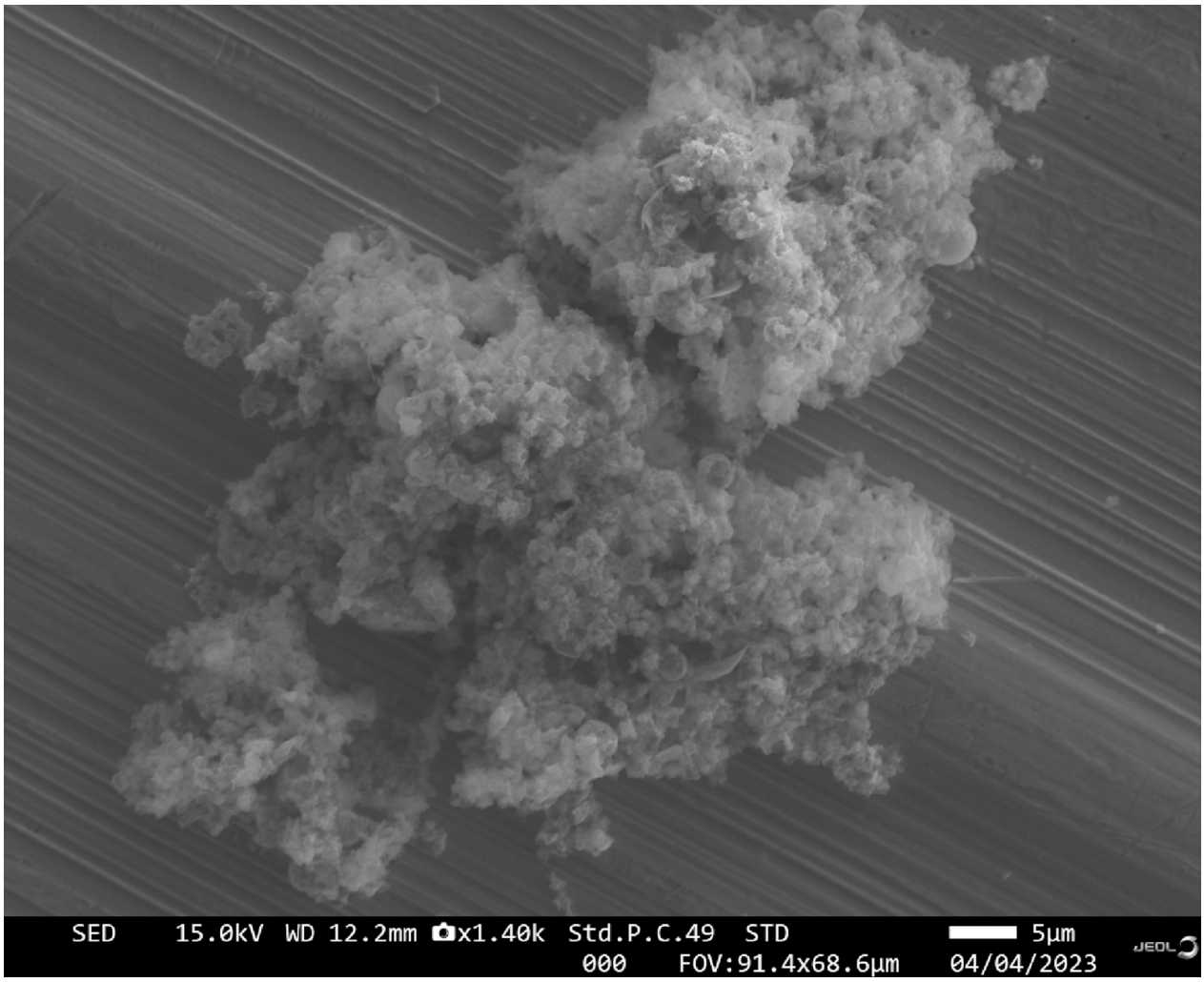

Figure 13: High magnification scanning electron microscopy image of a macroscopic particle formed in Falling Creek Reservoir filtered water laboratory experiments and collected at 10 days.

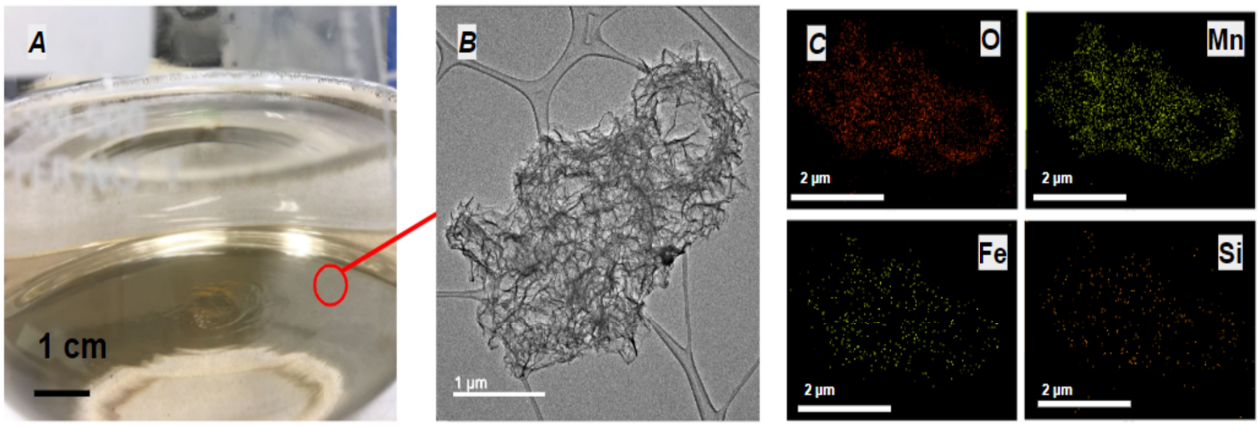

Figure 14: Falling Creek Reservoir (FCR) unfiltered reservoir water experiment. A) Reservoir water photographed at 4 days. B) Brightfield transmission electron microscopy (TEM) image showing crumpled sheet particles suspended within discolored solution collected at 4 days. C) Silicon, iron, oxygen and manganese element maps of the particle shown in B. Maps collected by energy-dispersive spectroscopy.

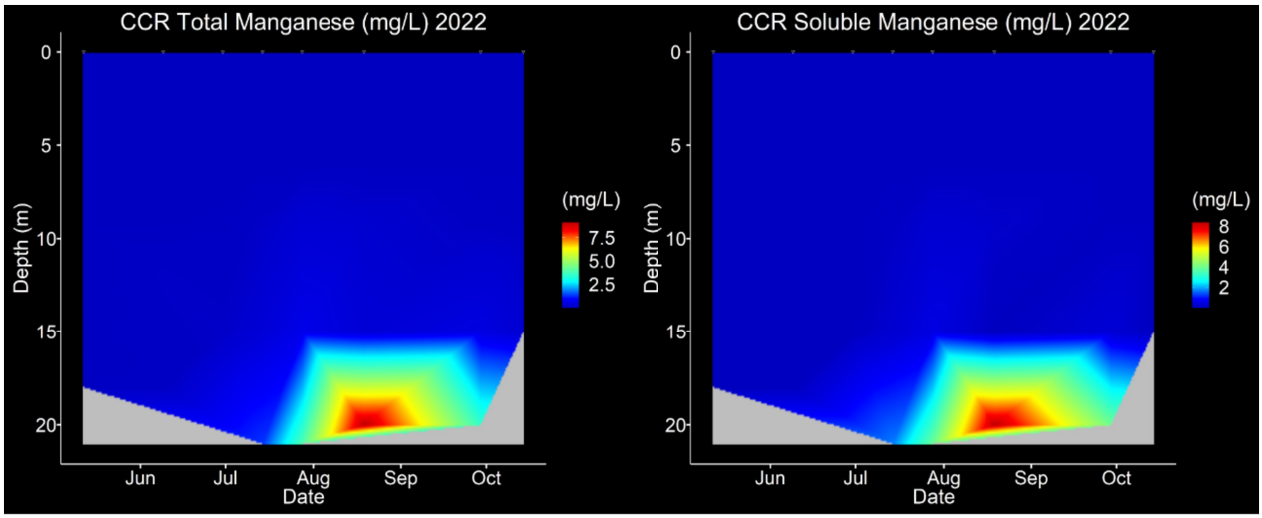

Figure 15: Heatmaps of total (left) and soluble (right) manganese (Mn) in the water column of Carvins Cove Reservoir (CCR) during the stratified period of 2022. Hypolimnetic oxygenation (HOx) was operational during the entire field season. Between sampling dates, we linearly interpolated Mn concentrations in the water column. Blank areas on the heatmap correspond to dates during which the lowest regularly sampled depth (20.0 m) was not sampled due to high sedimentation and organic matter in the lower water column.

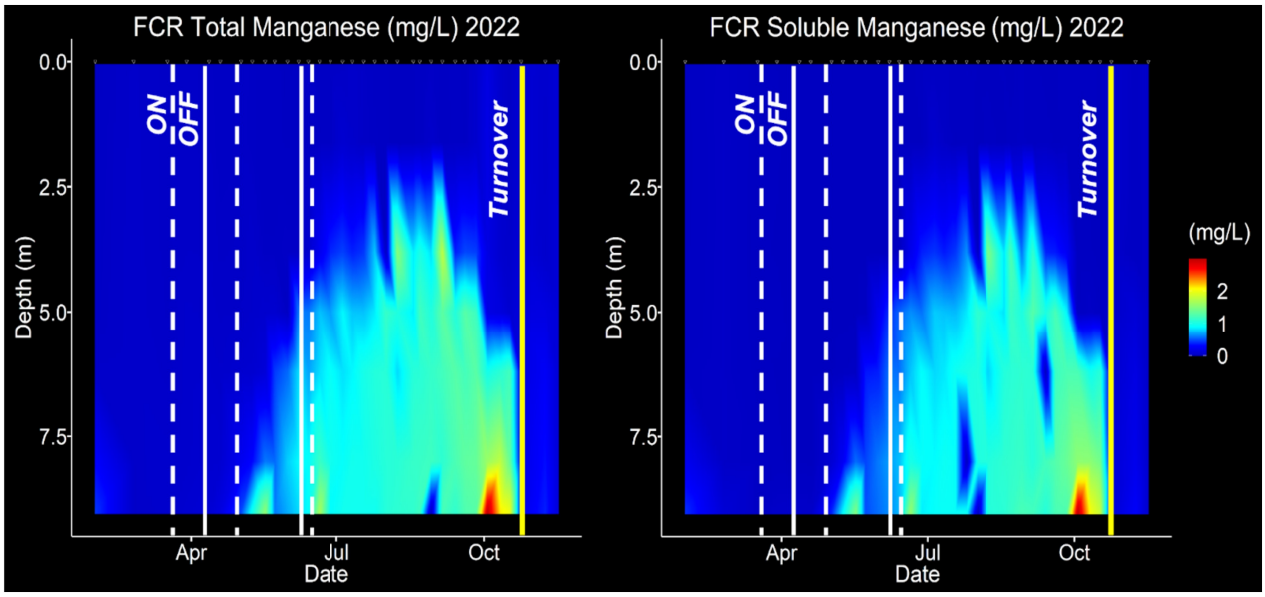

Figure 16: Heatmaps of total (left) and soluble (right) manganese (Mn) in the water column of Falling Creek Reservoir during the stratified period of 2022. Dashed white lines correspond to dates of HOx activation and solid white lines correspond to periods of HOx deactivation. The median depth of the hypolimnion is 3.8m. Between sampling dates, we linearly interpolated Mn concentrations in the water column.

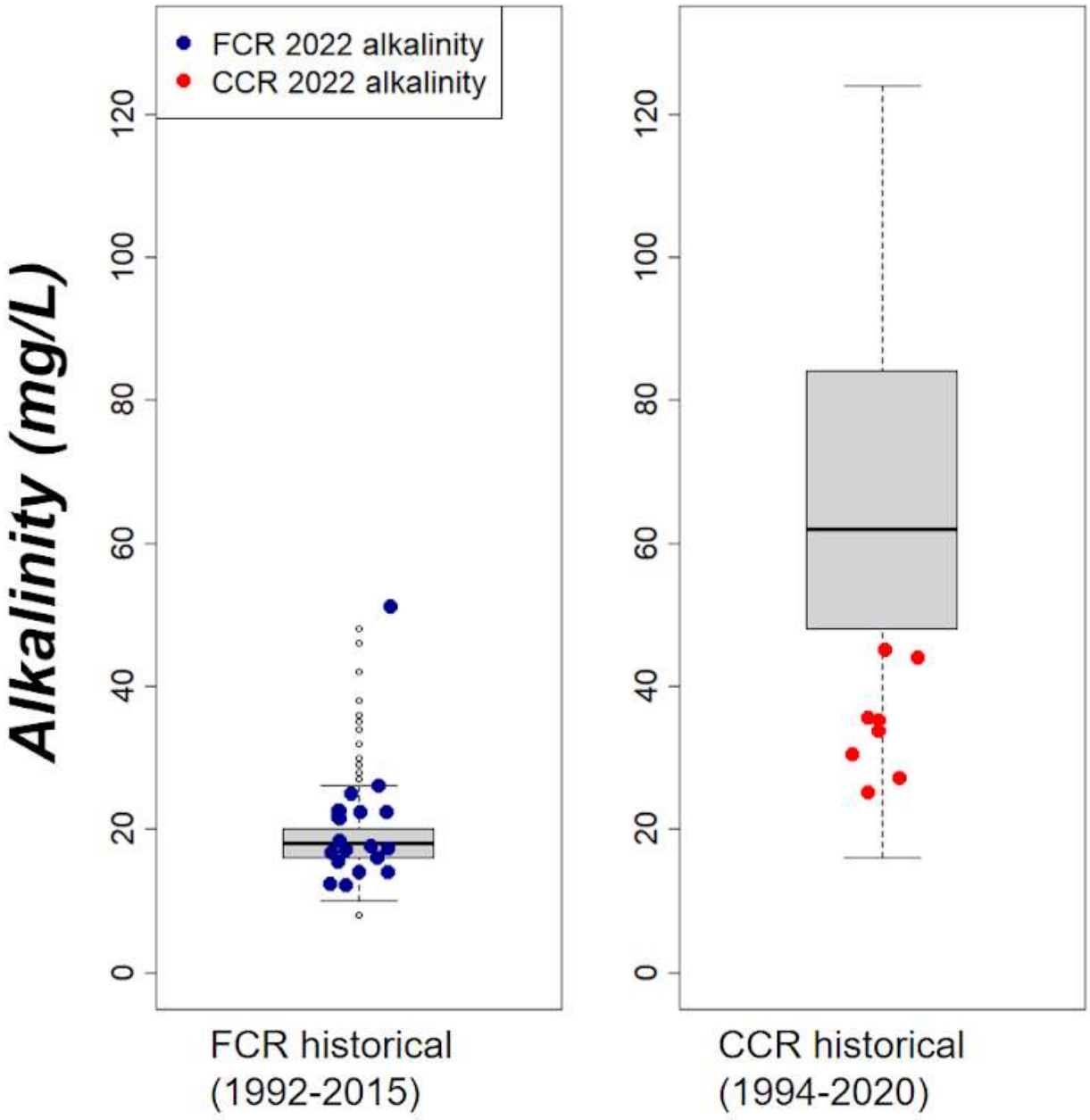

Figure 17: Boxplots of Falling Creek Reservoir and Carvins Cove Reservoir alkalinity (mg/L $CaCO_3$) compiled from historical Western Virginia Water Authority monitoring data, with 2022 alkalinity measured in this study shown as points.

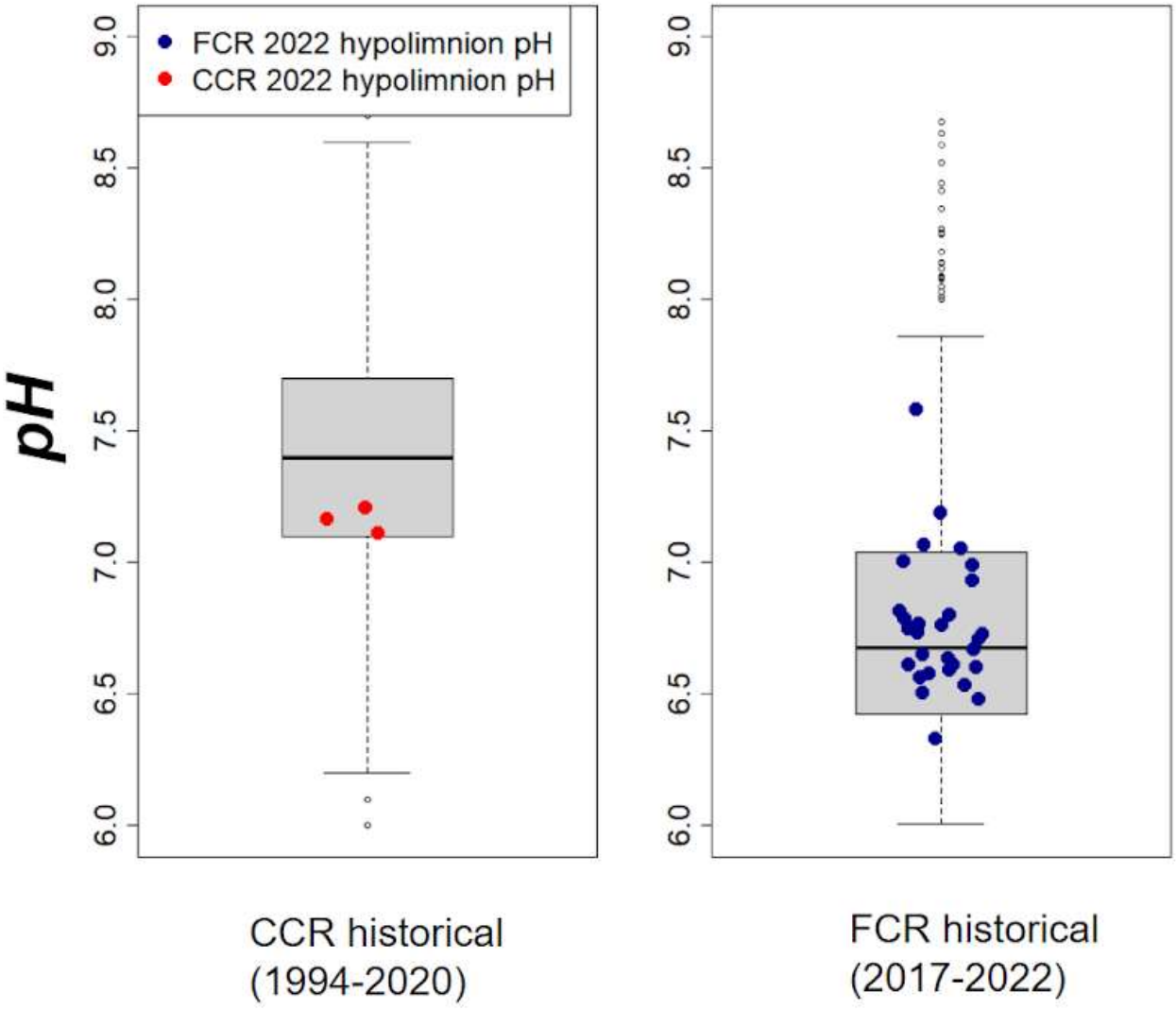

Figure 18: Boxplots of hypolimnetic pH in Falling Creek Reservoir (FCR) and Carvins Cove Reservoir (CCR). Historical data compiled from Western Virginia Water Authority monitoring for CCR and conductivity, temperature and depth meter profiles in FCR, with summer 2022 pH shown as points (Carey et al. 2023).

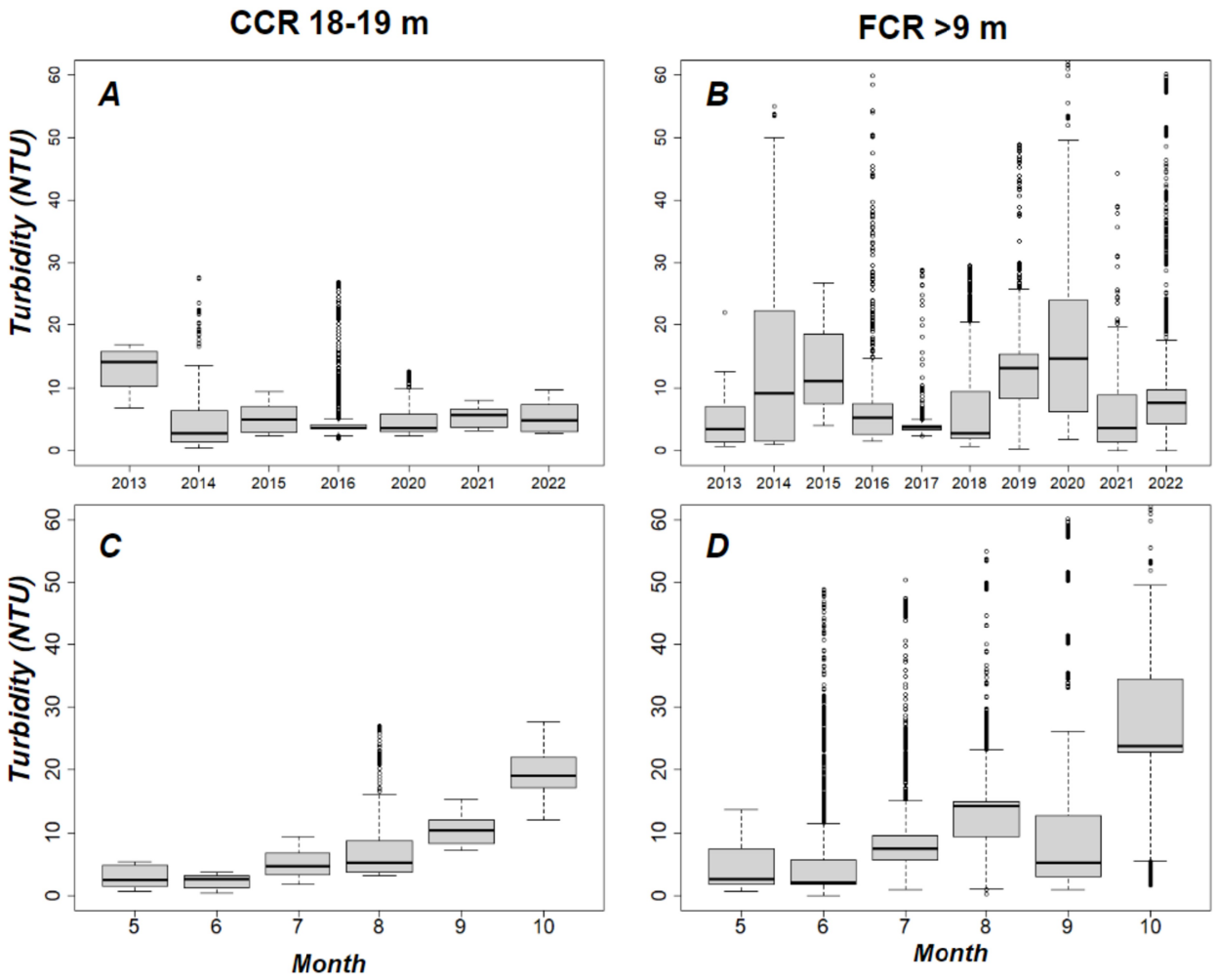

Figure 19: Boxplot of turbidity measurements by conductivity, temperature and depth meter (CTD) from 2013-2022 in Carvins Cove Reservoir (CCR) and Falling Creek Reservoir (FCR) (Carey et al. 2023). A) Turbidity values from 18-19 m in CCR grouped by year of monitoring. B) Turbidity values from 9-10 m in FCR grouped by year of monitoring. The larger spread of data in FCR is at least partly due to greater number of CTD casts throughout the year in FCR. C) Turbidity values from 18-19 m in CCR aggregated by month of year during the stratified period. D) Turbidity values from >9 m in FCR grouped by month of year during the stratified period.

Tables:

Table 1: HOx system design and reservoir characteristics of Falling Creek Reservoir and Carvins Cove Reservoir

	Falling Creek Reservoir (Gerling et al. 2014)	Carvins Cove Reservoir (Gantzer et al. 2009b, Man et al. 2020)
Maximum depth at full pond (m)	9.3	23
Surface area (km^2)	0.119	2.5
HOx system type	Side stream supersaturation	Linear diffuser
Depth of oxygen introduction (m)	8.5	~18
Designed daily oxygen input (kg/d)	25	Variable

Table 2: Falling Creek Reservoir and Carvins Cove Reservoir sampling site locations and descriptions (from Schreiber et al. 2023)

Reservoir	Site number	Description	Latitude	Longitude
CCR	50	Pelagic deep hole site of Carvins Cove Reservoir near dam; the closest access point to the dam via boat and 21 m at full pond	37.3706	-79.9582
CCR	201	Inflow stream site to Carvins Cove Reservoir at Carvins Creek Stream accessed via fireroad near red barns	37.3958	-79.9937
CCR	301	Inflow stream site to Carvins Cove Reservoir at Sawmill Branch inflow site upstream of reservoir where fire road bridge crosses the stream	37.4169	-79.9771
CCR	400	Inflow tunnel site to Carvins Cove Reservoir at emergence of Tinker Creek Tunnel	37.399	-79.9485
CCR	501	Inflow tunnel site to Carvins Cove Reservoir at emergence of Catawba Creek Tunnel	37.4082	-79.9897
FCR	50	Pelagic deep hole site nearest to Falling Creek Reservoir dam; at end of FCR catwalk	37.30325	-79.8373
FCR	100	Inflow stream site on Tunnel Branch primary inflow to Falling Creek Reservoir; long-term monitoring site where gauged weir is located	37.30858	-79.83494
FCR	200	Inflow stream site on Falling Creek secondary inflow to Falling Creek Reservoir; also referred to as the wetland stream	37.30943	-79.83619

Table 3: pH and alkalinity of starting conditions for 14-day experiments

Trial	Starting alkalinity (approx in mg/L $CaCO_3$)	Starting pH
High pH/high alkalinity	250 +/- 100	10.5 +/- 0.5
pH 8/moderate alkalinity	70 +/- 20	7.5 +/- 1*
pH 8/high alkalinity	250 +/- 100	8 +/- 0.5*
Low pH/ low alkalinity	20 +/- 10	6.5*
High pH/moderate alkalinity	70 +/- 20	10.5 +/- 0.5
High pH	20 +/- 10	10.5 +/- 0.5
pH 8	5 +/- 10*	8 +/- 0.5
Control	2 +/- 2	6 (+/- 0.5)*

*estimated based on chemical principles and preliminary trials

Table 4: pH and alkalinity of starting conditions for 24-hour experiments

Trial	Starting alkalinity (approx in mg/L $CaCO_3$)	Starting pH
High alkalinity/high pH	250 +/- 100	10.5 +/- 0.5
High pH/moderate alkalinity	70 +/- 20	10.5 +/- 0.5
Control	2 +/- 2	6 (+/- 0.5)

Table 5: Qualitative observations of selected 14-day experiment solutions

Days	High pH/high alkalinity	High pH/moderate alkalinity
0	Clear	Clear
1	Clear solution with loose aggregated black-rusty brown particles	Yellow-brown discoloration
4	Clear solution with disaggregated black-rusty brown particles	Yellow-brown discoloration
7	Clear solution with aggregated black-rusty brown particles	Yellow-brown discoloration
10	Clear solution with aggregated black-rusty brown particles	Yellow-brown discoloration
14	Clear solution with aggregated black-rusty brown particles	Yellow-brown discoloration

Table 6: Qualitative observations of 24-hour laboratory experiment solutions

Hours	High pH/high alkalinity	High pH/moderate alkalinity	Control
0	Yellow-brown discoloration	Yellow-brown discoloration	Clear solution
1	Yellow-brown discoloration	Yellow-brown discoloration	Clear solution
2	Yellow-brown discoloration	Yellow-brown discoloration	Clear solution
6	Yellow-brown discoloration	Yellow-brown discoloration	Clear solution
12	Yellow-brown discoloration with reddish brown-black aggregates	Yellow-brown discoloration with reddish brown-black aggregates	Clear solution
24	Yellow-brown discoloration with reddish brown-black aggregates	Yellow-brown discoloration with reddish brown-black aggregates	Clear solution

Table 7: Qualitative observations of reservoir water experimental solutions

Days	CCR unfiltered	FCR unfiltered	Control/FCR filtered/CCR filtered
0	Clear water with tan and black silt to sand sized particles	Clear water with tan and black silt to sand sized particles	Clear solution
1	Clear water with tan and black silt to sand sized particles	Clear water with tan and black silt to sand sized particles	Clear solution
4	Clear water with tan and black silt to sand sized particles	Pink-orange water with aggregated or silt-sized dispersed rusty brown to black particles	Clear solution
7	Slight brown-yellow discoloration of water with silt-sized dispersed brown to black particles	Pink-orange water with aggregated or silt-sized dispersed rusty brown to black particles	Clear solution
10	Slight brown-yellow discoloration of water with silt-sized dispersed brown to black particles	Pink-orange water with aggregated or silt-sized dispersed rusty brown to black particles	Clear solution

Table 8: Mn removal rates reported in the literature from laboratory experiments and field observations

Lake or Reservoir	Reference	pH	Zero-order Mn removal rate (mg/L/d)	First order Mn removal rate (d-1)	Second order Mn removal rate ($mg/L^{-1} hr^{-1}$)	Half-time (d)	Experiment type	Conditions
Falling Creek Reservoir	This study	6.53	-	0.050		0.58	Laboratory	Unfiltered reservoir water spiked with Mn
Carvins Cove Reservoir	This study	7.10	-	0.002		12.4	Laboratory	Unfiltered reservoir water spiked with Mn
N/A	This study	10.1			0.25			
Falling Creek Reservoir	Munger et al. (2016)	6.6	0.039			30	Laboratory	Reservoir water spiked with Mn
Falling Creek Reservoir	Munger et al. (2016)	6.8 (at 6.2 m)	0.014			33	Field observations	Intermittent HOx system deactivation
Lake Oneida	Chapnick et al. (1982)	8-8.4	0.016			1-2	Laboratory	Hypolimnetic water
Lake Richard B. Russell	Hsiung and Tisue (1994)	6.5	0.12				Laboratory	Unfiltered epilimnetic water – in equilibrium with O2
Lake Richard B. Russell	Hsiung and Tisue (1994)	6.5	0.02				Laboratory	Unfiltered epilimnetic water – in equilibrium with air

N/A	Learman et al. (2011)	7.6	0.99-1.62				Laboratory	Filtered artificial seawater spiked with 100 μM $MnCl_2$
N/A	Learman et al. (2011)	7.6	3.32-4.81				Laboratory	Filtered artificial seawater spiked with 100 μM $MnCl_2$ and birnessite colloids
Lake Erie, Western Basin (June)	Godwin et al. (2020)	8.23	0				Laboratory	Filtered hypolimnion water – light or dark conditions
Lake Erie, Western Basin (June)	Godwin et al. (2020)	8.23	0.035				Laboratory	Unfiltered surface mixed water – dark conditions
Lake Erie, Western Basin (June)	Godwin et al. (2020)	8.23	0-0.0088				Laboratory	Sterilized surface mixed water – dark conditions
Lake Erie, Western Basin (June)	Godwin et al. (2020)	8.23	0.051-0.069				Laboratory	Sterilized surface mixed water – light conditions
Lake Sempach	Friedl et al. (1997)	-				1.4	Field observations	Hypolimnetic water with bacteria
N/A	Diem and Stumm (1984)	8.4				>4 years	Laboratory	Sterile synthetic solution
N/A	Diem and Stumm	8.8				2-3	Laboratory	Sterile synthetic solution with

	(1984)							$NaHCO_3$ added to acheive rhodochrosite saturation
Lake Zurich	Diem and Stumm (1984)	7.5	0.0058			2-3	Laboratory	Spiked with Mn(II) and 25 mL bacteria-containing particle suspension
Lake Zurich	Diem and Stumm (1984)	7.5				>32	Laboratory	Spiked with Mn(II) and filtered

7.0 References

Adams, J.P., Kirst, R., Kearns, L.E., and Krekeler, M.P.S., 2009, Mn-oxides and sequestration of heavy metals in a suburban catchment basin of the Chesapeake Bay watershed: Environmental Geology, v. 58, p. 1269–1280, doi:10.1007/s00254-008-1628-y.

Adamo, T., 2020, Metrohm 930 Complex IC Flex Specs: University of Toronto TRACES Lab, Available at: utsc.utoronto.ca/~traceslab/PDFs/Metrohm_IC_Specs.pdf. (Accessed: 17th May 2023)

American Public Health Association (APHA), American Water Works Association, Water Environment Federation, 1998, Standard Methods for the Examination of Water and Wastewater, 20th ed. American Public Health Association, Washington, DC.

Austin, D., Scharf, R., Chen, C.-F., and Bode, J., 2019, Hypolimnetic oxygenation and aeration in two Midwestern USA reservoirs: Lake and Reservoir Management, v. 35, p. 266–276, doi:10.1080/10402381.2019.1599087.

Bethke, C.M., 2007, Geochemical and Biogeochemical Reaction Modeling: Cambridge University Press, doi:10.1017/CBO9780511619670.

Bryant, L.D., Hsu-Kim, H., Gantzer, P.A., and Little, J.C., 2011, Solving the problem at the source: Controlling Mn release at the sediment-water interface via hypolimnetic oxygenation: Water Research, v. 45, p. 6381–6392, doi:10.1016/j.watres.2011.09.030.

Carey, C.C. et al., 2022, Anoxia decreases the magnitude of the carbon, nitrogen, and phosphorus sink in freshwaters: Global Change Biology, v. 28, p. 4861–4881, doi:10.1111/gcb.16228.

[dataset] Carey, C.C., Lewis, A.S., Howard, D.W., Woelmer, W.M., Gantzer, P.A., Bierlein, K.A., Little, J.C., and WVWA., 2022b, Bathymetry and watershed area for Falling Creek Reservoir, Beaverdam Reservoir, and Carvins Cove Reservoir ver 1. Environmental Data Initiative, doi: 10.6073/pasta/352735344150f7e77d2bc18b69a22412

[dataset] Carey, C.C., Lewis, A.S.L., and Breef-Pilz, A., 2023, Time series of high-frequency profiles of depth, temperature, dissolved oxygen, conductivity, specific conductance, chlorophyll a, turbidity, pH, oxidation-reduction potential, photosynthetic active radiation, and descent rate for Beaverdam Reservoir, Carvins Cove Reservoir, Falling Creek

Reservoir, Gatewood Reservoir, and Spring Hollow Reservoir in southwestern Virginia, USA 2013-2022. Environmental Data Initiative, doi:10.6073/PASTA/5170B52F7514F54D834130DB0EFC5565.

Chapnick, S.D., Moore, W.S., and Nealson, K.H., 1982, Microbially mediated manganese oxidation in a freshwater lake1: Mn oxidation in Oneida Lake: Limnology and Oceanography, v. 27, p. 1004–1014, doi:10.4319/lo.1982.27.6.1004.

Cheng, H., Yang, T., Jiang, J., Lu, X., Wang, P., and Ma, J., 2020, Mn2+ effect on manganese oxides (MnOx) nanoparticles aggregation in solution: Chemical adsorption and cation bridging: Environmental Pollution, v. 267, p. 115561, doi:10.1016/j.envpol.2020.115561.

Davison, W., 1993, Iron and manganese in lakes: Earth-Science Reviews, v. 34, p. 119–163, doi:10.1016/0012-8252(93)90029-7.

Debroux, J.-F., Beutel, M.W., Thompson, C.M., and Mulligan, S., 2012, Design and testing of a novel hypolimnetic oxygenation system to improve water quality in Lake Bard, California: Lake and Reservoir Management, 28, 245–254, doi:10.1080/07438141.2012.716501.

De Vitre, R., and Davison, W., 1993, Manganese Particles in Freshwaters, *in* Revival: Environmental Particles, CRC Press, p. 36.

Diem, D., and Stumm, W., 1984, Is dissolved Mn2+ being oxidized by O2 in absence of Mn-bacteria or surface catalysts? Geochimica et Cosmochimica Acta, v. 48, p. 1571–1573, doi:10.1016/0016-7037(84)90413-7.

Downs, R.T., and Hall-Wallace, M., 2003, The American Mineralogist Crystal Structure Database. American Mineralogist, 88, 247-250.

Elzinga, E.J., 2016, 54 Mn Radiotracers Demonstrate Continuous Dissolution and Reprecipitation of Vernadite (δ-MnO 2) during Interaction with Aqueous Mn(II): Environmental Science & Technology, v. 50, p. 8670–8677, doi:10.1021/acs.est.6b02874.

EPA., 2021, Secondary Drinking Water Standards: Guidance for Nuisance Chemicals. Available at: https://www.epa.gov/sdwa/secondary-drinking-water-standards-guidance-nuisance-chemicals. (Accessed: 25th April 2023)

Friedl, G., Wehrli, B., and Manceau, A., 1997, Solid phases in the cycling of manganese in eutrophic lakes: New insights from EXAFS spectroscopy: Geochimica et Cosmochimica Acta, v. 61, p. 275–290, doi:10.1016/S0016-7037(96)00316-X.

Gantzer, P.A., Bryant, L.D., and Little, J.C., 2009, Controlling soluble iron and manganese in a water-supply reservoir using hypolimnetic oxygenation: Water Research, v. 43, p. 1285–1294, doi:10.1016/j.watres.2008.12.019.

Gantzer, P.A., Bryant, L.D., and Little, J.C., 2009b, Effect of hypolimnetic oxygenation on oxygen depletion rates in two water-supply reservoirs: Water Research, v. 43, p. 1700–1710, doi:10.1016/j.watres.2008.12.053.

[software] Gatan Digital Micrograph version 3.5. Pleasanton, California. Available from: https://www.gatan.com/products/tem-analysis/gatan-microscopy-suite-software

Gerling, A.B., Browne, R.G., Gantzer, P.A., Mobley, M.H., Little, J.C., and Carey, C.C., 2014, First report of the successful operation of a side stream supersaturation hypolimnetic oxygenation system in a eutrophic, shallow reservoir: Water Research, v. 67, p. 129–143, doi:10.1016/j.watres.2014.09.002.

Gerling, A.B., Munger, Z.W., Doubek, J.P., Hamre, K.D., Gantzer, P.A., Little, J.C., and Carey, C.C., 2016, Whole-Catchment Manipulations of Internal and External Loading Reveal the Sensitivity of a Century-Old Reservoir to Hypoxia: Ecosystems, v. 19, p. 555–571, doi:10.1007/s10021-015-9951-0.

Godwin, C.M., Zehnpfennig, J.R., and Learman, D.R., 2020, Biotic and Abiotic Mechanisms of Manganese (II) Oxidation in Lake Erie: Frontiers in Environmental Science, v. 8, p. 57, doi:10.3389/fenvs.2020.00057.

Hem, J., 1963, Chemical equilibria and rates of manganese oxidation: U.S. Geological Survey Water Supply Paper USGS Numbered Series, doi:10.3133/wsp1667A.

Hem, J.D., and Lind, C.J., 1983, Nonequilibrium models for predicting forms of precipitated manganese oxides: Geochimica et Cosmochimica Acta, v. 47, p. 2037–2046, doi:10.1016/0016-7037(83)90219-3.

Herndon, E.M., Havig, J.R., Singer, D.M., McCormick, M.L., and Kump, L.R., 2018, Manganese and iron geochemistry in sediments underlying the redox-stratified Fayetteville

Green Lake: Geochimica et Cosmochimica Acta, v. 231, p. 50–63, doi:10.1016/j.gca.2018.04.013.

Heu, R., Shahbazmohamadi, S., Yorston, J. and Capeder, P., 2019, Target Material Selection for Sputter Coating of SEM Samples. Microscopy Today 27, 32–36.

Hotze, E.M., Phenrat, T., and Lowry, G.V., 2010, Nanoparticle Aggregation: Challenges to Understanding Transport and Reactivity in the Environment: Journal of Environmental Quality, v. 39, p. 1909–1924, doi:10.2134/jeq2009.0462.

Hsiung, T.-M., and Tisue, T., 1994, Manganese Dynamics in Lake Richard B. Russell, *in* Environmental Chemistry of Lakes and Reservoirs, American Chemical Society, Advances in Chemistry 237, v. 237, p. 499–524, doi:10.1021/ba-1994-0237.ch016.

Kohl, P.M., and Medlar, S.J., 2006, Occurrence of manganese in drinking water and manganese control. American Water Works Association, Denver, Colorado.

Krueger, K.M., Vavrus, C.E., Lofton, M.E., McClure, R.P., Gantzer, P., Carey, C.C., and Schreiber, M.E., 2020, Iron and manganese fluxes across the sediment-water interface in a drinking water reservoir: Water Research, v. 182, p. 116003, doi:10.1016/j.watres.2020.116003.

Lan, S., Wang, X., Xiang, Q., Yin, H., Tan, W., Qiu, G., Liu, F., Zhang, J., and Feng, X., 2017, Mechanisms of Mn(II) catalytic oxidation on ferrihydrite surfaces and the formation of manganese (oxyhydr)oxides: Geochimica et Cosmochimica Acta, v. 211, p. 79–96, doi:10.1016/j.gca.2017.04.044.

Learman, D.R., Wankel, S.D., Webb, S.M., Martinez, N., Madden, A.S., and Hansel, C.M., 2011, Coupled biotic–abiotic Mn(II) oxidation pathway mediates the formation and structural evolution of biogenic Mn oxides: Geochimica et Cosmochimica Acta, v. 75, p. 6048–6063, doi:10.1016/j.gca.2011.07.026.

Madden, A.S., and Hochella, M.F., 2005, A test of geochemical reactivity as a function of mineral size: Manganese oxidation promoted by hematite nanoparticles: Geochimica et Cosmochimica Acta, v. 69, p. 389–398, doi:10.1016/j.gca.2004.06.035.

Man, X., Bierlein, K.A., Lei, C., Bryant, L.D., Wüest, A., and Little, J.C., 2020, Improved Modeling of Sediment Oxygen Kinetics and Fluxes in Lakes and Reservoirs: Environmental Science & Technology, v. 54, p. 2658–2666, doi:10.1021/acs.est.9b04831.

Manganese in drinking-water, 2021, World Health Organization Background document for development of WHO Guidelines for drinking-water quality Scientific brief WHO/HEP/ECH/WSH/2021.5, 68 p.

[dataset] Ming, C.L., and Schreiber, M.E, 2023, Time series of soluble Mn, pH, alkalinity and major elements in laboratory experiments testing pH, alkalinity and particle impacts on Mn removal ver. 1. Environmental Data Initiative. Retrieved from https://pasta-s.lternet.edu/package/eml/edi/1038/4

Moosdorf, N., Hartmann, J., and Dürr, H.H., 2010, Lithological composition of the North American continent and implications of lithological map resolution for dissolved silica flux modeling: LITHOLOGY AND DSi MODELING IN NORTH AMERICA: Geochemistry, Geophysics, Geosystems, v. 11, p. n/a-n/a, doi:10.1029/2010GC003259.

Munger, Z.W., Carey, C.C., Gerling, A.B., Hamre, K.D., Doubek, J.P., Klepatzki, S.D., McClure, R.P., and Schreiber, M.E., 2016, Effectiveness of hypolimnetic oxygenation for preventing accumulation of Fe and Mn in a drinking water reservoir: Water Research, v. 106, p. 1–14, doi:10.1016/j.watres.2016.09.038.

Preece, E.P., Moore, B.C., Skinner, M.M., Child, A., and Dent, S., 2019, A review of the biological and chemical effects of hypolimnetic oxygenation: Lake and Reservoir Management, v. 35, p. 229–246, doi:10.1080/10402381.2019.1580325.

[software] Putz, H., Brandenburg, K., GbR, Kreuzherrenstr., n.d., Match! - Phase Analysis using Powder Diffraction, Version 3.x [Software], Crystal Impact, 102, 53227 Bonn, Germany. Available from: https://www.crystalimpact.de/match.

Rimstidt, J.D., 2013, Geochemical rate models: an introduction to geochemical kinetics, 1st ed. Cambridge University Press, New York, New York.

Roland, J., 1970, Some effects of the introduction of hard water into Carvin Cove Reservoir, Virginia: Virginia Tech, 120 p.

Sánchez-España and Yusta, 2019, Coprecipitation of Co2+, Ni2+ and Zn2+ with Mn(III/IV) Oxides Formed in Metal-Rich Mine Waters: Minerals, v. 9, p. 226, doi:10.3390/min9040226.

[dataset] Schreiber, M.E., Ming, C.L., Hammond, N.W., Breef-Pilz, A., Geisler, B., and Haynie, G., 2023, Time series of total and soluble iron and manganese concentrations from Falling Creek Reservoir, Beaverdam Reservoir and Carvins Cove Reservoir in southwestern Virginia, USA from 2014 through 2022. Environmental Data Initiative, doi:10.6073/PASTA/9D901AE44871E018F475F42C58FB2004.

[software] Stroud Water Research Center, 2017, Model My Watershed. Available from https://wikiwatershed.org/

Tebo, B.M., Bargar, J.R., Clement, B.G., Dick, G.J., Murray, K.J., Parker, D., Verity, R., and Webb, S.M., 2004, BIOGENIC MANGANESE OXIDES: Properties and Mechanisms of Formation: Annual Review of Earth and Planetary Sciences, v. 32, p. 287–328, doi:10.1146/annurev.earth.32.101802.120213.

Tipping, E., Thompson, D.W., and Davison, W., 1984, Oxidation products of Mn(II) in lake waters: Chemical Geology, v. 44, p. 359–383, doi:10.1016/0009-2541(84)90149-9.

Tobiason, J.E., Bazilio, A., Goodwill, J., Mai, X., and Nguyen, C., 2016, Manganese Removal from Drinking Water Sources: Current Pollution Reports, v. 2, p. 168–177, doi:10.1007/s40726-016-0036-2.

UMass Amherst., 2016, Massachusetts Water Watch Partnership: pH and Alkalinity for Lakes. Available at: https://www.umass.edu/mwwp/protocols/lakes/ph_alkalinity_lake.html. (Accessed: 25th April 2023)

Wetzel, R.G., 2001, Limnology: lake and river ecosystems: San Diego, Academic Press, 1006 p.

Williams, D. B., and Carter, C. B., 1996, The Transmission Electron Microscope: A Textbook for Materials Science; Boston: Springer

Wittkop, C., Swanner, E.D., Grengs, A., Lambrecht, N., Fakhraee, M., Myrbo, A., Bray, A.W., Poulton, S.W., and Katsev, S., 2020, Evaluating a primary carbonate pathway for manganese enrichments in reducing environments: Earth and Planetary Science Letters, v. 538, p. 116201, doi:10.1016/j.epsl.2020.116201.

Woodward, H.P., 1932. Geology and Mineral Resources of the Roanoke Area. Virginia, Virginia Geological Survey, Richmond, VA.

Appendix A. Additional Falling Creek Reservoir (FCR) and Carvins Cove Reservoir (CCR) field monitoring data

We collected anion samples from the water column of FCR (collected at 0.1, 1.6, 3.8, 5, 6.2, 8 and 9 m depth) and CCR (collected at 0.1, 1.5, 6.0, 9.0, 15.0 and 20.0 m depth), in addition to CCR inflows (collected at 0.1 m depth). We additionally collected and analyzed metals samples from the inflows and FCR and CCR (collected at 0.1 m depth). Our field data also includes x-ray diffraction (XRD) spectra obtained from surficial sediments collected at CCR. See section 2.2 for a full description of sampling methods.

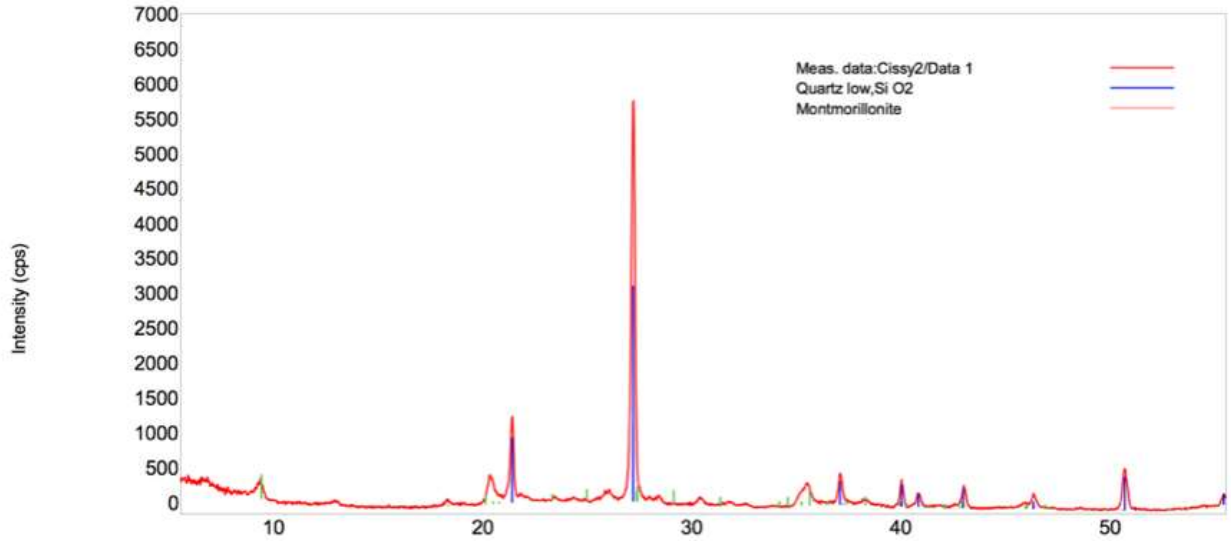

Figure S1: X-ray diffraction peaks detected in Carvins Cove Reservoir sediments collected from site 50, with matches for montmorillonite and quartz overlaid. Combined, quartz and montmorillonite comprise over 90% of minerals detected in the sediments.

Table S1: Anion concentration data for Falling Creek Reservoir (FCR), Carvins Cove Reservoir (CCR) and CCR inflows collected in 2022. For nearly all samples, NO_3-N concentrations were below the detection limit of 0.1 mg/L.

Reservoir	Date	Depth (m)	Site	Cl^- (mg/L)	NO_3-N (mg/L)	SO_4^{-2}
FCR	6/7/2022	0.1	50	0.85	<0.1	0.77
FCR	6/7/2022	1.6	50	0.89	<0.1	0.83
FCR	6/7/2022	3.8	50	0.86	<0.1	0.93
FCR	6/7/2022	5	50	0.92	<0.1	0.94
FCR	6/7/2022	6.2	50	0.96	<0.1	0.91
FCR	6/7/2022	8	50	1.1	<0.1	0.89
FCR	6/7/2022	9	50	0.96	<0.1	0.89
CCR	6/9/2022	0.1	50	1.41	<0.1	4.53
CCR	6/9/2022	3	50	1.04	<0.1	3.85
CCR	6/9/2022	5	50	1.71	<0.1	5.38
CCR	6/9/2022	9	50	1.82	<0.1	5.38
CCR	6/9/2022	12	50	1.81	<0.1	5.18
CCR	6/9/2022	15	50	2	<0.1	5.76
CCR	6/9/2022	18	50	1.35	<0.1	4.05
CCR	6/30/2022	0.1	50	1.78	<0.1	5.59
CCR	6/30/2022	1.5	50	2.07	<0.1	5.54
CCR	6/30/2022	6	50	1.91	<0.1	5.52
CCR	6/30/2022	9	50	2.04	<0.1	5.73
CCR	6/30/2022	15	50	2.01	<0.1	5.74
CCR	6/30/2022	21	50	2.03	<0.1	5.47
FCR	6/20/2022	0.1	50	1.11	<0.1	0.57
FCR	6/20/2022	1.6	50	0.96	<0.1	0.57
FCR	6/20/2022	3.8	50	0.99	<0.1	0.83
FCR	6/20/2022	5	50	0.98	<0.1	0.77
FCR	6/20/2022	6.2	50	1.01	<0.1	0.81
FCR	6/20/2022	8	50	0.95	<0.1	0.8
FCR	6/20/2022	9	50	1.02	<0.1	0.7
CCR	6/30/2022	0.1	501	1.97	<0.1	22.77

CCR	6/30/2022	0.1	201	4.5	<0.1	6.42
CCR	7/14/2022	0.1	101	0.67	<0.1	2.16
CCR	7/14/2022	0.1	301	0.59	<0.1	2.24
CCR	7/14/2022	0.1	50	1.71	<0.1	5.52
CCR	7/14/2022	1.5	50	1.73	<0.1	5.49
CCR	7/14/2022	6	50	1.79	<0.1	5.54
CCR	7/14/2022	9	50	1.9	<0.1	5.65
CCR	7/14/2022	15	50	1.98	<0.1	5.65
CCR	7/14/2022	20	50	2.02	<0.1	5.49
FCR	7/11/2022	0.1	50	1.19	<0.1	0.39
FCR	7/11/2022	1.6	50	1	<0.1	0.4
FCR	7/11/2022	3.8	50	1.18	<0.1	0.53
FCR	7/11/2022	5	50	1.21	<0.1	0.42
FCR	7/11/2022	6.2	50	1.15	<0.1	0.63
FCR	7/11/2022	8	50	1.01	<0.1	0.64
FCR	7/11/2022	9	50	1.23	<0.1	0.65
FCR	7/5/2022	0.1	50	1.42	<0.1	0.36
FCR	7/5/2022	8	50	0.99	<0.1	0.65
FCR	7/5/2022	6.2	50	1.05	<0.1	0.63
FCR	7/5/2022	9	50	1.02	<0.1	0.67
FCR	7/5/2022	3.8	50	1.16	<0.1	0.56
FCR	7/5/2022	5	50	1.07	<0.1	0.57
FCR	7/5/2022	1.6	50	0.98	<0.1	0.54
FCR	7/25/2022	9	50	0.53	0.49	0.48
FCR	7/25/2022	1.6	50	1.03	<0.1	0.43
FCR	7/25/2022	8	50	1.09	<0.1	0.56
FCR	7/25/2022	3.8	50	1.39	<0.1	0.44
FCR	7/25/2022	6.2	50	1.19	<0.1	0.52
FCR	7/25/2022	5	50	1.22	<0.1	0.5
FCR	7/25/2022	0.1	50	1.15	<0.1	0.43
CCR	7/28/2022	9	50	0.97	<0.1	3.12
CCR	7/28/2022	0.1	50	1.71	<0.1	5.36
CCR	7/28/2022	6	50	0.53	<0.1	1.85
CCR	7/28/2022	1.5	50	1.69	<0.1	5.38
CCR	7/28/2022	15	50	2.01	<0.1	5.59

CCR	7/28/2022	20	50	2.01	<0.1	5.15
FCR	8/8/2022	9	50	1.01	<0.1	0.47
FCR	8/8/2022	6.2	50	1.07	<0.1	0.46
FCR	8/8/2022	5	50	1.14	<0.1	0.38
FCR	8/8/2022	1.6	50	0.94	<0.1	0.41
FCR	8/8/2022	8	50	1.02	<0.1	0.47
FCR	8/8/2022	3.8	50	1.33	<0.1	0.45
FCR	8/8/2022	0.1	50	0.88	<0.1	0.39
FCR	8/18/2022	3.8	50	1.53	<0.1	0.51
FCR	8/18/2022	0.1	50	1.22	<0.1	0.48
CCR	8/19/2022	0.1	201	3.27	<0.1	6.56
CCR	8/19/2022	20	50	2.17	<0.1	4.55
FCR	8/18/2022	6.2	50	1.22	<0.1	0.42
CCR	8/19/2022	6	50	1.75	<0.1	5.31
CCR	8/19/2022	0.1	301	0.65	<0.1	2.92
CCR	9/29/2022	6	50	1.88	<0.1	5.18
CCR	9/29/2022	1.5	50	1.97	<0.1	5.56
CCR	9/29/2022	15	50	2.12	<0.1	5.18
CCR	9/29/2022	9	50	2.02	<0.1	5.13
CCR	9/29/2022	21	50	2.11	<0.1	5.25
CCR	9/29/2022	0.1	50	1.85	<0.1	5.22
FCR	8/18/2022	5	50	1.24	<0.1	0.3
CCR	8/19/2022	0.1	50	1.75	<0.1	5.14
FCR	8/18/2022	9	50	1.16	<0.1	0.47
CCR	8/19/2022	15	50	2.12	<0.1	5.33
CCR	8/19/2022	9	50	2.09	<0.1	5.32
FCR	8/18/2022	8	50	1.17	<0.1	0.44
CCR	8/19/2022	1.5	50	1.77	<0.1	5.19
FCR	8/18/2022	1.6	50	1.02	<0.1	0.47
FCR	9/26/2022	5	50	1.16	<0.1	0.44
FCR	9/26/2022	1.6	50	1.04	<0.1	0.53
FCR	9/26/2022	3.8	50	1.18	<0.1	0.5
FCR	9/26/2022	6.2	50	1.17	<0.1	0.34
FCR	9/26/2022	0.1	50	1.07	<0.1	0.53

FCR	9/26/2022	8	50	1.18	<0.1	0.31
FCR	9/26/2022	9	50	1.17	<0.1	0.32

Table S2: Fe and Mn concentrations at the inflows of Falling Creek Reservoir (FCR) and Carvins Cove Reservoir (CCR) in 2022.

Reservoir	Site	Date and Time	Total iron (mg/L)	Total manganese (mg/L)	Soluble iron (mg/L)	Soluble manganese (mg/L)
FCR	100	2022-05-02 16:22:00	NA	NA	0.0076	0.0025
FCR	200	2022-05-02 16:55:00	NA	NA	0.8688	0.0531
FCR	100	2022-05-09 09:45:00	NA	NA	0.0057	0.001
FCR	200	2022-05-09 10:45:00	NA	NA	0.8809	0.0653
FCR	100	2022-05-17 16:34:00	NA	NA	0.0137	0.0008
FCR	200	2022-05-17 17:02:00	NA	NA	1.0298	0.0507
FCR	100	2022-05-23 12:45:00	NA	NA	0.0512	0.0048
FCR	200	2022-05-23 13:36:00	NA	NA	1.538	0.0928
FCR	100	2022-05-31 12:05:00	NA	NA	0.1621	0.009
FCR	200	2022-05-31 12:33:00	NA	NA	0.5637	0.044
FCR	100	2022-06-07 15:27:00	NA	NA	0.1343	0.0034
FCR	100	2022-06-13 12:00:00	NA	NA	0.1325	0.0048
FCR	200	2022-06-13	NA	NA	1.1223	0.0523

		13:02:00				
FCR	100	2022-06-20 10:04:00	NA	NA	0.2021	0.0046
FCR	200	2022-06-20 11:15:00	NA	NA	1.0665	0.0621
FCR	100	2022-06-27 13:06:00	NA	NA	0.2075	0.0075
FCR	200	2022-06-27 12:40:00	NA	NA	0.7814	0.0659
CCR	301	2022-06-30 13:10:00	0.1445	0.0625	0.0104	0.0176
CCR	501	2022-06-30 14:05:00	0.2199	0.0263	0.0139	0.0037
CCR	400	2022-06-30 12:00:00	0.5203	0.064	0.1417	0.0631
CCR	201	2022-06-30 12:00:00	0.2076	0.0433	0.0104	0.0393
FCR	100	2022-07-05 10:11:00	0.1816	0.1139	0.0886	0.1056
CCR	301	2022-07-14 13:30:00	0.056	0.0152	0.022	0.0073
CCR	201	2022-07-14 14:10:00	0.1655	0.0234	0.018	0.0117
FCR	100	2022-07-18 10:00:00	0.1246	0.0662	0.075	0.0698
FCR	200	2022-07-18 10:00:00	NA	NA	1.4179	0.0853
CCR	301	2022-07-28 12:00:00	0.0573	0.0144	0.1789	0.0316
FCR	100	2022-08-01 09:54:00	NA	NA	0.1192	0.0648
FCR	100	2022-08-18 12:35:00	NA	NA	0.0647	0.0394
FCR	200	2022-08-18	NA	NA	1.4059	0.0892

		13:15:00				
CCR	301	2022-08-19 12:39:00	0.0685	0.0201	0.0225	0.0087
CCR	201	2022-08-19 13:32:00	0.2204	0.0314	0.0801	0.0285
FCR	100	2022-09-13 13:10:00	NA	NA	0.0423	0.0134
FCR	100	2022-09-26 13:34:00	NA	NA	0.042	0.0179
FCR	200	2022-09-26 14:30:00	NA	NA	0.6326	0.0582
CCR	301	2022-09-29 10:34:00	0.073	0.0225	0.0206	0.0088
CCR	201	2022-09-29 09:45:00	0.0775	0.0189	0.0488	0.0187
FCR	100	2022-10-03 14:00:00	0.1259	0.0165	0.0331	0.0049
CCR	301	2022-10-14 11:25:00	0.0461	0.0117	0.0261	0.006
CCR	201	2022-10-14 10:20:00	0.1408	0.0237	0.0533	0.0233
FCR	100	2022-10-17 12:00:00	0.1363	0.0314	0.0485	0.0226
FCR	200	2022-10-17 12:00:00	NA	NA	1.1278	0.1086
FCR	100	2022-11-16 12:00:00	0.0685	0.0106	0.0345	0.0065
FCR	100	2022-11-16 00:00:00	0.0974	0.0107	0.0493	0.0046
CCR	301	2022-11-17 11:00:00	0.057	0.0129	0.0652	0.0101
CCR	501	2022-11-17 10:30:00	0.1415	0.0126	0.0334	0.005
CCR	400	2022-11-17	0.2642	0.0299	0.0422	0.0181

		11:30:00				
CCR	201	2022-11-17 09:30:00	0.1028	0.0105	0.0577	0.0086
FCR	100	2022-11-28 13:40:00	0.1028	0.0189	0.0354	0.0063
FCR	200	2022-11-28 13:55:00	NA	NA	0.5414	0.0437

Appendix B. Benchtop scanning electron microscopy (SEM) images and element maps of macroscopic particles from 14-day pH-alkalinity experiments

For the 14-day pH-alkalinity experiments, we collected backscatter electron (BSE) images and energy dispersive X-ray spectroscopy (EDS) element maps of macroscopic particles from the high pH/moderate alkalinity and high pH/high alkalinity experiments. Images were collected using a Hitachi TM3000 benchtop SEM housed in the Department of Geosciences at Virginia Tech. EDS element mapping was conducted using a Quantax 70 EDS system attached to the benchtop SEM. Particles were collected from the experimental solutions for analysis on day 14 of the experiment, before washing with nanopure water as described in Section 2.6.1 and mounting on copper electrical tape without coating.

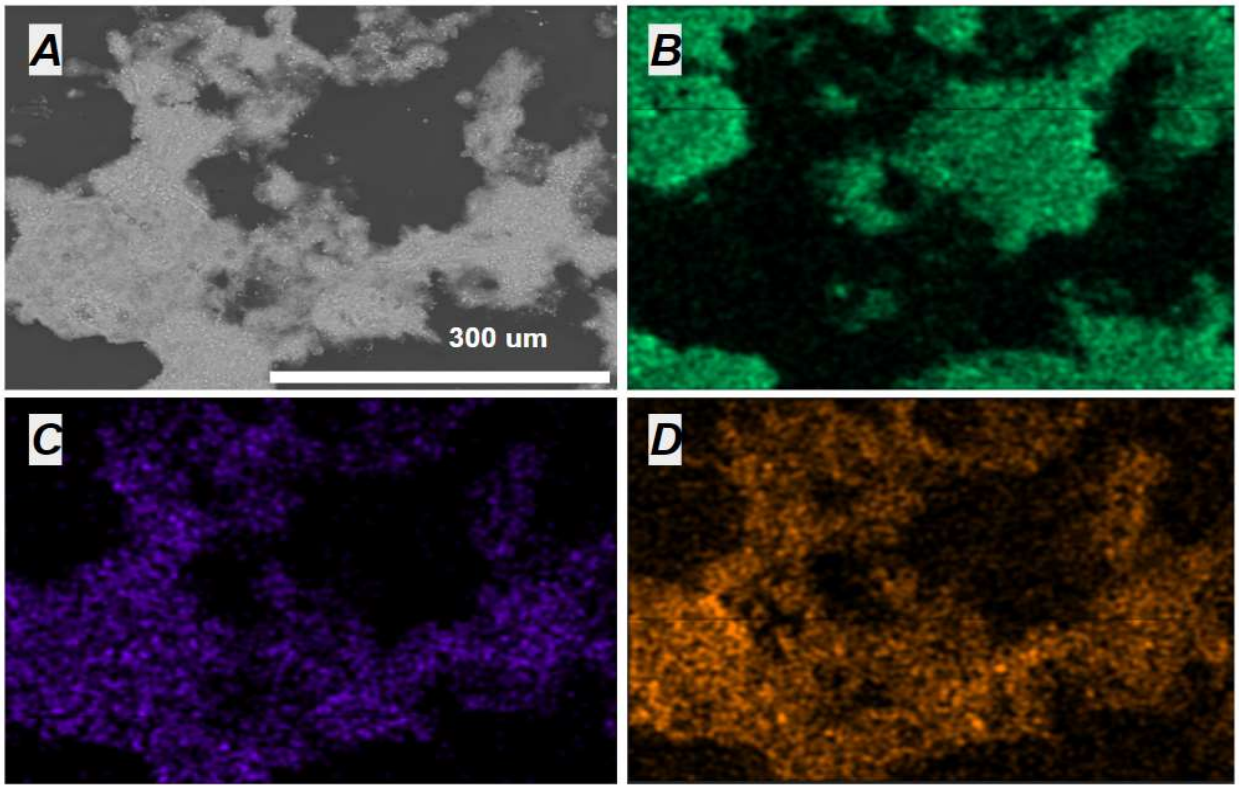

Figure S2. 14-day high pH/high alkalinity experiment. A) Backscattered electron (BSE) image of a macroscopic particle collected from the experiment. B) Energy dispersive X-ray spectroscopy (EDS) map of carbon abundances across the surface of the particle shown in A. Carbon is almost entirely absent from the surface of the particle, with regions of abundant carbon likely introduced by adhesive on the copper tape used to mount samples. C) EDS map of manganese abundances across the surface of the particle shown in A. D) EDS map of oxygen abundances across the surface of the particle shown in A.

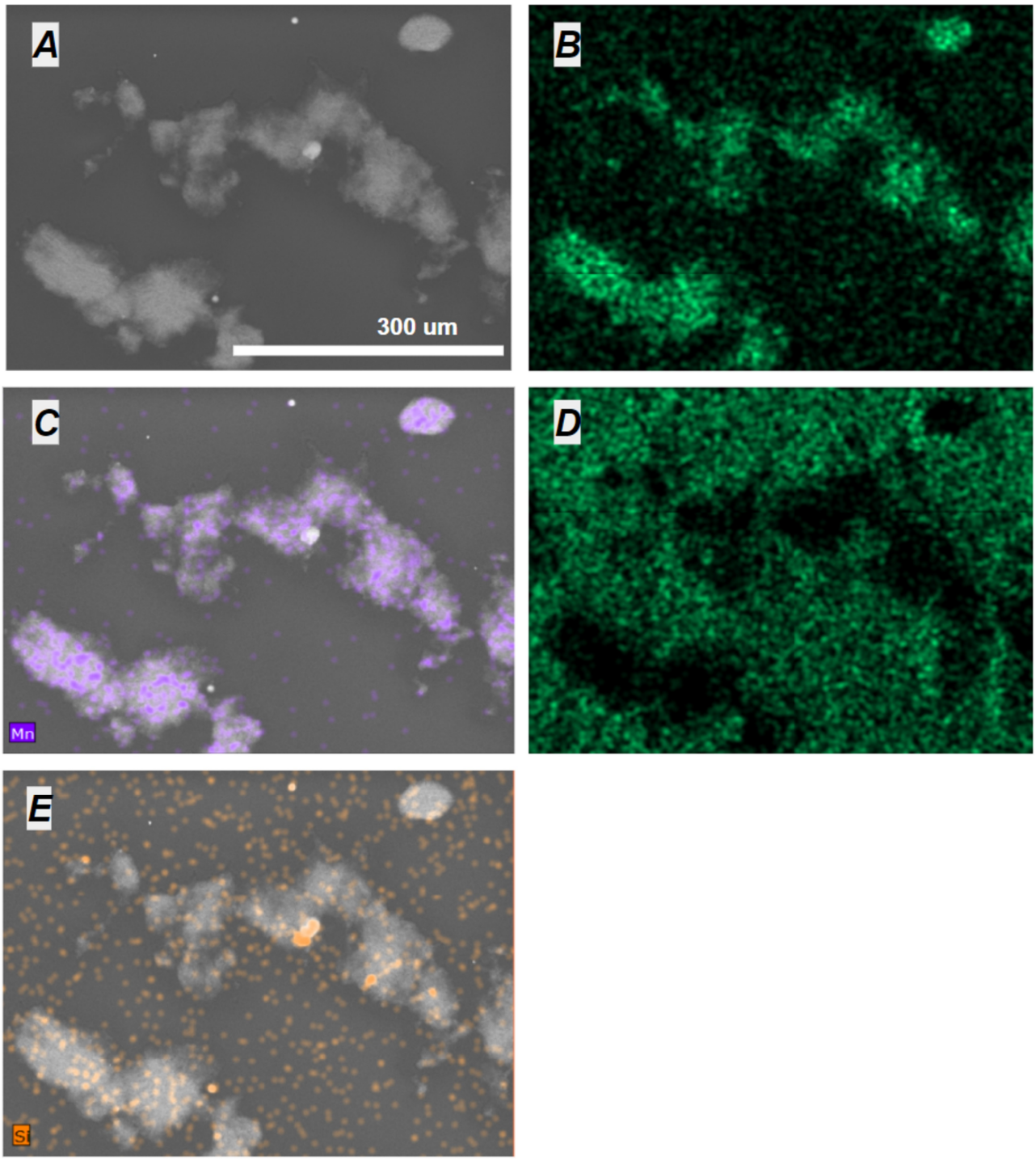

Figure S3. 14-day high pH/moderate alkalinity experiment. A) Backscattered electron image of a macroscopic particle collected from the experiment. B) Energy dispersive X-ray spectroscopy (EDS) map of carbon abundances across the surface of the particle shown in A. Carbon is almost

entirely absent from the surface of the particle, with regions of abundant carbon likely introduced by adhesive on the copper tape used to mount samples. C) EDS map of Mn abundances across the surface of the particle shown in A. D) Elemental map of relative oxygen abundances across the surface of the particle shown in A. E) Elemental map of relative silicon abundances across the surface of the particle shown in A. Areas of high silicon abundance likely correspond to glass contamination within the experimental solutions.

Appendix C. Additional TEM images and element maps of particles from 24-hour pH and alkalinity laboratory experiments

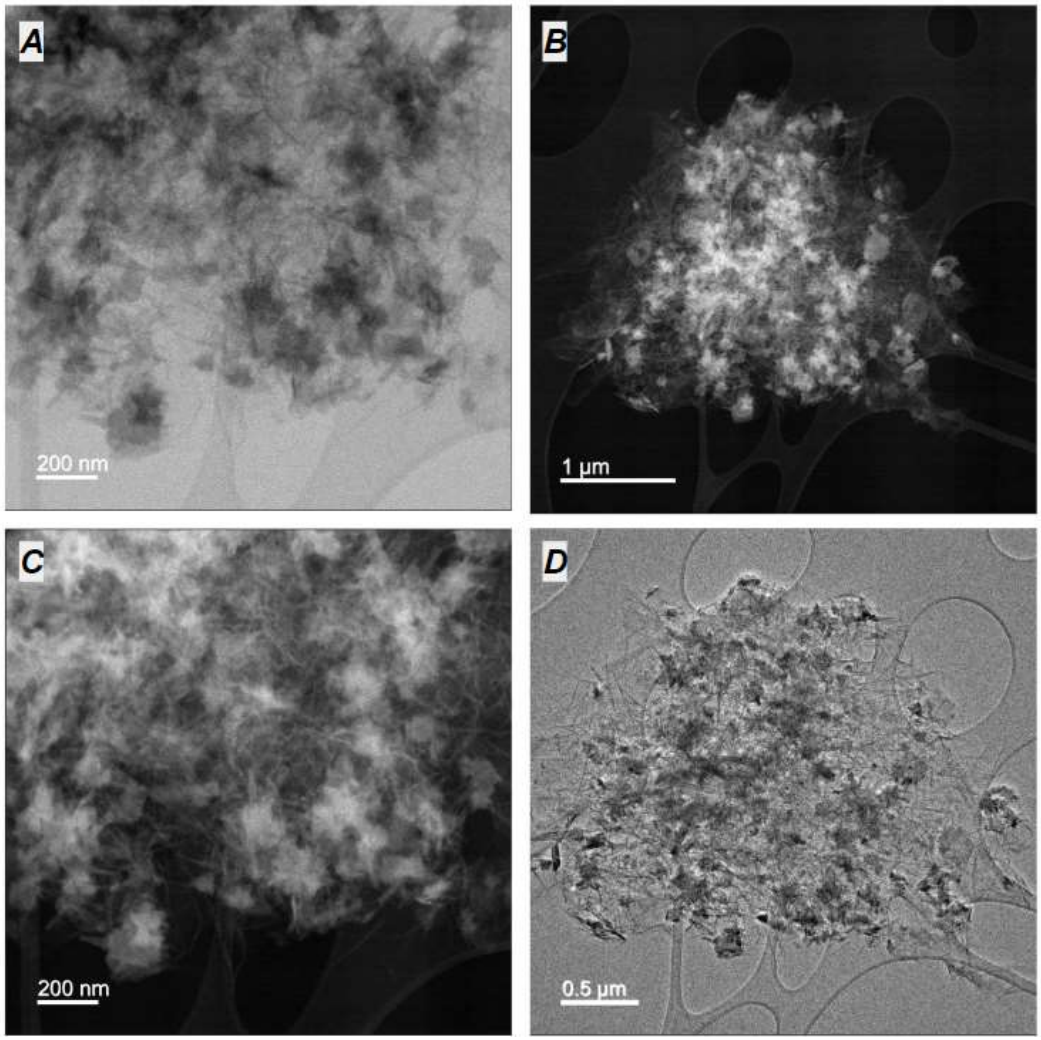

Figure S4. Transmission electron microscopy (TEM) images of a microscopic particle suspended in the 24-hour high pH/moderate alkalinity solution at 12 hours. The particle is several um in diameter and contains interlocking needle-like crystals of under 10 nm in diameter each. A) High magnification brightfield TEM image. B) Brightfield TEM image of the entire particle. C) Darkfield TEM image of the same view shown in A. D) Darkfield TEM image of the same view shown in B.

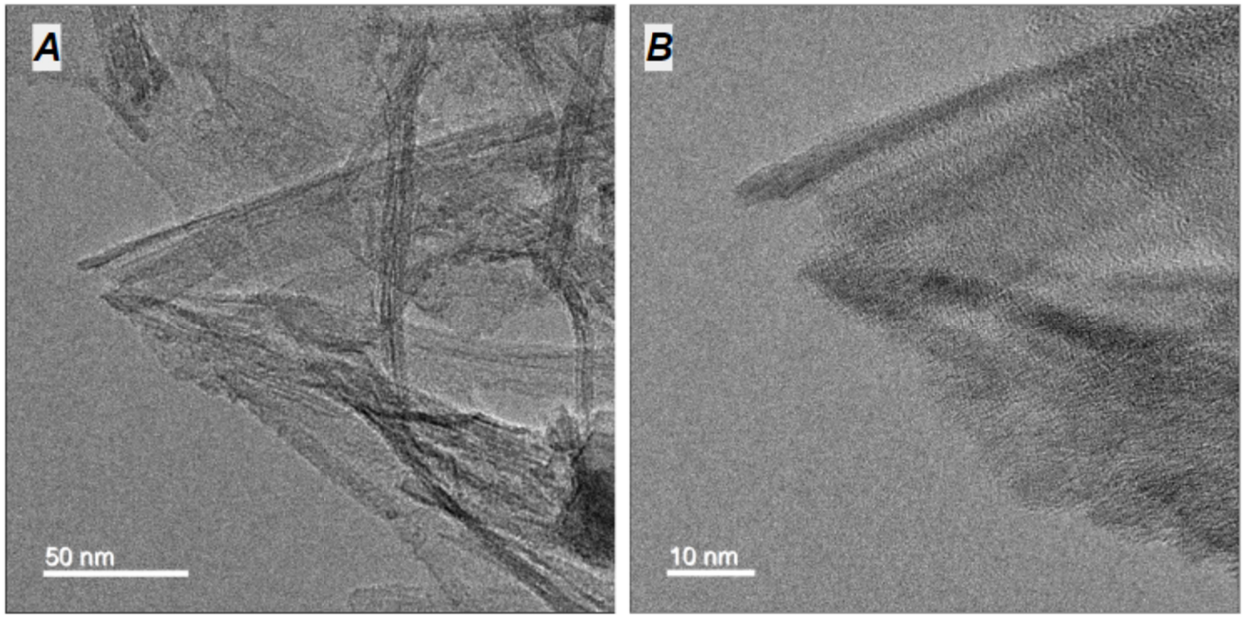

Figure S5. High magnification brightfield TEM images collected of the particle shown in Figure S4. A) Brightfield TEM image along the particle's periphery. B) Higher magnification brightfield TEM image in the same region shown in A. No crystal lattice fringes are visible.

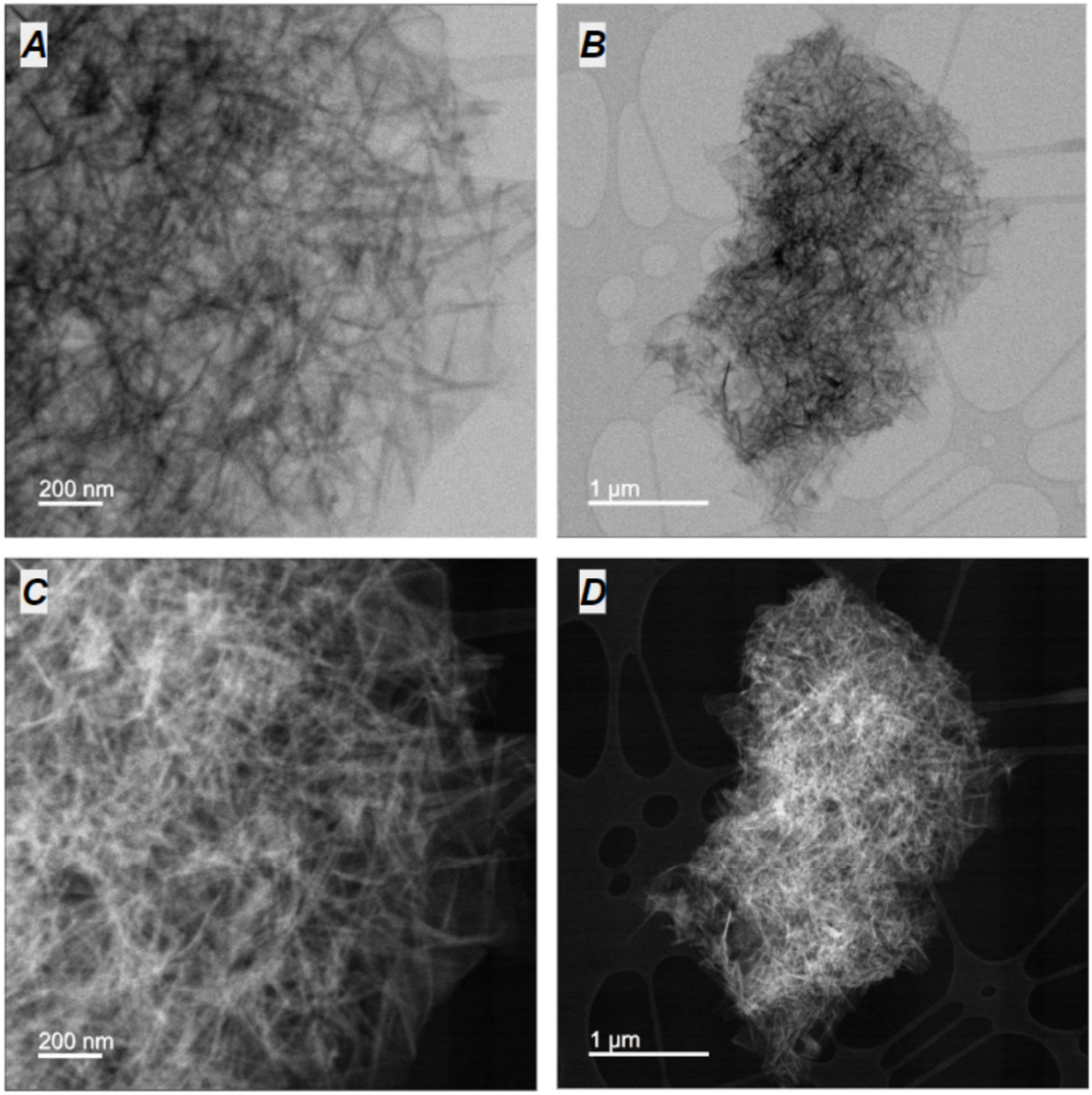

Figure S6. Transmission electron microscopy (TEM) images of a microscopic particle suspended in the 24-hour high pH/high alkalinity solution at 12 hours. The particle is several um in diameter and contains interlocking needle-like crystals of under 10 nm in diameter each. A) High magnification brightfield TEM image of the particle. Sheet-like morphologies are visible alongside the needles. B) Brightfield TEM image of the entire particle. C) Darkfield TEM image of the same view shown in A. D) Darkfield TEM image of the same view shown in B.

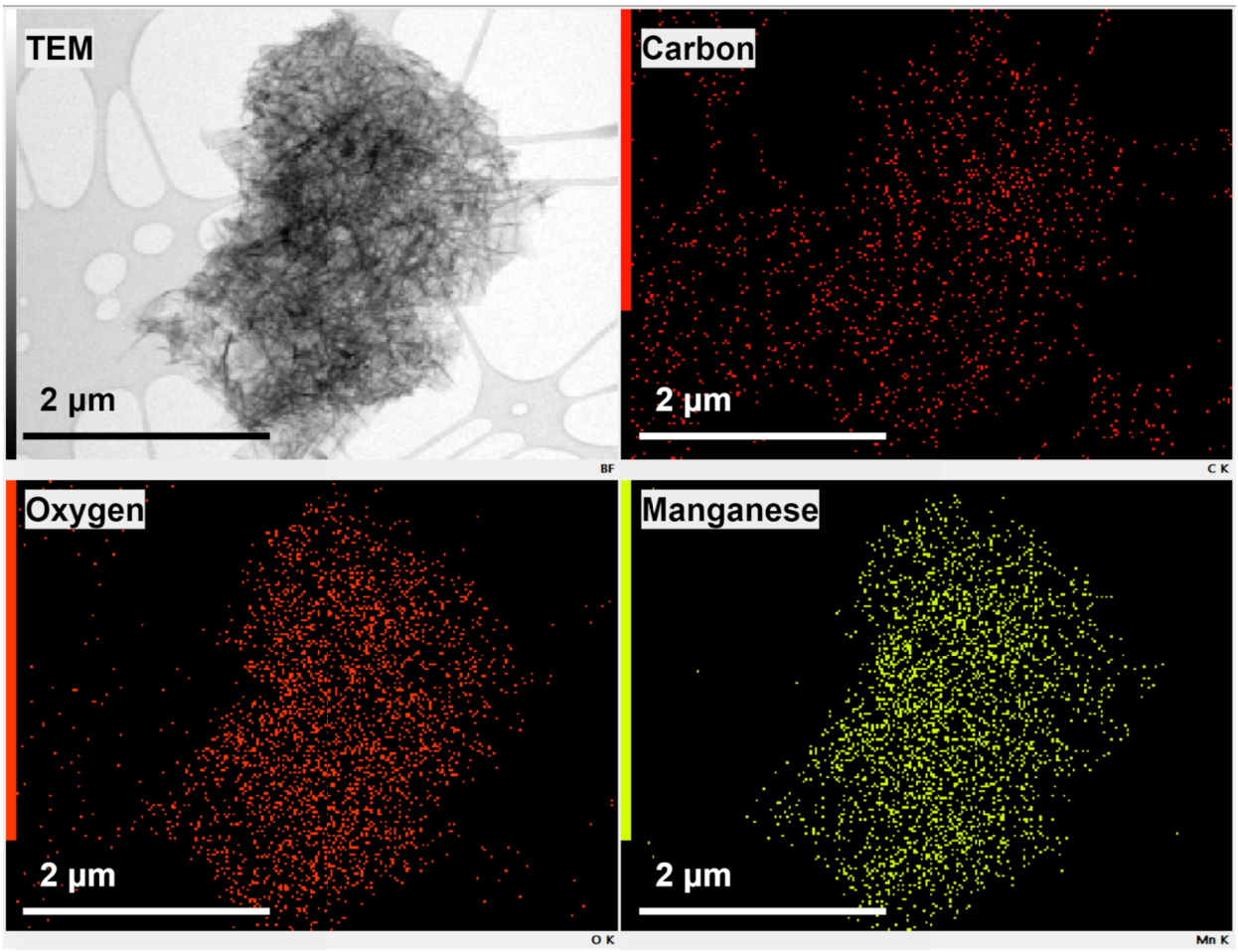

Figure S7. Carbon, oxygen and manganese element maps of particle collected from high pH/high alkalinity solution. Maps and brightfield image collected by transmission electron microscopy.

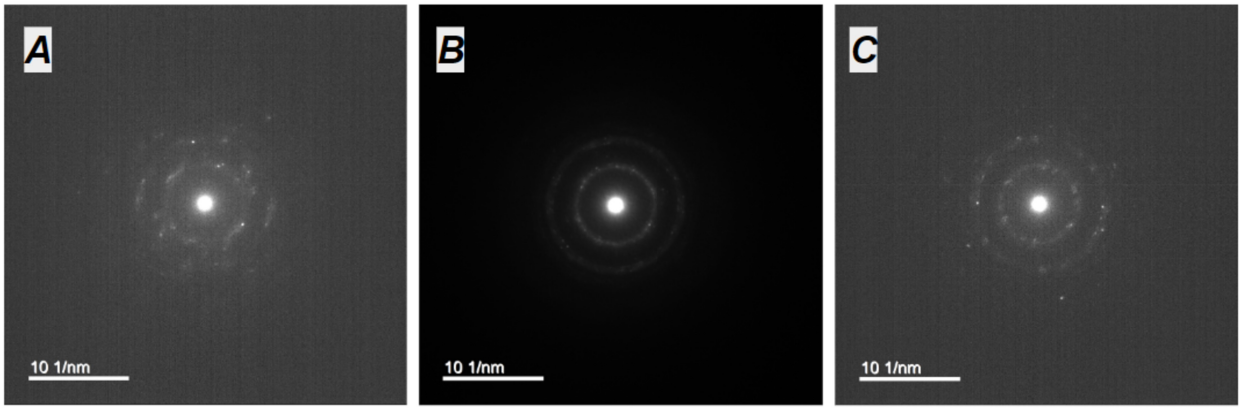

Figure S8. Selected area electron diffraction spot and ring patterns from the high pH/moderate alkalinity solution particle shown in Figure 8 and Figure S4.

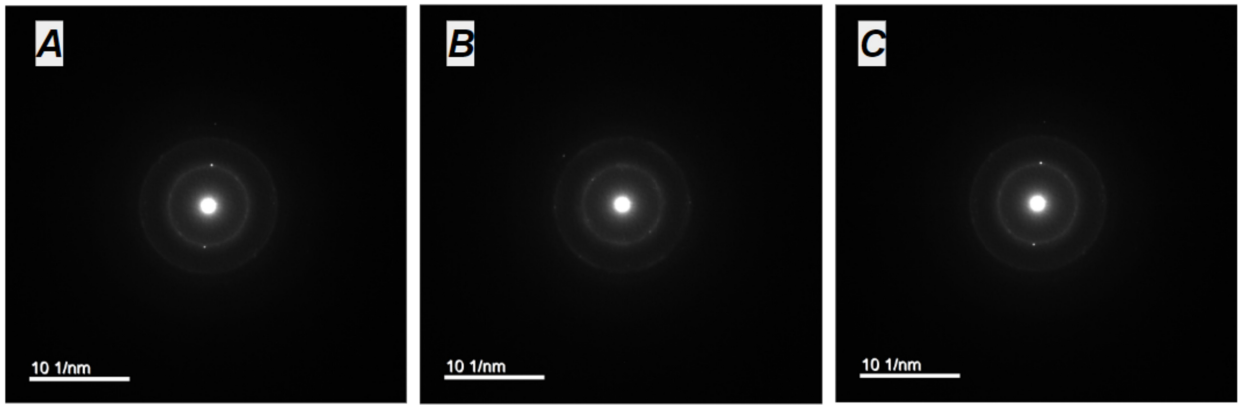

Figure S9. Selected area electron diffraction spot and ring patterns from the high pH/high alkalinity solution particle shown in Figure S7.

Table S3: d-spacings obtained from the SAED pattern shown in Figure S8 A

Feature	Notes	d-Spacing (Å)
Spot	Bright	2.49062
Spot	Radius overlaps 2 bright spots	2.21078
Spot	Radius overlaps 2 faint spots	1.80513
Ring	Dispersed	2.37059
Spot	Faint	1.92901
Spot	Bright	1.626
Spot	Radius overlaps 4 faint spots	1.4906
Ring	Overlaps 3 faint spots	1.22211
Spot	Faint	0.919

Table S4: d-spacings obtained from the selected area electron diffraction pattern shown in Figure S8 B

Feature	Notes	d-Spacing (Å)
Spot	Faint	2.8396
Ring	Radius overlaps 2 bright spots and 4 faint spots	2.57457
Spot	Faint	2.21946
Ring	Radius overlaps 3 bright spots	1.56986
Spot	Faint	1.40944
Spot	Bright	1.45183
Spot	Bright	1.20683
Spot	Faint	1.12936
Spot	Bright	1.01628

Table S5: d-spacings obtained from selected area electron diffraction pattern shown in Figure S8 C

Feature	Notes	d-Spacing (Å)
Ring	Overlaps 5 bright spots and numerous faint spots	2.35479
Spot	Bright	2.5407
Spot	Faint	1.91181
Ring	Overlaps 2 bright spots	1.56986
Ring	Overlaps 3 bright spots	1.43032

Table S6: d-spacings obtained from selected area electron diffraction pattern shown in Figure S9 A

Feature	Notes	d-Spacing (Å)
Ring	Dispersed	2.49062
Spot	Bright	2.37059
Spot	Radius overlaps 2 bright spots and one faint spot	2.21078
Spot	Radius overlaps 2 faint spots	1.78872
Spot	Radius overlaps 2 bright spots	1.45748

Table S7: d-spacings obtained from selected area electron diffraction pattern shown in Figure S9 B

Feature	Notes	d-Spacing (Å)
Ring	Overlaps 2 bright spots	2.49062
Ring	Overlaps 4 faint spots	1.4362
Spot	Bright	1.27766

Table S8: d-spacings obtained from selected area electron diffraction pattern shown in Figure S11 C

Feature	Notes	d-Spacing (Å)
Ring	Overlaps 2 bright spots	2.38286
Ring	Faint/dispersed	1.46282
Spot	Faint	1.19933

Appendix D. Additional scanning electron microscopy (SEM) images, selected area electron diffraction (SAED) data and electron probe microanalyzer (EPMA) element maps of particles from 24-hour pH-alkalinity laboratory experiments

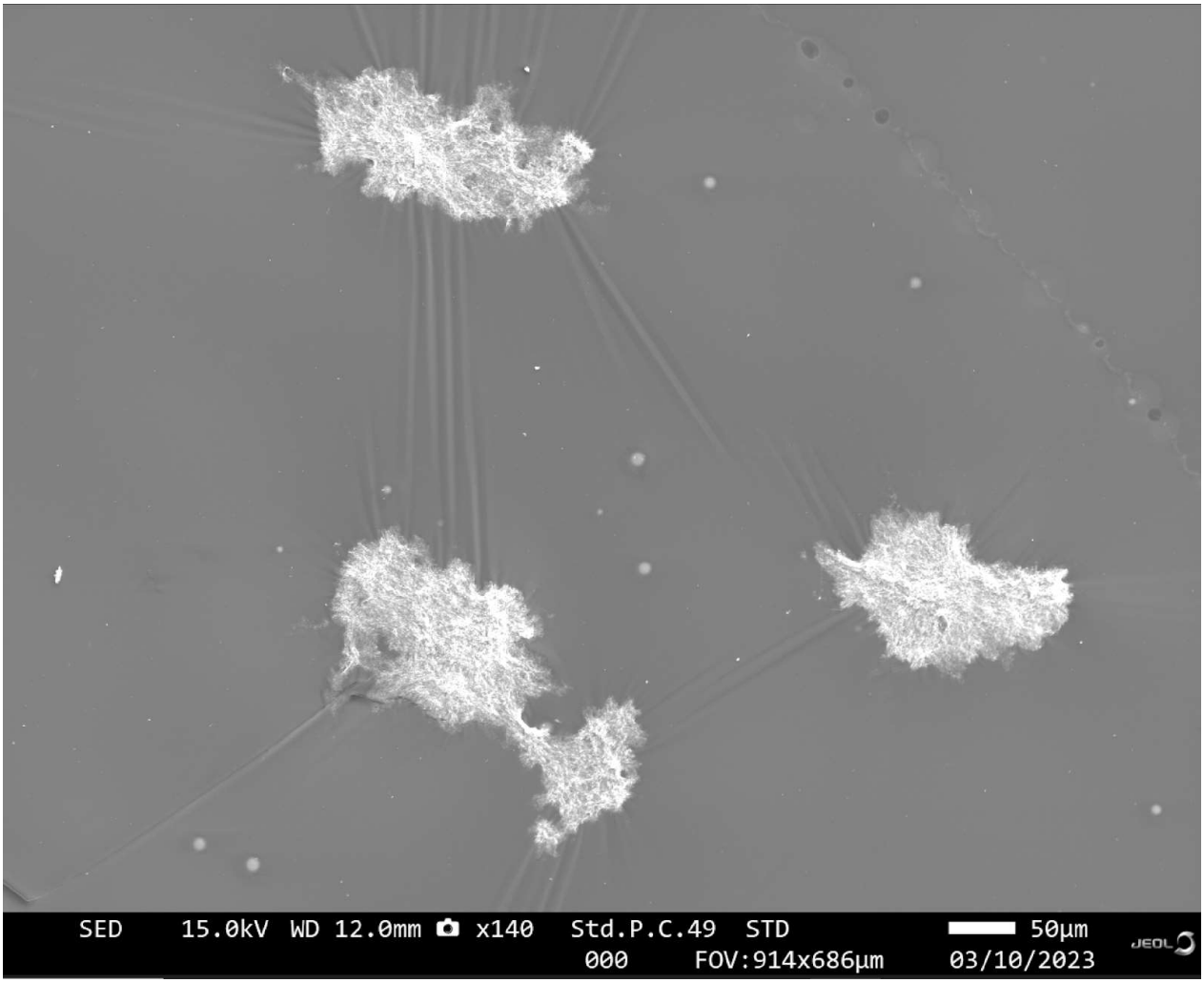

Figure S10. Scanning electron microscopy image of several particles collected from high pH/high alkalinity solutions at 24 hours.

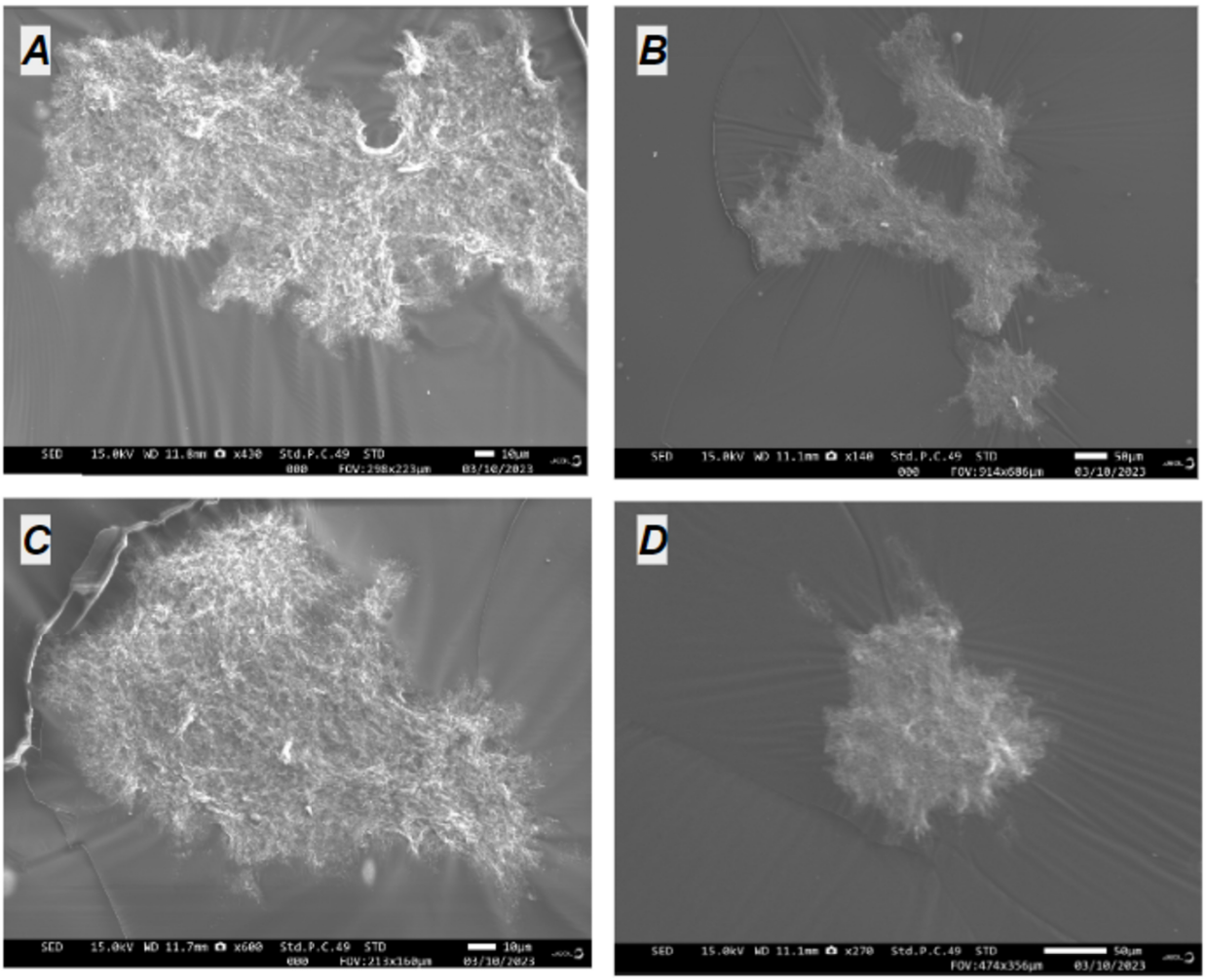

Figure S11. Scanning electron microscopy images of particles collected from high pH/moderate alkalinity solution at 24 hours. Particles feature pitted surface textures similar to particles collected from the high pH/high alkalinity solution.

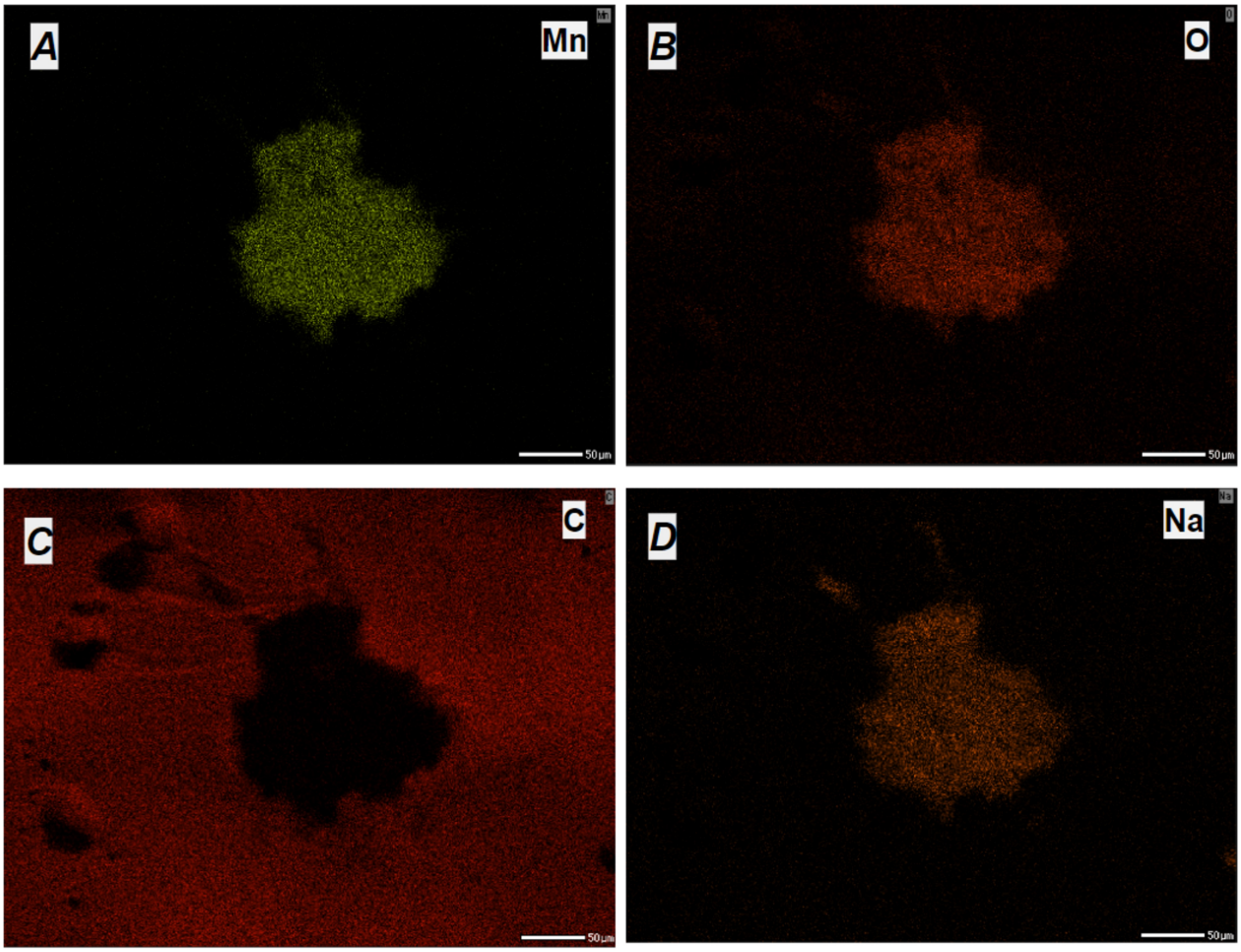

Figure S12. Electron probe microanalyzer element maps collected for the particle shown in Figure S11 D.

Appendix E. Additional SEM images from preliminary pH and alkalinity laboratory experiments

In addition to the 14-day and 24-hour pH and alkalinity laboratory experiments, we conducted preliminary experiments on Mn removal in solutions of varying pH and alkalinity. The conditions tested were pH 10 without alkalinity adjustment, pH 10 and 80 mg/L $CaCO_3$, pH 10 and 800 mg/L $CaCO_3$, and pH 10 and 40 mg/L $CaCO_3$. We adjusted the pH and alkalinity within these experiments using dilute NaOH and Na_2CO_3, respectively. For the duration of the experiment, solutions remained exposed to light and oxygenated by continuous agitation. Using the leucoberbelin blue method, monitoring of oxidized Mn concentrations in solutions occurred weekly for a total of 30 days. We observed formation of black particles in pH 10 and 80 mg/L $CaCO_3$ and pH 10 and 800 mg/L $CaCO_3$ solutions within one week. Yellow-brown discoloration was observed in the pH 10 and 40 mg/L $CaCO_3$ solution. The particles remained until the experiment's conclusion. After triple rinsing with nanopure water, macroscopic (>100 μm) particles collected on day 30 were mounted on carbon tape and sputter coated with carbon. Particles were imaged using the JEOL IT500 SEM housed in the Virginia Tech NCFL.

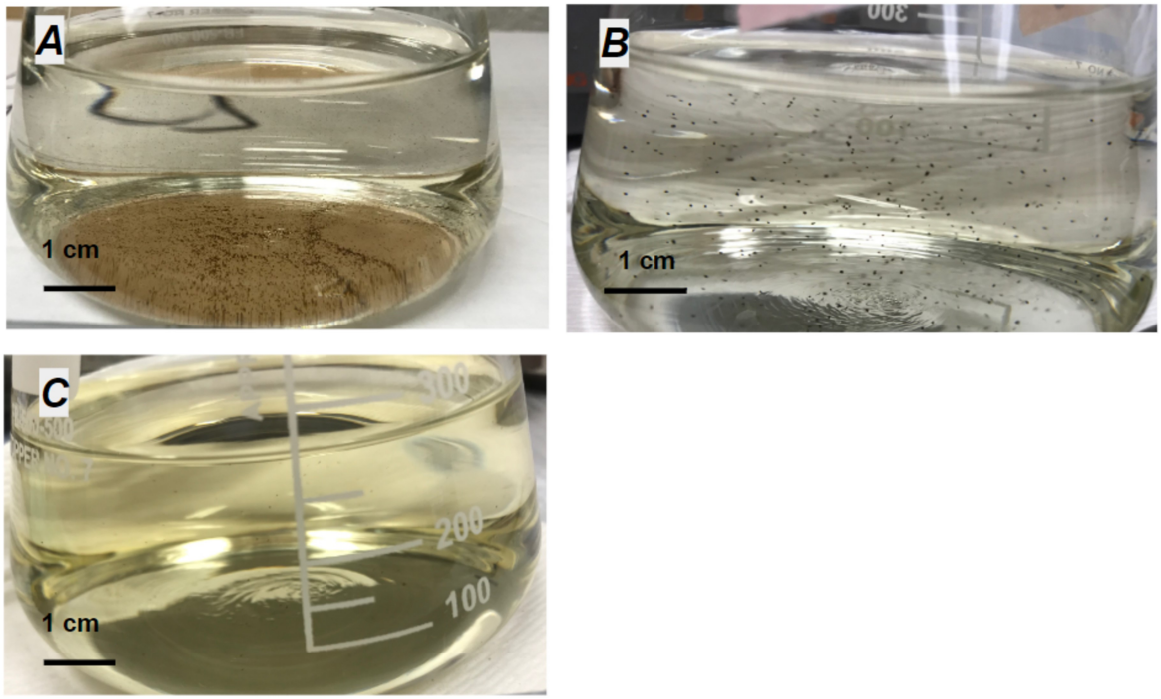

Figure S13. Images of the preliminary pH and alkalinity experiments photographed on day 7. A) pH 10 and 800 mg/L $CaCO_3$. B) pH 10 and 80 mg/L $CaCO_3$. C) pH 10 and 40 mg/L $CaCO_3$.

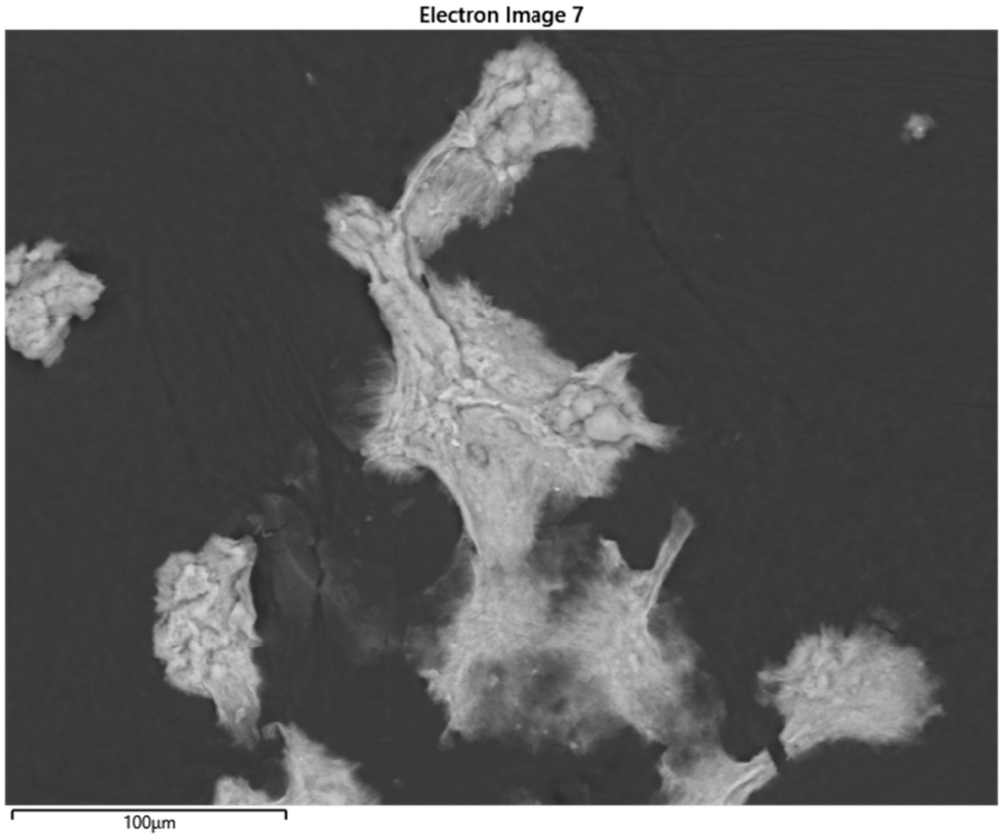

Figure S14. Scanning electron microscopy image of a single particle collected from the pH 10 and 800 mg/L $CaCO_3$ solution on day 30.

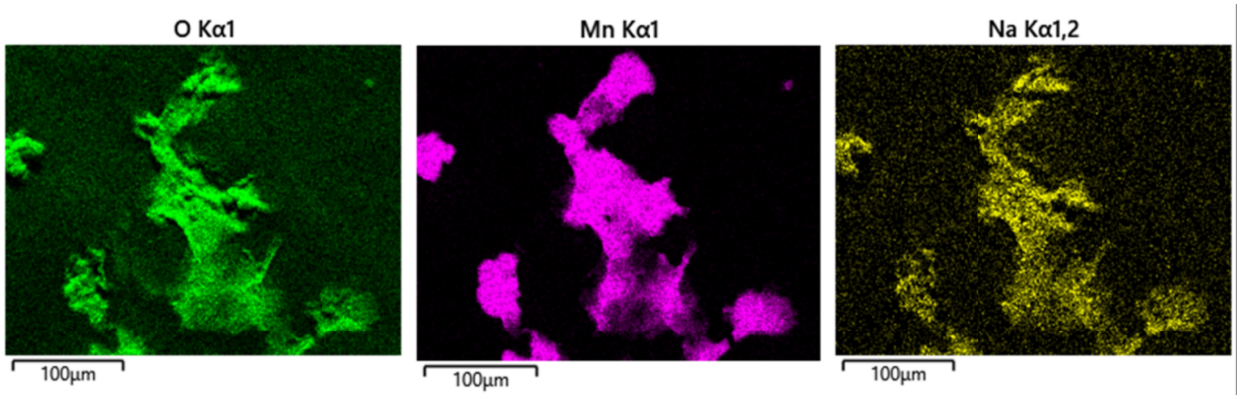

Figure S15. Energy dispersive spectroscopy of the particle shown in Figure S14.

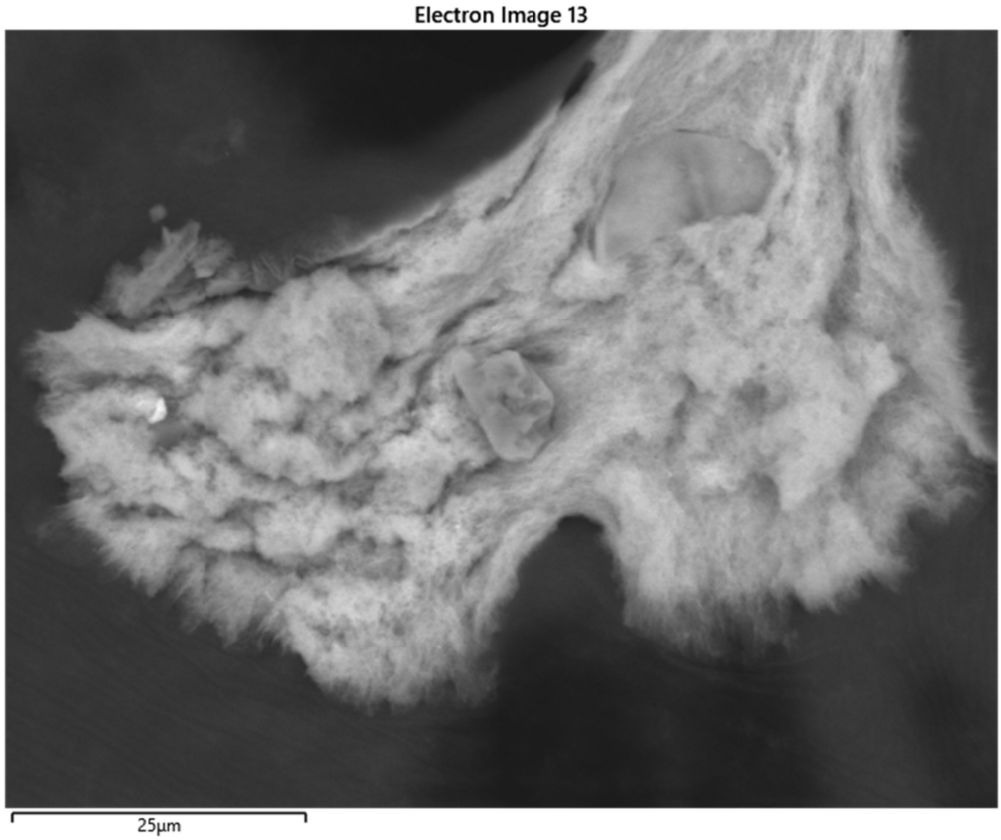

Figure S16. High magnification scanning electron microscopy image of a single particle collected from the pH 10 and 800 mg/L $CaCO_3$ solution on day 30.

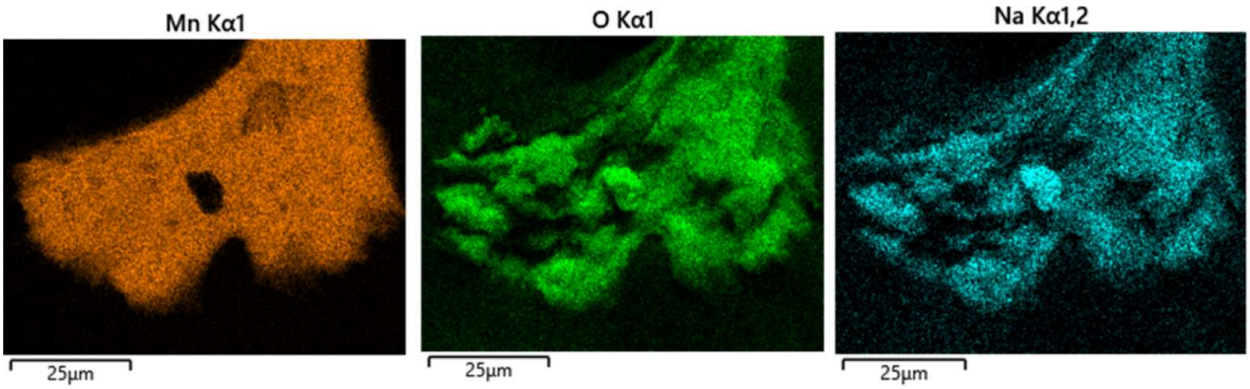

Figure S17. Energy dispersive X-ray spectroscopy of the view shown in Figure S16.

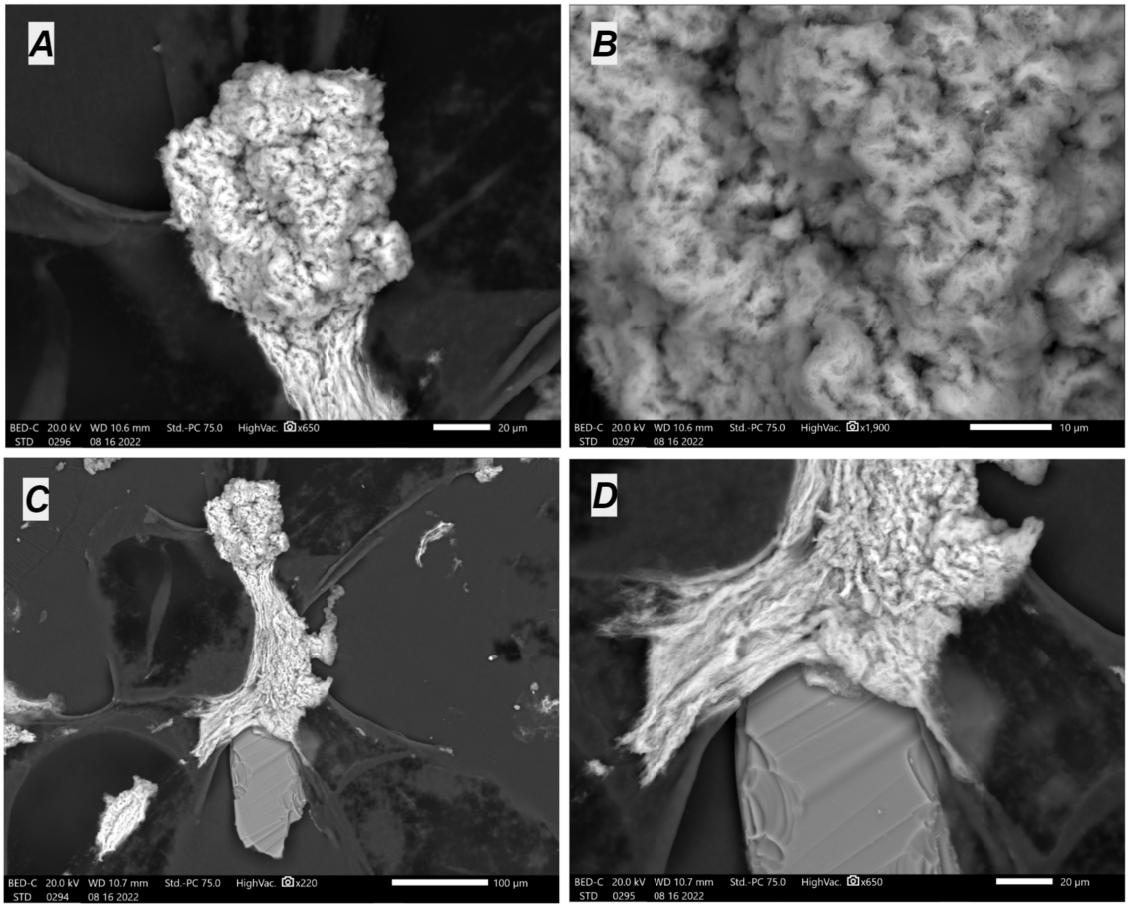

Figure S18. Scanning electron microscopy images of a single MnOx particle collected from pH 10 and 80 mg/L $CaCO_3$ solution. A) Image collected at 650x magnification. B) Image collected at 1900x magnification. C) Image collected at 220x magnification. D) Image collected at 650x magnification.

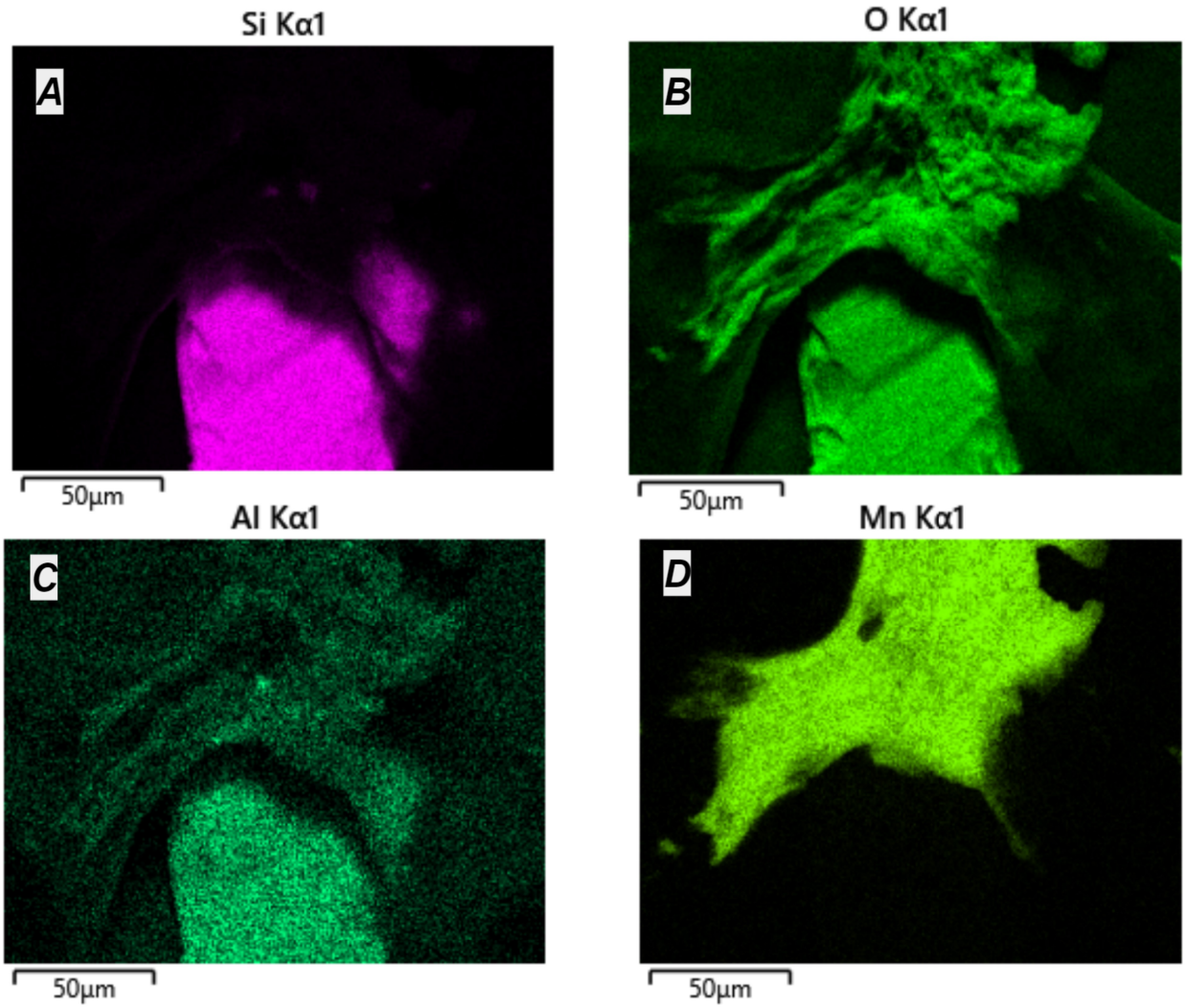

Figure S19. EDS element maps of the region shown in Figure S18D.

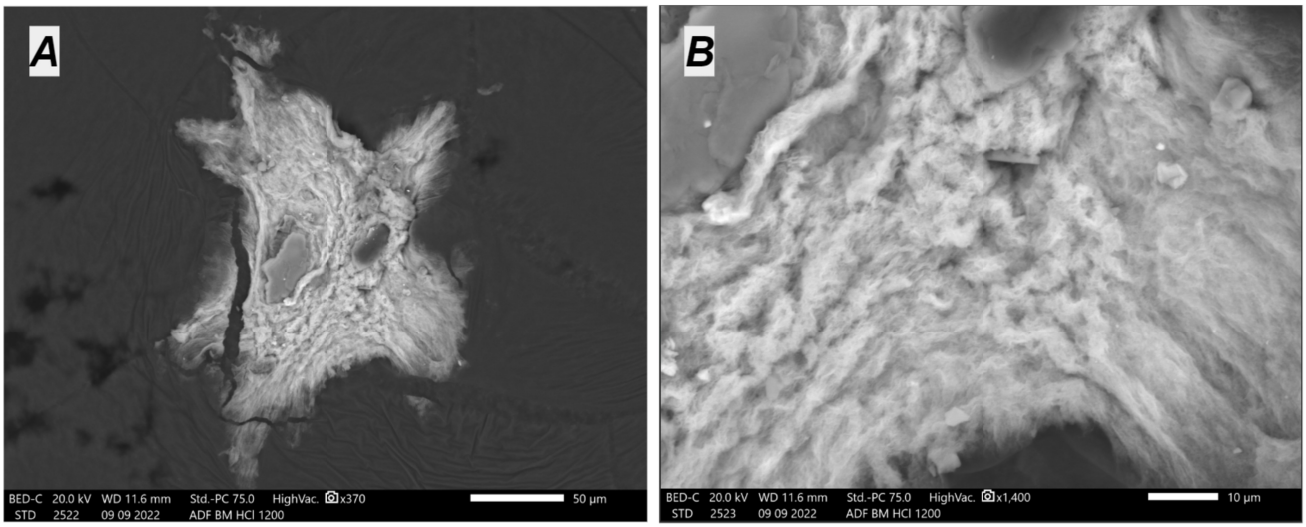

Figure S20. Scanning electron microscope images of a particle collected in pH 10 and 80 mg/L $CaCO_3$ solution at 30 days.

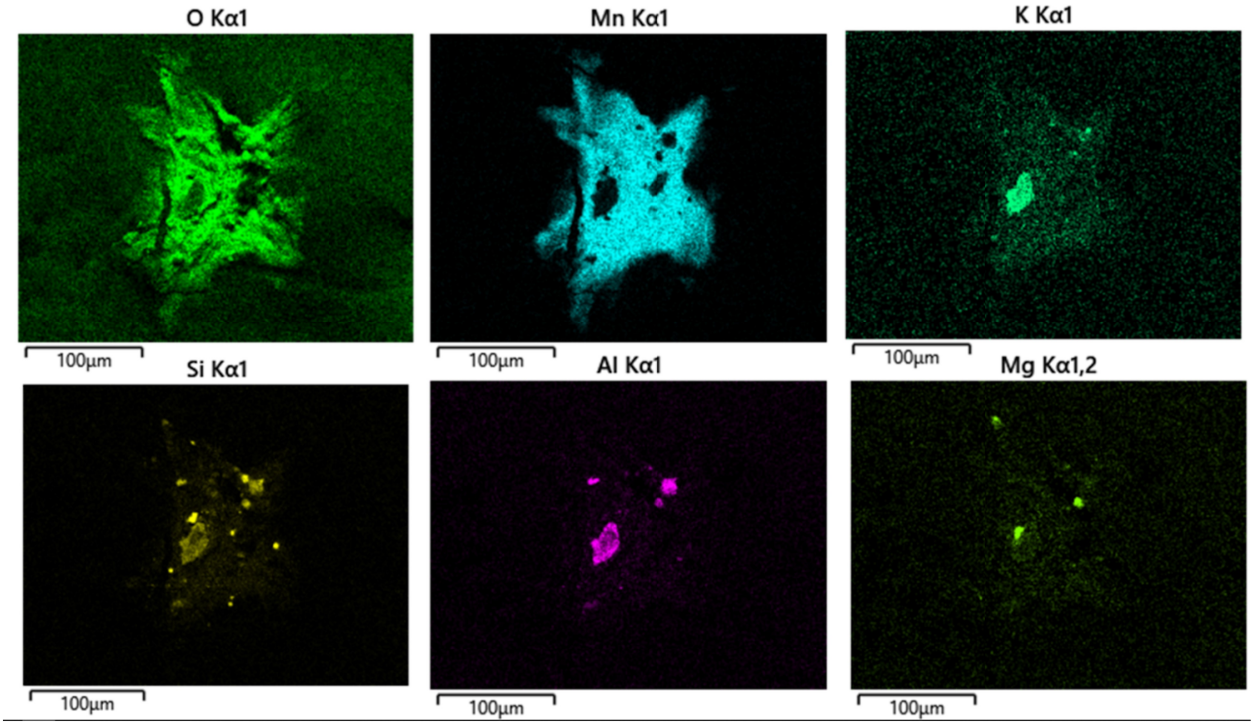

Figure S21. Energy dispersive spectroscopy element maps of the view shown in Figure S20 A.

Appendix F. Additional pH time series for 14-day pH-alkalinity experiments

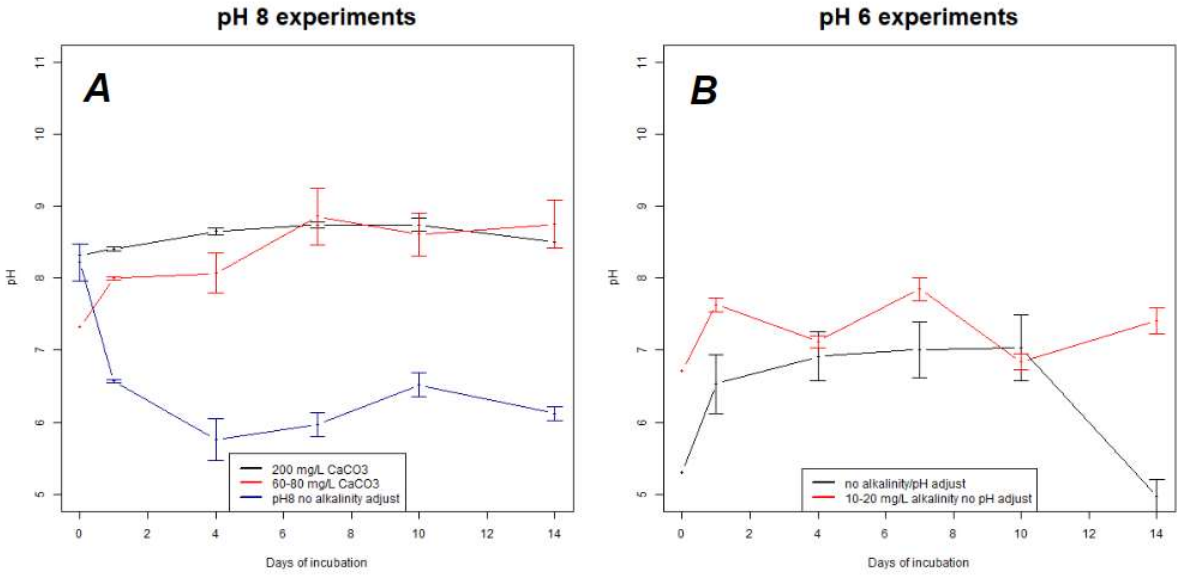

Figure S22. A) Averaged pH time series for pH 8 experiments. B) Averaged pH time series for control and low pH/low alkalinity experiments.

Appendix G. Additional scanning electron microscopy (SEM) images and electron probe microanalyzer (EPMA) elemental maps from reservoir water laboratory experiments

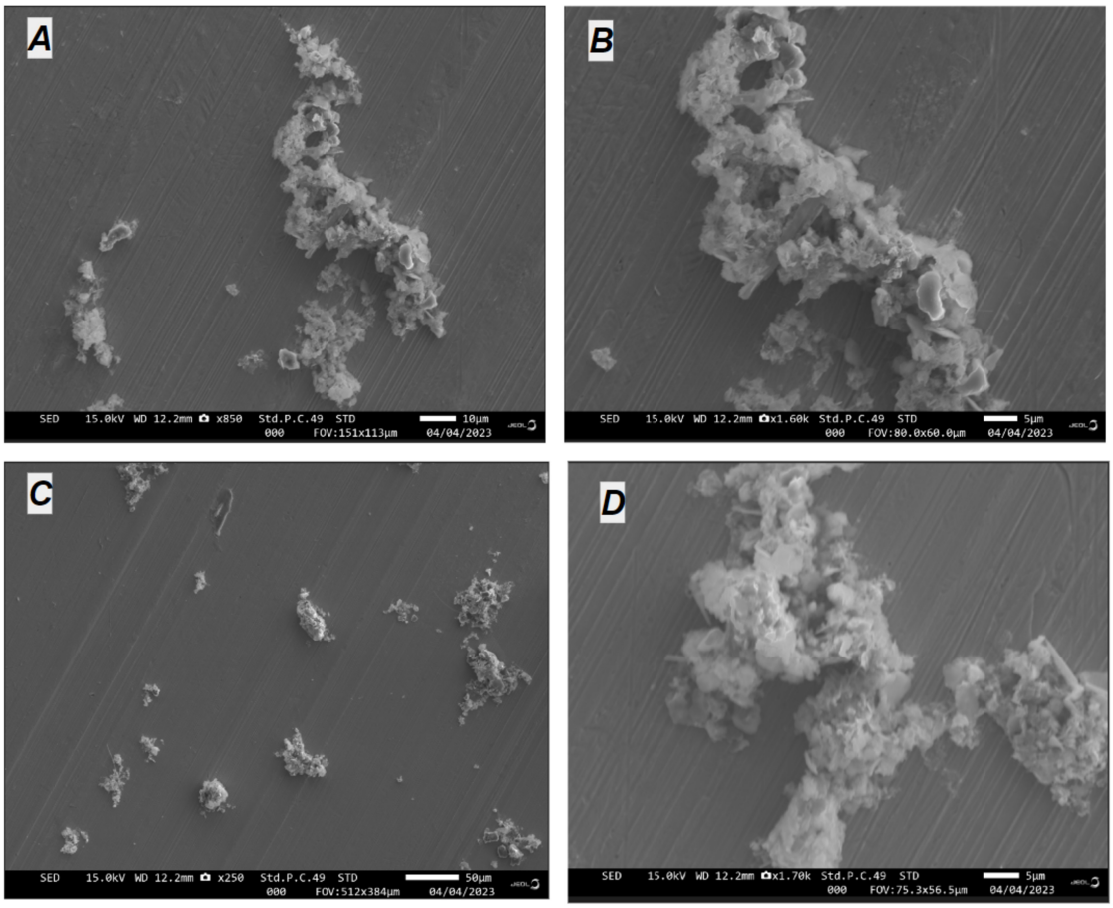

Figure S23. Scanning electron microscopy images of particles collected from CCR unfiltered reservoir water experiments at 10 days.

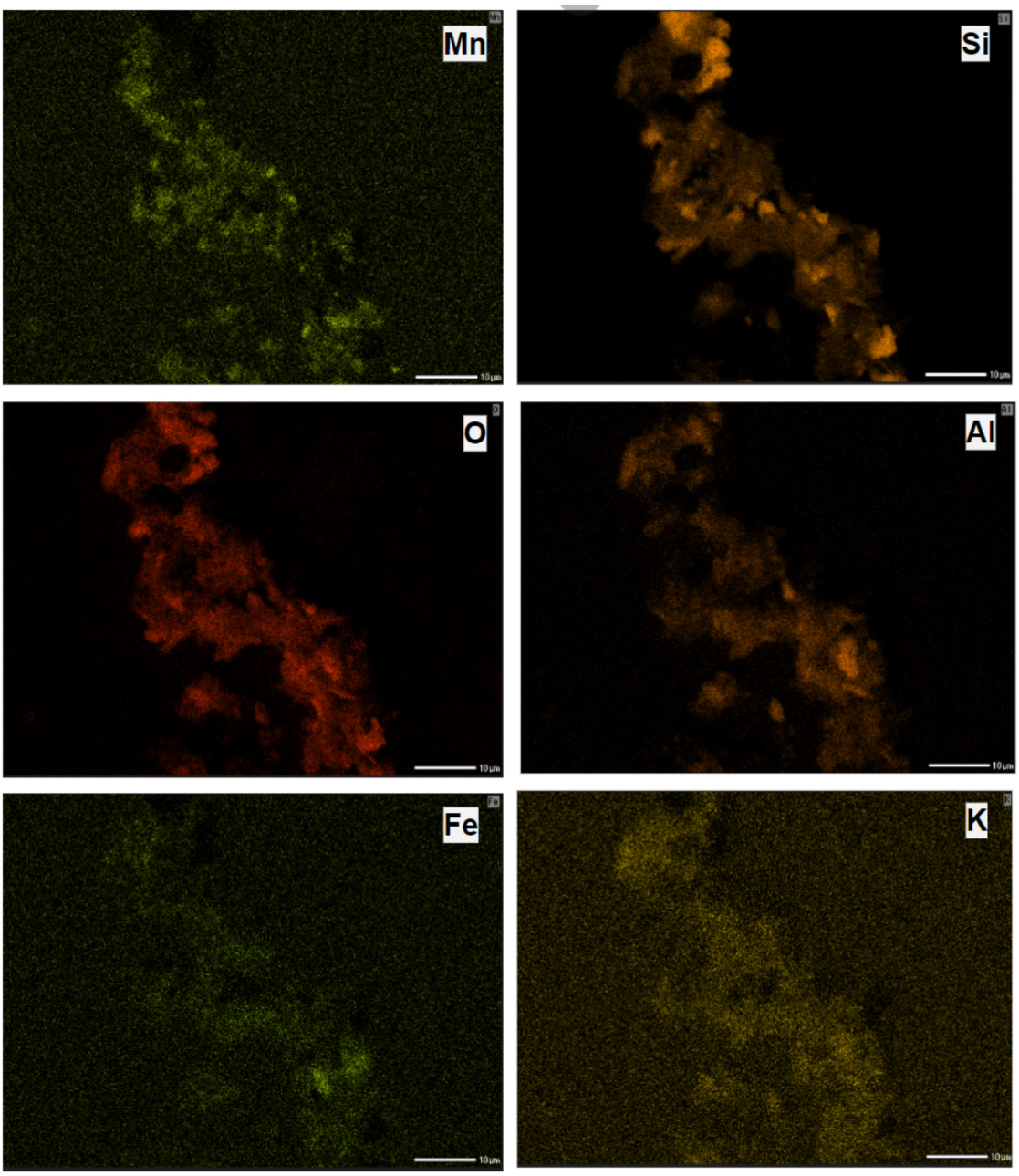

Figure S24. Electron probe microanalyzer element maps of the particle view shown in Figure S23B.

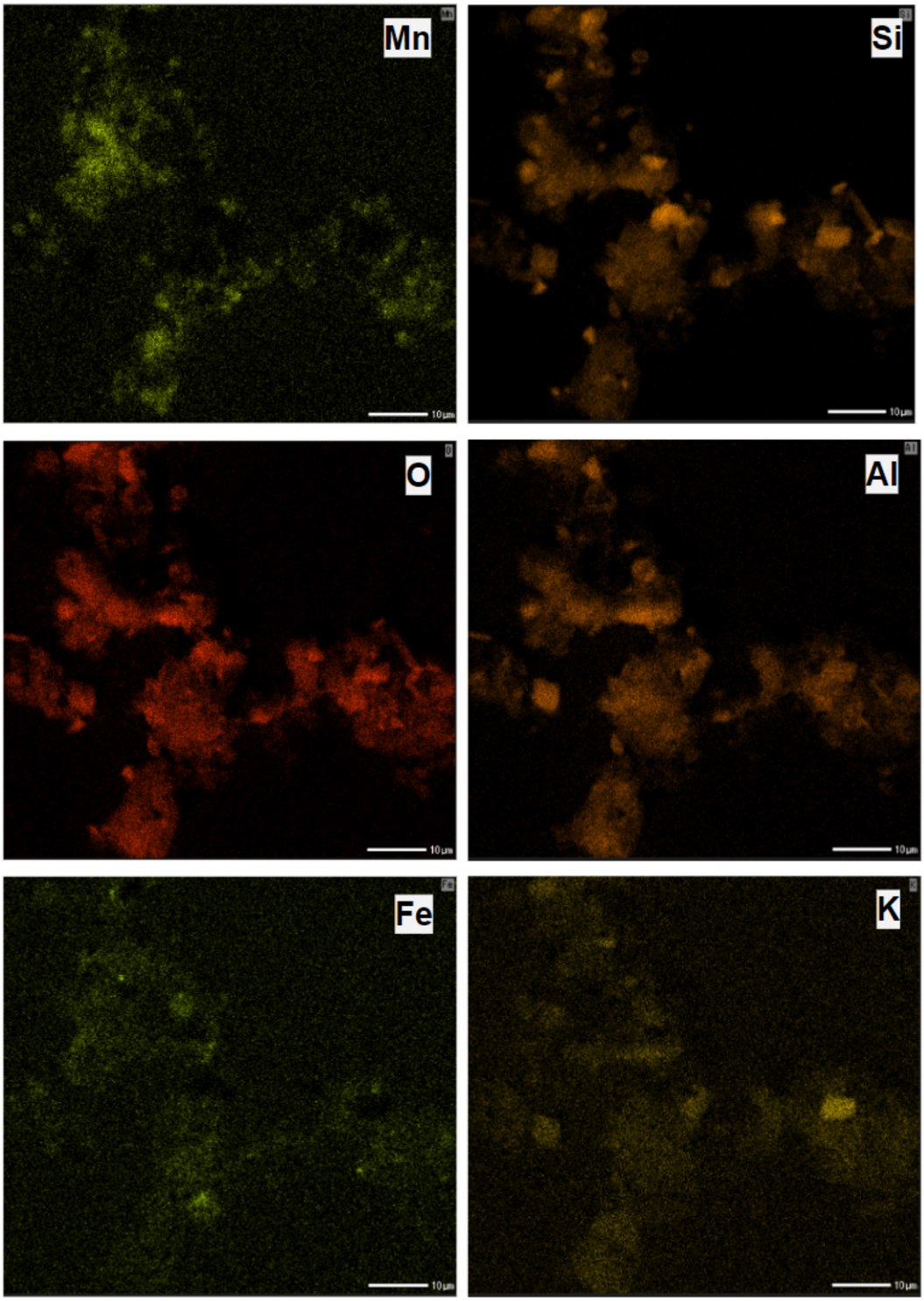

Figure S25. Electron probe microanalyzer element maps of the particle view shown in Figure S23D.

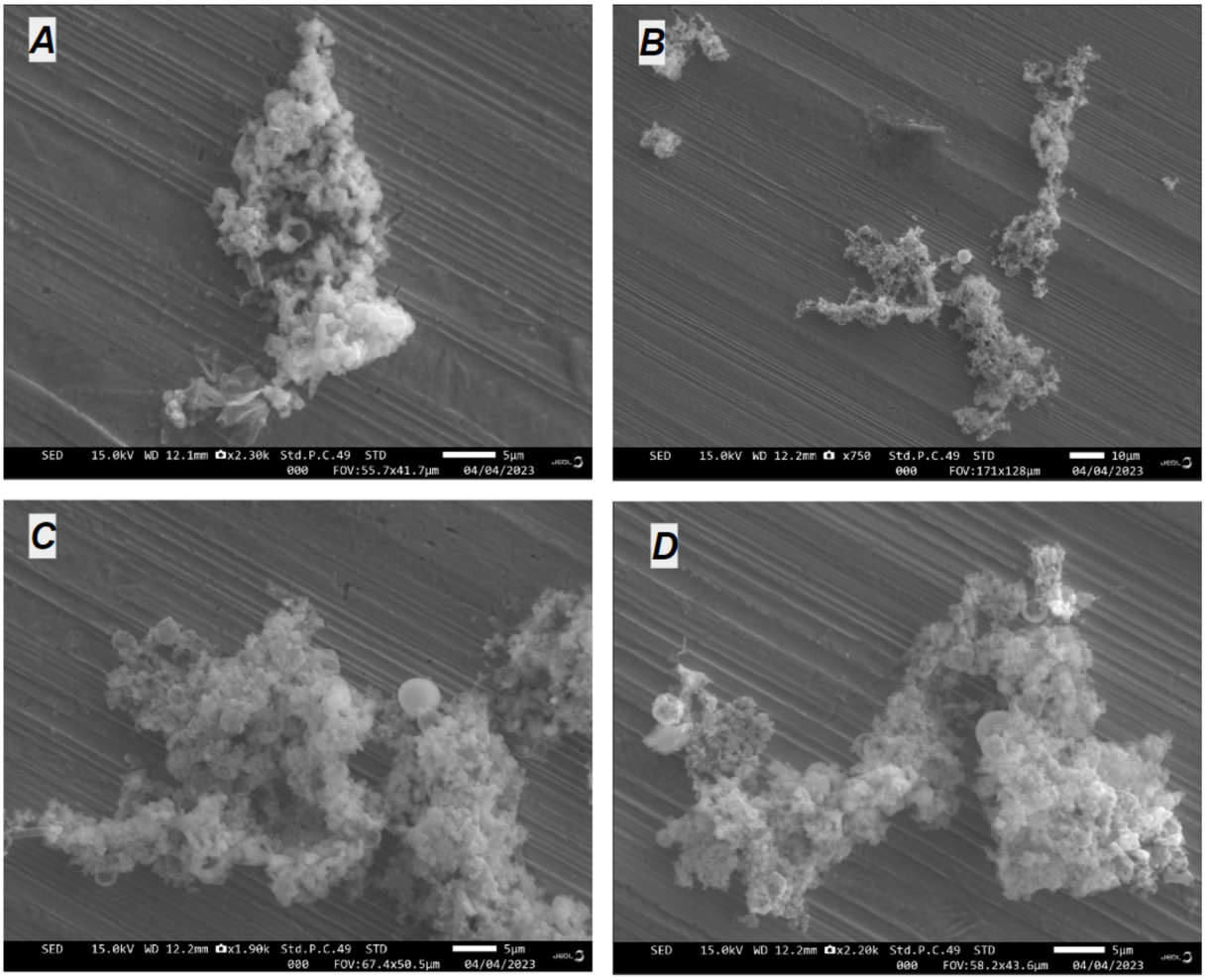

Figure S26. Scanning electron microscopy images of particles collected from the Falling Creek Reservoir filtered water experiment at 10 days.

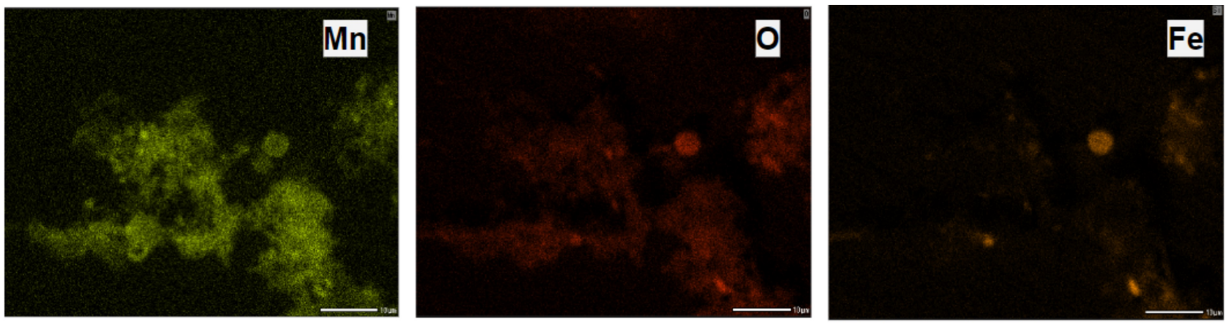

Figure S27. Manganese, oxygen and iron element maps of the particle shown in Figure S26C. Maps collected by electron probe microanalyzer.

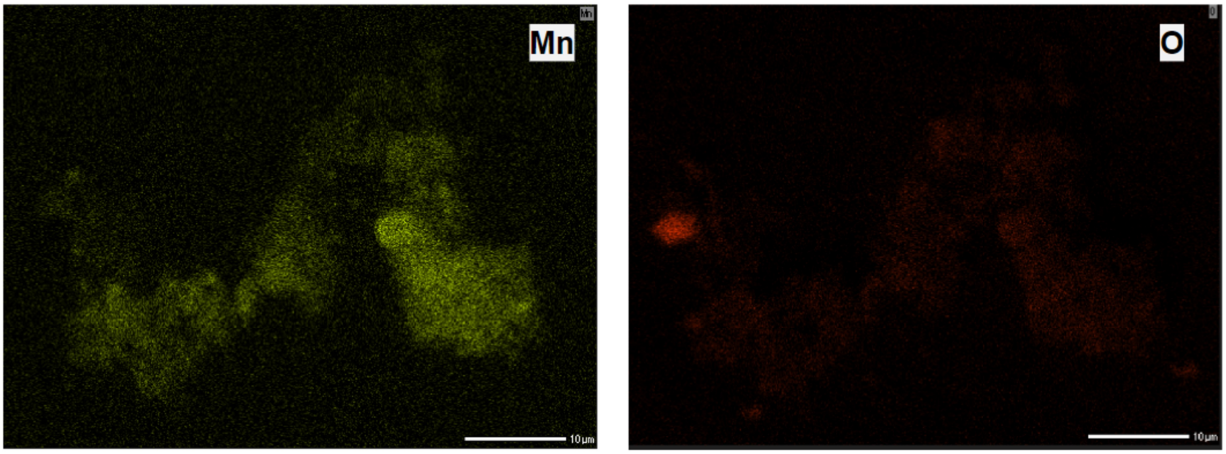

Figure S28. Manganese and oxygen element maps of the particle shown in Figure S26D. Maps collected by electron probe microanalyzer.

Appendix H. Additional transmission electron microscopy (TEM) images, selected area electron diffraction (SAED) data and energy dispersive x-ray spectroscopy (EDS) elemental maps from reservoir water laboratory experiments

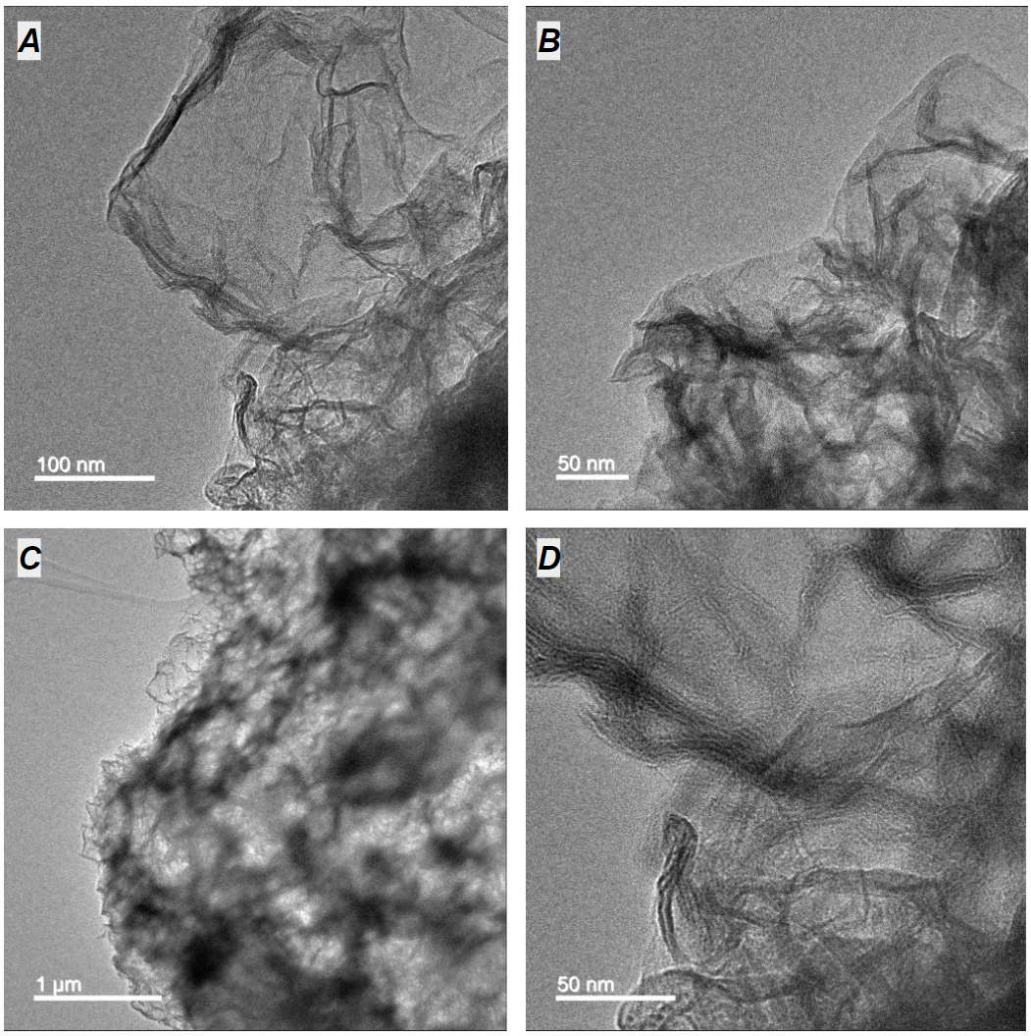

Figure S29. Brightfield transmission electron microscopy images of a particle collected from the FCR unfiltered laboratory experiment at 4 days. The particle is several um in diameter and has a crumpled sheet-like morphology. A) High-magnification image collected along the particle's periphery. B) High-magnification image of another location along the particle's periphery. C) Zoomed-out view of the particle. More stacking of sheets and greater crumpling was observed

toward the particle's interior. D) High-magnification image of a third location along the particle's periphery.

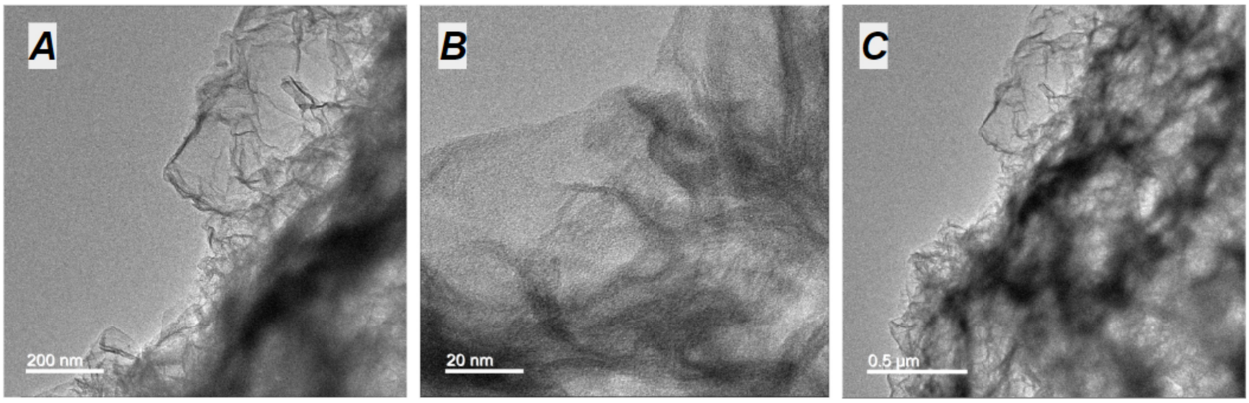

Figure S30. Additional brightfield transmission electron microscopy images of the particle shown in Figure S29. The particle is several um in diameter and has a crumpled sheet-like morphology, with more crumpling and stacking of sheets in the particle's interior. A) High-magnification image collected along the particle's periphery. B) Higher-magnification view of the particle region shown in A. C) Zoomed-out view of the particle including part of the particle interior.

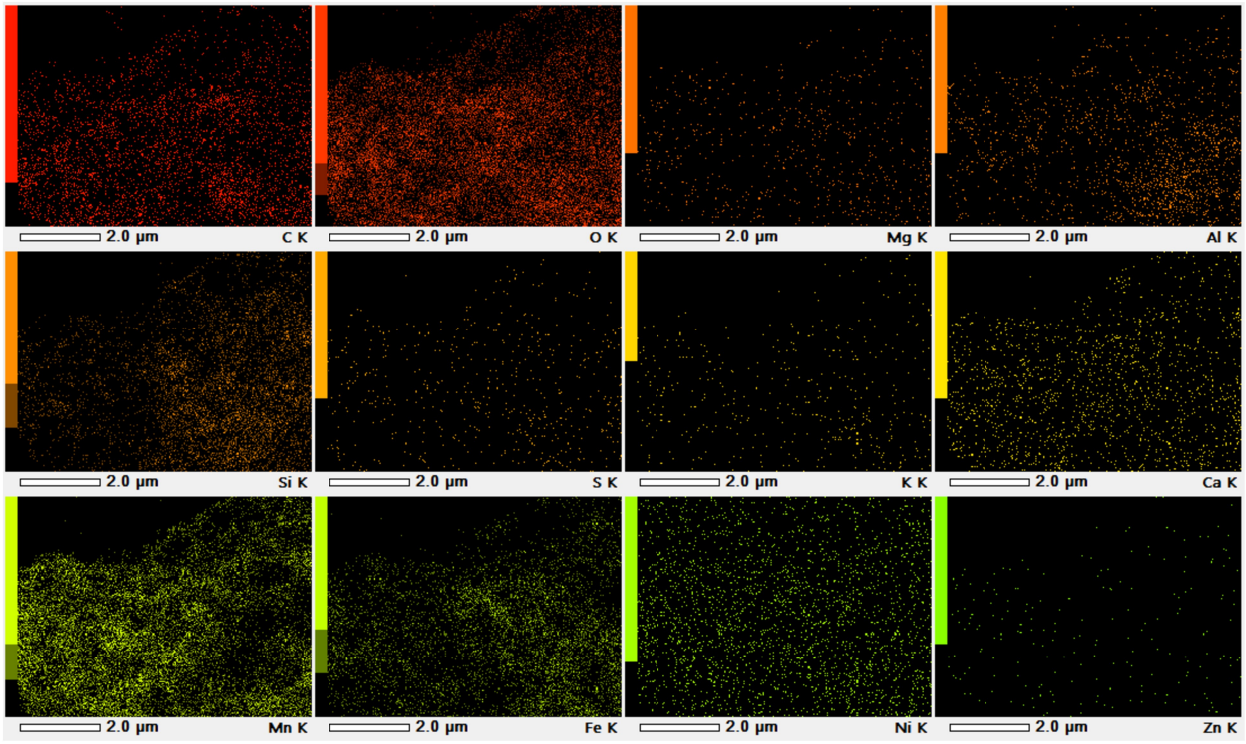

Figure S31. Energy diffraction spectroscopy element maps of a microscopic particle collected from the Falling Creek Reservoir unfiltered reservoir water experiment at day 10. The high amounts of carbon shown on the map is likely caused by the lacy carbon grid beneath the particle.

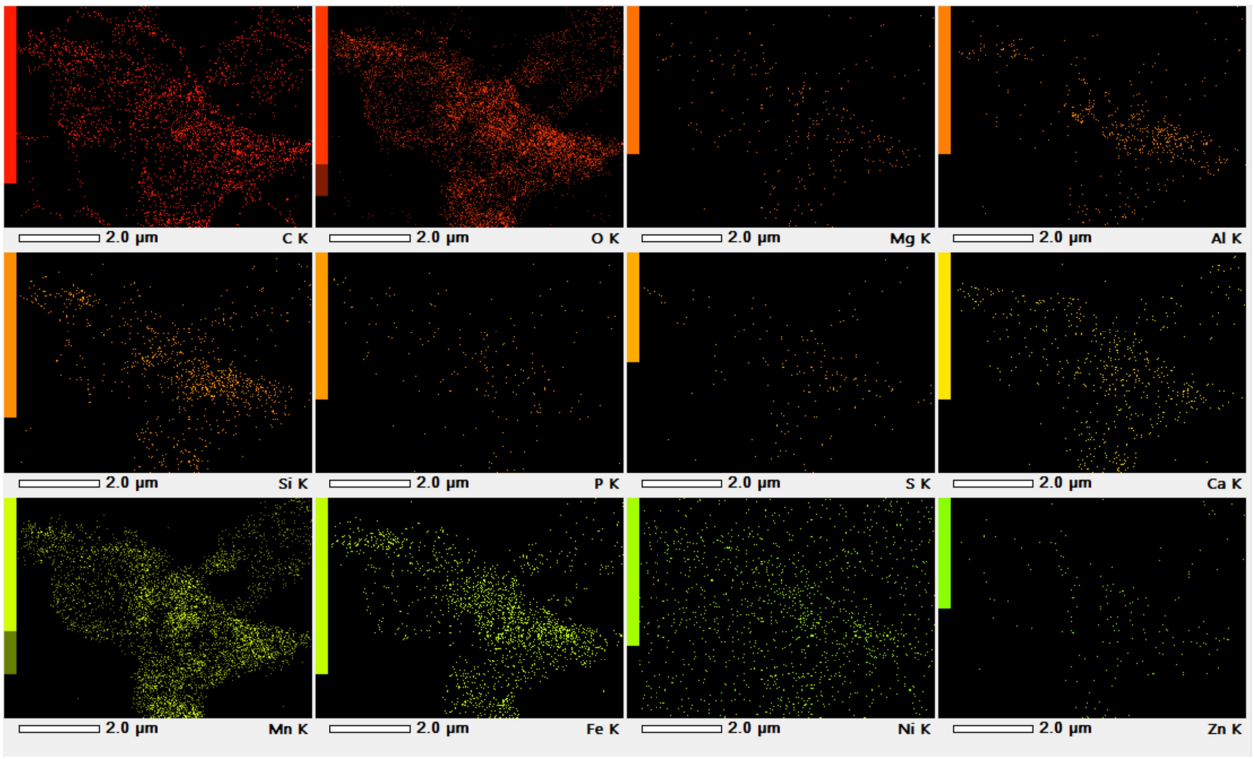

Figure S32. Energy diffraction spectroscopy element maps of a microscopic particle collected from the Falling Creek Reservoir unfiltered reservoir water experiment at day 10. The high amounts of carbon shown on the map is likely caused by the lacy carbon grid beneath the particle.

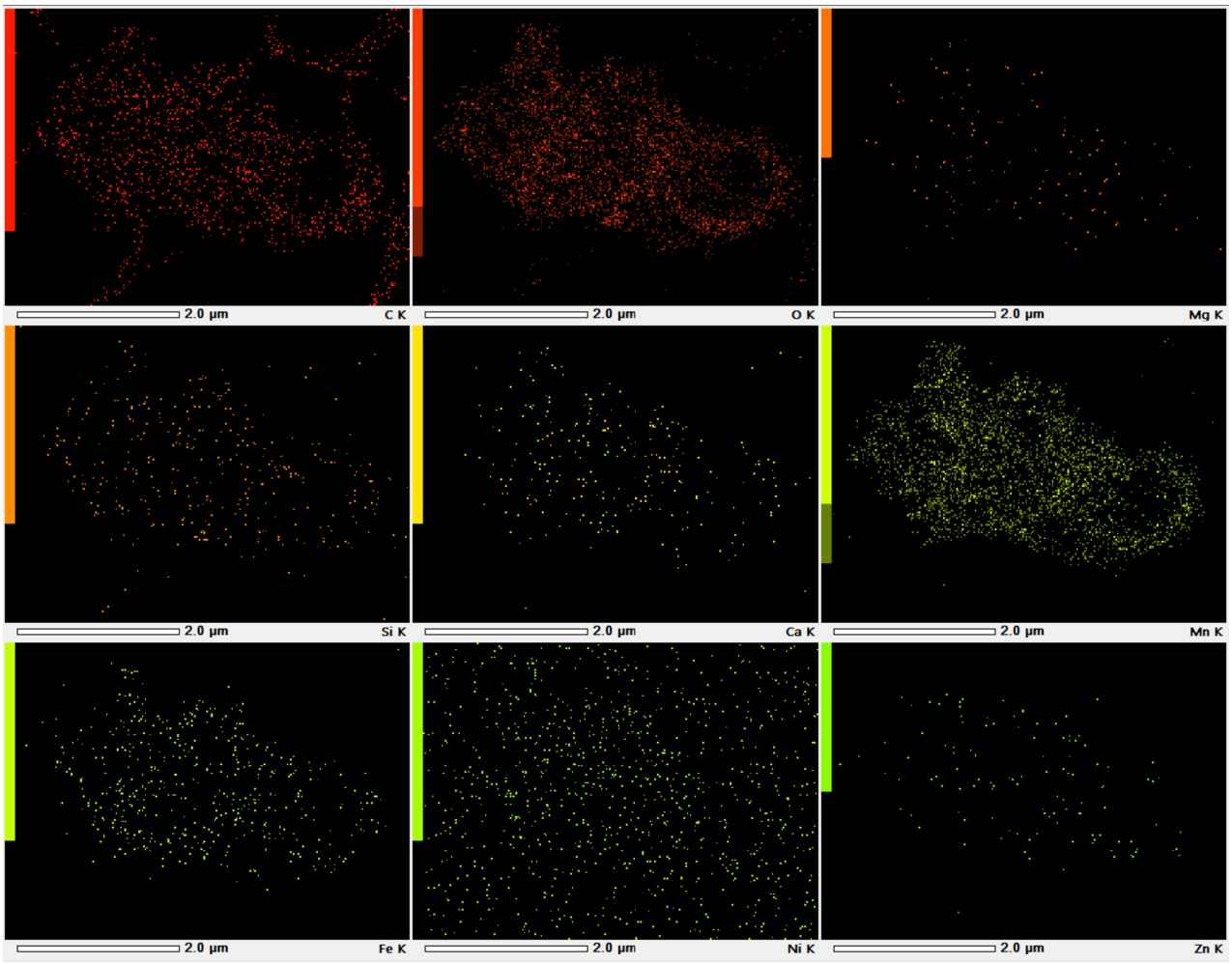

Figure S33. All energy diffraction spectroscopy element maps of the particle shown in Figure 14, collected from the Falling Creek Reservoir unfiltered water experiment. The high amounts of carbon shown on the map is likely caused by the lacy carbon grid beneath the particle.

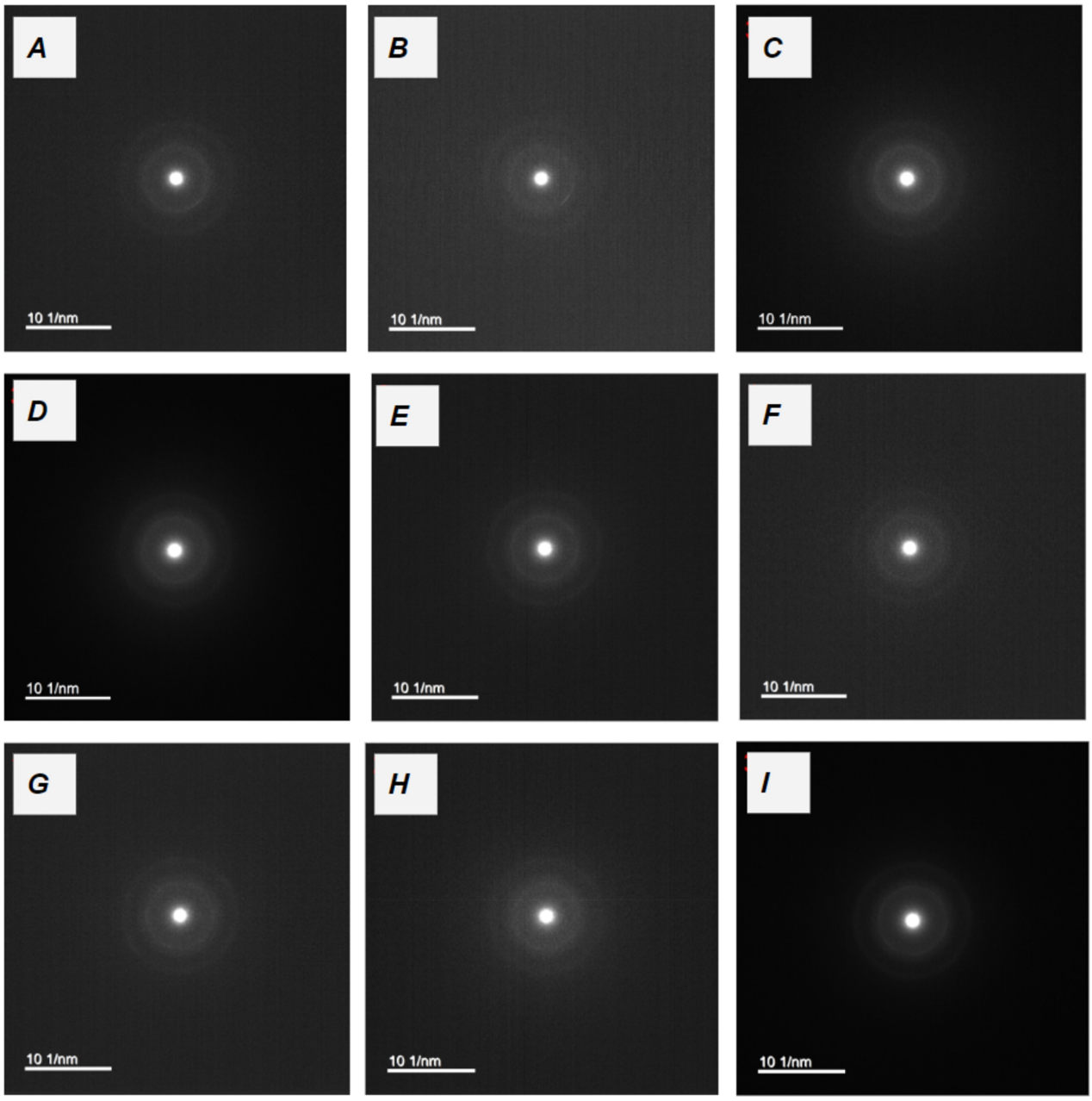

Figure S34. Selected area electron diffraction patterns from microscopic particles collected in Falling Creek Reservoir unfiltered water experiments. A, B and C are from one particle. D, E and F are from another particle. G, H and I are from a third particle.

Table S9: d-spacings obtained from diffraction patterns shown in Figure S36

	Pattern								
Ring d-spacing (Å)	**A**	**B**	**C**	**D**	**E**	**F**	**G**	**H**	**I**
1	2.55	2.54	2.49	2.52	2.56	2.48	2.52	2.54	2.49
2	1.40	1.52	1.52	1.48	1.54	1.44	1.49	1.58	1.51

Appendix I. Geochemist's Workbench inputs and results

Table S10: Reservoir pH, dissolved oxygen concentration and dissolved species concentrations entered into Geochemist's Workbench software to calculate mineral solubilities. Calculated mineral solubilities listed below inputs.

Date (2022)	6/7	6/7	6/7	6/7	6/7	6/7	6/7	7/11	7/11	7/11	7/11	7/11	7/11	7/11	7/14	7/14	7/14	7/14	7/14	7/14
Reservoir	FCR	FCR	FCR	FCR	FCR	FCR	FCR	FCR	FCR	FCR	FCR	FCR	FCR	FCR	CCR	CCR	CCR	CCR	CCR	CCR
Depth (m)	0.1	1.6	3.8	5	6.2	8	9	0.1	1.6	3.8	5	6.2	8	9	0.1	1.5	6	9	15	20
Site	50	50	50	50	50	50	50	50	50	50	50	50	50	50	50	50	50	50	50	50
Inputs																				
Cl (mg/L)	0.85	0.89	0.86	0.92	0.96	1.1	0.96	1.19	1	1.18	1.21	1.15	1.01	1.23	1.71	1.73	1.79	1.9	1.98	2.02
NO3-N (mg/L N)	0.1	0.1	0.1	0.1	0.1	0.1	0.1	0.1	0.1	0.1	0.1	0.1	0.1	0.1	0.1	0.1	0.1	0.1	0.1	0.1
SO4 (mg/L)	0.77	0.83	0.93	0.94	0.91	0.89	0.89	0.39	0.4	0.53	0.42	0.63	0.64	0.65	5.52	5.49	5.54	5.65	5.65	5.49
Na (ppb)	2460.9	2535.2	2802.2	2958	2916.1	2963	2925.7	2603	2461.1	2797.3	2994.8	2939.7	2934.8	3038.2	1375.9	1396.1	1418.2	1459.6	1470.6	1476.5
Mg (ppb)	859.8	893.5	1036.1	1129.5	1117.6	1153.7	1127.6	864.4	867.5	1050.7	1166.2	1159.8	1186.3	1184.4	2461.4	2505.2	2623.8	2808	2937.5	3011.9
Al (ppb)	19.7	27.8	15.9	10	11.2	9.5	9.8	14.6	12.7	7	3.9	2.1	2.2	2.2	7.1	6.5	3.1	2.4	2.5	2.9
K (ppb)	1041.6	1023	956.4	1000.1	1068.4	1085.8	1072.1	1279.2	1218.7	1243.2	1194.3	1224.1	1147.8	1312.1	909.9	921	926.9	939	946.6	979.1
Ca (ppb)	1871	1909.1	2347.2	2674.9	2697.6	2773.4	2734	1893.5	1925.3	2588.1	2936.4	2918.4	2976.9	2990.6	9345.2	9449.1	9872.4	10636.6	11318.6	11592.7
Fe (ppb)	248	266.9	137.8	51.3	56	41.8	42.8	616.9	576.1	1499.7	3495.7	352.2	39.1	69.2	6.1	0	0	0	0	13
Mn (ppb)	3	2.6	2.7	416.1	580.8	679.8	634.1	23.9	32	357.7	764.5	859.7	959.4	941.9	0.4	5.9	1.4	60.8	221.5	1681.1
pH	9.67	9.65	8.26	7.83	7.42	7.12	6.99	9.23	8.26	7.18	7	6.82	6.64	6.6	8.26	8.33	8.22	7.69	7.23	7.11
DO (mg/L)	11.6	13.9	2.63	1.92	1.94	1.89	1.84	6.44	0.14	0.079	0.531	0.637	0.645	0.643	6.93	6.92	9.23	5.5	5.18	2.43
Alkalinity (mg/L $CaCO_3$)	15.5	15.5	15.5	15.5	15.5	15.5	15.5	16.1	16.1	16.1	21.55	21.55	21.55	21.55	35.63	35.63	45.5	45.5	45.5	45.5
Results																				
Birnessite (log Q/K)	39.1	38.2	48.7	59.6	54.2	50.0	47.6	51.7	53.01	-65.0	43.0	44.4	42.0	41.3	41.9	51.6	45.9	51.8	48.9	53
Hausmannite (log Q/K)	2.9	2.5	6.9	11.0	9.0	7.4	6.6	7.8	9.5	-12	6.0	5.7	4.8	4.5	4.1	7.7	5.5	7.8	6.8	8.1
Rhodochrosite (log Q/K)	-5.5	-5.6	-2.5	-0.71	-1.0	-1.2	-1.4	-3.3	-1.4	-1.5	-1.2	-1.4	-1.6	-1.6	-3.2	-2.1	-2.6	-1.3	-1.2	-0.4

Table S11: Experimental solution pH, dissolved oxygen concentration and dissolved species concentrations entered into Geochemist's Workbench software to calculate mineral solubilities. Calculated mineral solubilities listed below inputs.

Treatment	high pH/moderate alkalinity	high pH/high alkalinity	high pH	moderate pH/moderate alkalinity	moderate pH/high alkalinity	moderate pH
Inputs						
Mn (ppb)	1000	1000	1000	1000	1000	1000
pH	10	10	10	8.5	8.5	8.5
Alkalinity (mg/L $CaCO_3$)	80	200	30	80	200	10
DO (mg/L)	2	2	2	2	2	2
Results						
Birnessite (log Q/K)	62.1	62.9	62.9	71.0	70.7	71.1
Hausmannite (log Q/K)	12.3	12.4	12.4	15.2	15.2	15.4
Rhodochrosite (log Q/K)	-2.0	-1.5	-2.3	1.2	1.2	-0.05